ORNL/TM-10787

ornl

OAK RIDGE NATIONAL LABORATORY

MARTIN MARIETTA

Determination of Multiaxial Flow Surfaces at Elevated Temperatures Using the Concept of Dissipation Potential

J. A. Clinard
C. Lacombe

OPERATED BY
MARTIN MARIETTA ENERGY SYSTEMS, INC.
FOR THE UNITED STATES
DEPARTMENT OF ENERGY

Printed in the United States of America. Available from
National Technical Information Service
U.S. Department of Commerce
5285 Port Royal Road, Springfield, Virginia 22161
NTIS price codes—Printed Copy: A05 Microfiche A01

ORNL/TM-10787

Interagency Agreement DOE No. 1819-1447-A2

Engineering Technology Division

DETERMINATION OF MULTIAXIAL FLOW SURFACES AT ELEVATED TEMPERATURES USING THE CONCEPT OF DISSIPATION POTENTIAL

J. A. Clinard
Oak Ridge National Laboratory
Engineering Technology Division

C. Lacombe
University of Tennessee

April 1988

Note: This document contains information of a preliminary nature. It is subject to revision or correction and therefore does not represent a final report.

Prepared by the
OAK RIDGE NATIONAL LABORATORY
Oak Ridge, Tennessee 37831
operated by
MARTIN MARIETTA ENERGY SYSTEMS, INC.
for the
U.S. DEPARTMENT OF ENERGY
under Contract No. DE-AC05-84OR21400

CONTENTS

DETERMINATION OF MULTIAXIAL FLOW SURFACES AT ELEVATED TEMPERATURES USING THE CONCEPT OF DISSIPATION POTENTIAL

J. A. Clinard
C. Lacombe

ABSTRACT

This analytical activity builds on previous experimental efforts at Oak Ridge National Laboratory to measure multiaxial flow surfaces using tubular specimens of type 316 stainless steel. Tests were isothermal at 650°C (1200°F). Flow surface determination was conducted after certain torsional preloadings and was composed of a series of 16 probes at 16 distinct axial/torsional stress-rate ratios. These probes sufficiently characterized the flow surfaces in the stress subspace. Previous analytical efforts reduced the experimental data for determination of surfaces of constant inelastic strain rate (SCISR). Current efforts remove assumptions concerning the inelastic strain state (for the multiaxial response) and reuse the experimental data to cast flow surfaces in the form of surfaces of constant dissipation potential (SCDP). Some 43 SCDP flow surface families are determined from the high-temperature experimental database. Details of the analytical techniques are provided. Resulting preliminary assessments are presented and discussed concerning various theoretical subjects such as normality of strain rate vectors and goodness-of-fit of candidate stress functions composed of second and third stress invariants.

1. INTRODUCTION AND BACKGROUND

This report documents recent data reduction efforts that are a follow-on to an experimental effort performed in 1984 for NASA-Lewis Research Center (under Interagency Agreement). The purpose of the effort documented herein is to carry out a detailed computerized assessment and presentation of the previously gathered data and to use the information to develop a series of multiaxial flow surfaces representing constant dissipation potential or rate of inelastic work.

The report is based on efforts funded by NASA under the agreement DOE No. 1819-1447-A2.

Special exploratory multiaxial tests on type 316 stainless steel at 650°C (1200°F) resulted from previous cooperative efforts among the staffs of the Oak Ridge National Laboratory and NASA-Lewis Research Center. Flow

surfaces in the form of constant inelastic strain rate were experimentally determined using ORNL facilities. This previous experimental effort produced data that continue to feed ORNL's and NASA's efforts to formulate constitutive theories for high-temperature structural alloys. Because the original study was carefully planned and the database was carefully collected and preserved, the data remain prominent for investigation of emerging theories of multiaxial material behavior. Indeed, the current effort reinvestigates the data originally collected to conditions of constant inelastic strain rate (SCISR) to produce new representations in the form of surfaces of constant dissipation potential (SCDP). The SCDP flow surfaces form the bases of a viscoplastic constitutive theory that reduces assumptions concerning the multiaxial stress dependence.

In the remainder of this chapter brief background information is given concerning theoretical considerations forming the basis of the analytical study. The experimental considerations are revisited briefly. The following two chapters discuss the data analysis methodology in some depth and summarize results and findings. Then a closure is provided which discusses possibilities for additional studies. In the appendix many example plots are given of SCISR and SCDP flow surfaces.

1.1 Theoretical Consideration

The theory behind the experimental and analytical efforts discussed in this document was first presented in Ref. 1 where a unified (viscoplastic) constitutive theory for high-temperature structural alloys, such as stainless steels and high-alloy steels, was developed. The multiaxial aspects of the viscoplastic theory were further developed along the lines of Drucker (Ref. 2) and presented in Ref. 3. Much of this discussion repeats the descriptions of Ref. 3.

The present work builds upon a multiaxial database to support premises of the Ref. 3 theory for fully isotropic materials where inelastic deformation behavior is relatively independent of hydrostatic stress. The Ref. 3 approach begins with the assumption of the existence of a dissipation

potential function

$$\Omega(\sigma_{ij}, \alpha_{ij}) = \emptyset(J_2, J_3) + \hat{D}(\hat{J}_2, \hat{J}_3) \tag{1}$$

with the generalized normality structure

$$\dot{\epsilon}^p_{ij} = \frac{\partial \Omega}{\partial \sigma_{ij}} \tag{2}$$

$$-\dot{\alpha}_{ij}/h = \frac{\partial \Omega}{\partial \alpha_{ij}} \ , \tag{3}$$

where σ_{ij} and α_{ij} denote the applied and internal stress, and $\dot{\epsilon}^p_{ij}$ denotes the inelastic strain rate. h is a scalar function of the internal stress. With the further assumption concerning independence from hydrostatic stress (J_1), a specific theory results that employs the second (J_2) and third (J_3) principal invariants of σ_{ij} and α_{ij} to produce the complete multiaxial theory as below:

Flow Law

$$\dot{\epsilon}^p_{ij} = f(F)\Gamma_{ij} \tag{4}$$

in which

$$\Gamma_{ij} = J_2^2 \sum_{ij} - \frac{2C}{3} J_3 \ t_{ij} \tag{5}$$

and

$$t_{ij} = \sum_{ik}\sum_{kj} - \frac{2}{3} J_2 \ \delta_{ij} \ . \tag{6}$$

Growth Law

$$\dot{a}_{ij} = h(G)\dot{\epsilon}^p_{ij} - r(G)\pi_{ij} \tag{7}$$

in which

$$\pi_{ij} = \hat{J}_2^2 \ a_{ij} - \frac{2C}{3} \hat{J}_3 \ g_{ij} \tag{8}$$

and

$$g_{ij} = a_{ik}a_{kj} - \frac{2}{3} \hat{J}_2 \ \delta_{ij} \ . \tag{9}$$

In the flow law the following terms are involved:

S_{ij} and a_{ij} are the deviators of applied and internal stress respectively.

$$\sum_{ij} = S_{ij} - a_{ij} \tag{10}$$

is called the stress difference.

The second and third scalar invariants of $\sum_{ij}$ are

$$J_2 = \frac{1}{2} \sum_{ij} \sum_{ij} \tag{11}$$

and

$$J_3 = \frac{1}{3} \sum_{ij} \sum_{jk} \sum_{ki} \ . \tag{12}$$

Lastly,

$$F = \frac{(J_2^3 - CJ_3^2)^{1/3}}{\kappa^2} - 1 \ . \tag{13}$$

In the growth law for a_{ij}, the following terms are involved:

The second and third scalar invariants of a_{ij} are

$$\hat{J}_2 = \frac{1}{2} a_{ij} a_{ji} \tag{14}$$

and

$$\hat{J}_3 = \frac{1}{3} a_{ij} a_{jk} a_{ki} \ . \tag{15}$$

Lastly,

$$G = \frac{(\hat{J}_2^3 - C\hat{J}_3^2)^{1/3}}{\kappa^2} \ . \tag{16}$$

In the flow and growth laws the functions f(F), h(G), and r(G) can be determined from uniaxial testing as described in Refs. 4–6. The values of C and κ must be determined from multiaxial tests.

Returning to Eq. (1) since we have not yet defined Ø and Đ, Robinson suggests in Ref. 1 that

$$\text{Ø} = \frac{\kappa^2}{\mu(n+1)} F^{\frac{n+1}{2}} \quad \text{and} \tag{17}$$

$$\text{Đ} = \frac{r(G)}{h(G)} \frac{\kappa^2}{\mu(n+1)} G^{\frac{n+1}{2}} , \tag{18}$$

where μ and n are other material parameters. The author also suggests specific forms for r and h for J_2-materials. Since we do not use or attempt to quantify r, h, μ, or n in the current study we drop the discussion here.

The present study provides information regarding the form of the stress functions F and G. In the tension-torsion subspace F and G are ellipse-like. In the data "fitting" process, F is approximated by an ellipse in order to simplify the computational task. The values of C and κ for a 16-probe dataset [$(\sigma_{11},\sigma_{12})$ pairs representing the loci of stress states producing constant dissipation potential] result approximately form the ellipse fit as will be discussed later in greater detail. It should be clearly understood that the testing and data reduction philosophy are based on the assumption of "nearly" constant values of C, κ, and a_{ij} in F during flow surface probing. However, changes of C, κ, and a_{ij} as functions of the preloading are expected as illustrated.

With a_{ij} constant (as in mild probing of a "nearly" constant inelastic state), the dissipation potential may be expressed in general form as

$$\Omega = \int_o^{\sigma_{ij}} \dot{\epsilon}_{ij} \, d\sigma_{ij} , \tag{19}$$

or, alternately and more specifically for the tension-torsion subspace as

$$\Omega = \int_o^t \dot{\epsilon}^p_{11} \, \dot{\sigma}_{11} \, dt + \int_o^t 2\dot{\epsilon}^p_{12} \, \dot{\sigma}_{12} \, dt , \tag{20}$$

where subscript 11 stands for the axial component and subscript 12 stands for the torsional component of strain and stress. During the probing

sequences $\dot{\sigma}_{11}$ and $\dot{\sigma}_{12}$ are constants in the experimental procedure. t is the time of the probe.

1.2 Experimental Considerations

Test Facility. The high-temperature multiaxial test facility employed to produce the data of this study was designed to apply axial and torsional loads simultaneously to tubular specimens as prescribed by manual or computer generated controls. The facility is made up of the following components:

- axial-torsional material testing system,
- radio frequency induction heating system,
- data acquisition and control system, and
- axial-torsional extensometer.

An extensive description of the specifications for the above devices is given in Ref. 8.

Test Specimen. The tubular test specimens (Fig. 1) were obtained from 51 mm bars of 316 stainless steel. The material is part of the ORNL reference heat No. 8092297. Specimens had a nominal 34.8 mm working section with a 26.04 mm outside diameter and a 1.91 mm wall thickness. Specimens were heated to 1065°C, held for a 30-min solution annealing, and then subjected to rapid cooling.

Tests Performed. Two 650°C high-temperature test sequences were performed as depicted in Figs. 2 and 3:

- A short-time test sequence (Fig. 2) during which 9 flow surface determinations were conducted at various points on a cyclic plastic torsional preloading loop. (The preloadings were strain-controlled at a rate of 500 $\mu\epsilon$/min.)
- A long-term creep test sequence (Fig. 3) during which 34 flow surface determinations were conducted at various times during the 14-week torsional stress-controlled creeping sequence.

Of the 9 determinations of the short-time test sequence, 4 were immediate repetitions prior to resumption of the cyclic preloading. In the long-

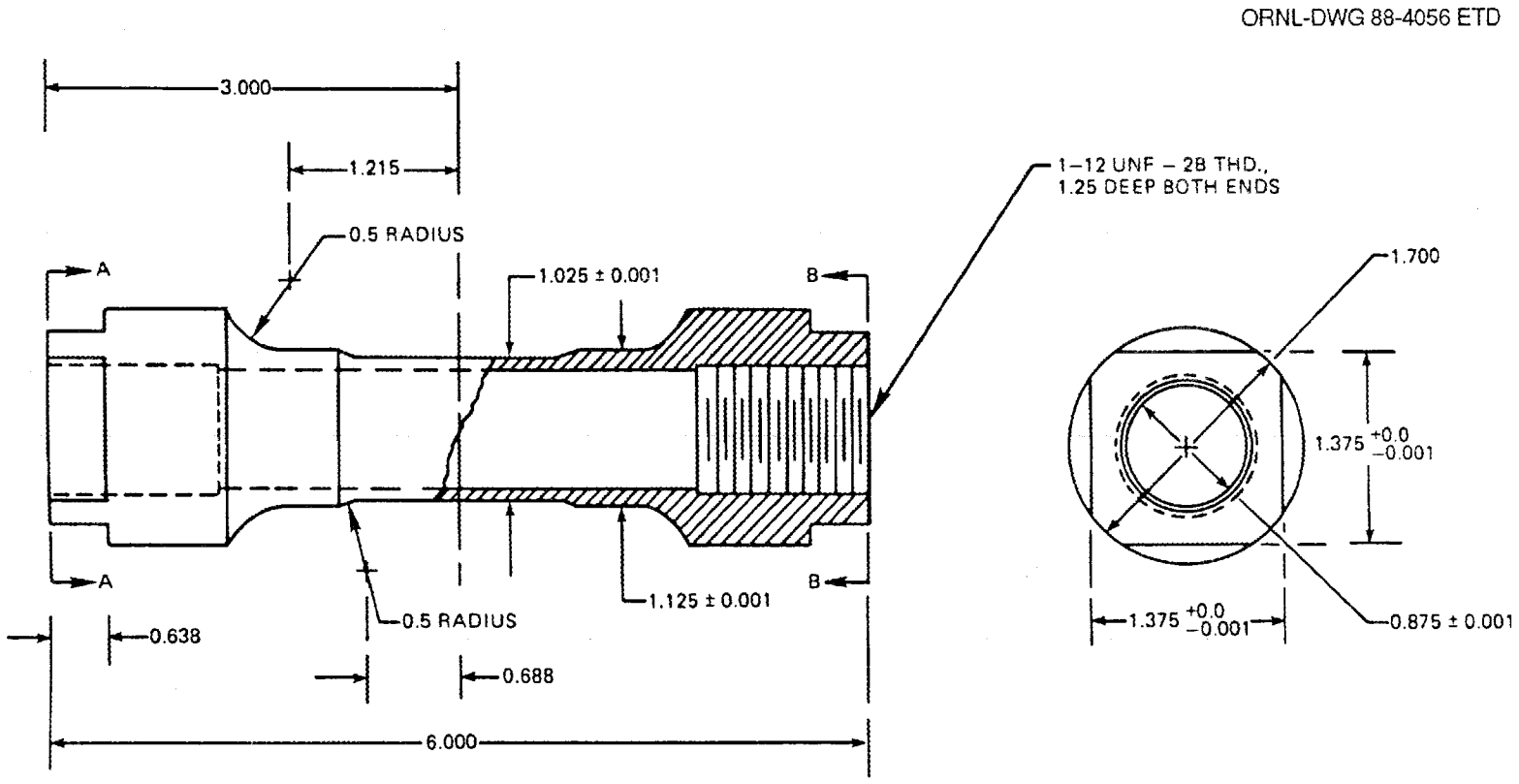

Fig. 1. Schematic of the test specimen. Dimensions in inches.

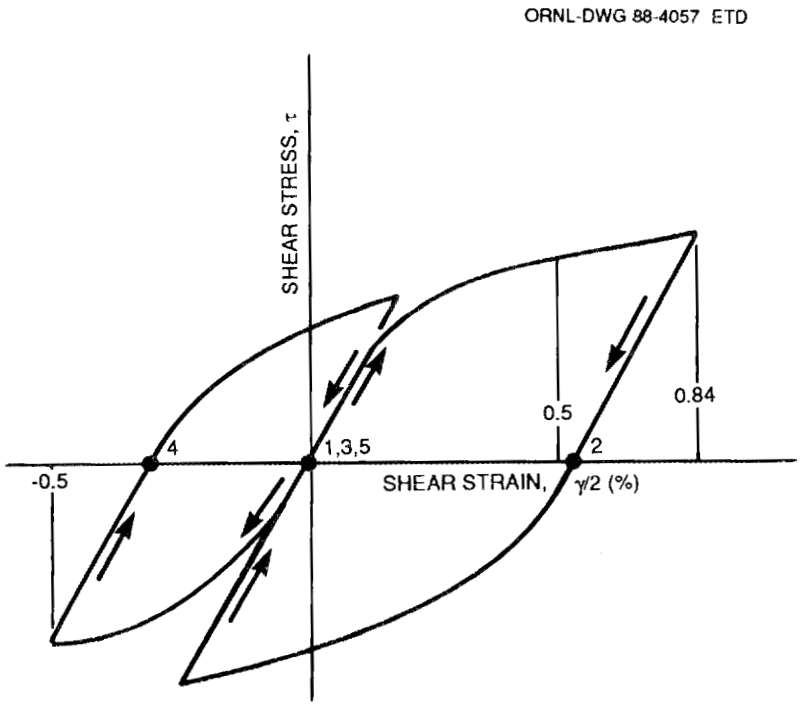

Fig. 2. Short-time test sequence. Flow surfaces were determined at points 1–5 of the preloading loop. The preloadings are strain-controlled at a rate of 500 $\mu\epsilon$/min.

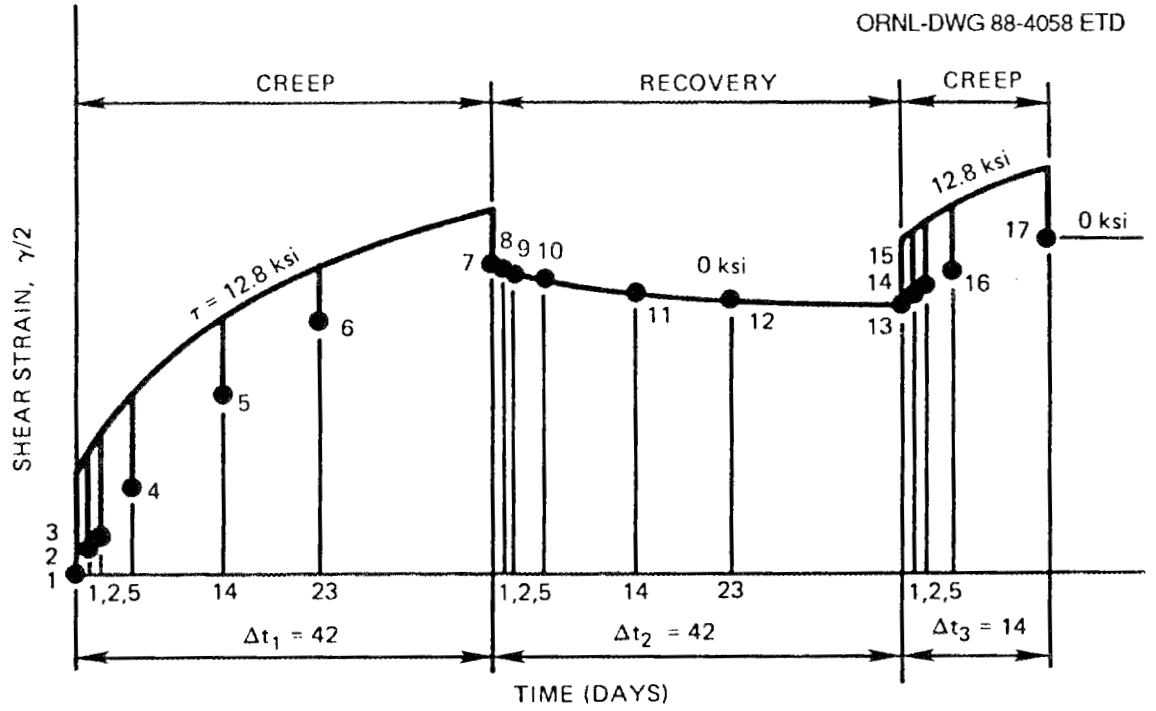

Fig. 3. Long-term creep test sequence. Flow surfaces were determined at points 1–17.

term test sequence each of 17 primary determinations was repeated to produce the 34 total flow surface determinations.

The preloadings were intended to establish inelastic states which remained "nearly" constant during flow surface determinations. The changes in the flow surfaces due to the preloadings are studied allowing experimental investigation of the growth law in Eq. (7).

All 43 determinations were conducted as SCISR-type sequences; that is, each determination consisted of 16 axial-torsional probes executed at a uniform stress rate of value 69 MPa/min (10^4 psi/min) until an inelastic strain rate (J_2-form) of 100 $\mu\epsilon$/min was measured.

Recording and Pre-Processing of Data. The test control program determined the set-point voltage inputs sent to the material testing system, thus controlling loads. For a given probe, testing was initiated near the stress origin and proceeded slowly by increasing the J_2-stress at a prescribed $\dot{\sigma}_{11}/\dot{\sigma}_{12}$ ratio until the measured inelastic strain rate exceeded 100 $\mu\epsilon$/min. Stress rates for the probes were content at $\bar{\dot{\sigma}}$ = 10 ksi/min. All probe stresses, strains, and times were recorded on the computer's hard disk during testing. Information was later compiled on a magnetic tape in raw form. After moving the raw data onto a minicomputer (VAX-type) reformatting was conducted to simplify subsequent data handling for the study.

2. DATA ANALYSIS METHODOLOGY

2.1 The Data Reduction Program, HOTLIPS

HOTLIPS (High Temperature Ellipse Flow Surface Program) is the computer program developed for reducing and studying the multiaxial data. HOTLIPS is written in FORTRAN and uses DISSPLA* to produce graphics. The program is operated by means of a command file supervisor (collection of input instructions) that directs program functions. Reduced data are delivered in two different formats – plots and tables. Most plots presented in this report were generated by HOTLIPS. The HOTLIPS tables provide detailed information about the data and data representations and serve as input to other post-processing programs such as LOTUS 1-2-3† used to explore global tendencies.

2.2 Program and Data Files

The file environment during the data reduction is as follows. Test data are subdivided into five separate input files due to the volume of information. The HOTLIPS command file supervisor is maintained as a separate file. The information produced by HOTLIPS is either directed to the screen or kept in output data and plot files for later generation of hard copy. A processing reflection file is generated showing program diagnostics or error messages produced by HOTLIPS. This is useful if difficulties are encountered during an execution.

2.3 Command Structure

HOTLIPS is controlled by a command file invoking the various capabilities of the program for a given execution. Modifying the command file modifies the actions performed by HOTLIPS over a given set of test data. The command file allows probe-level requests for tables and plots and

---

*DISSPLA is a proprietary graphics package of Computer Associates, Inc., of Sorrento Valley, CA.

†LOTUS 1-2-3 is a proprietary computer program for the IBM-PC produced by LOTUS Development Co., Inc.

probe-family-level requests for tables and plots. The probe-family-level applies to both SCISR and SCDP flow surface representations. A key feature of the command file is the "DO LOOP" statement allowing repetitive tasks such as the computations performed on probes to be defined by a minimum number of command statements. The command file also facilitates data selection through "dummy" read statements (usually in DO LOOPs) skipping the unwanted data within a given sequential file.

An algorithmic representation of the command file is given in Fig. 4. The probe-family-level function of HOTLIPS are referred to in Fig. 4 (and in the remainder of the report) as SCISR functions.

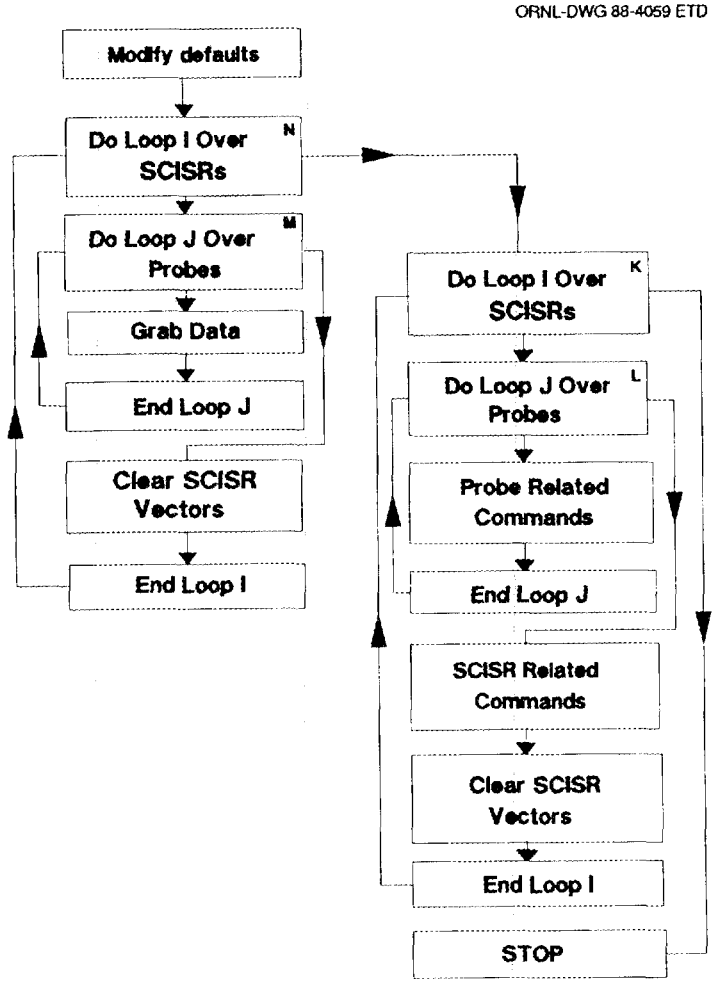

Fig. 4. Schematic of the HOTLIPS command file.

2.4 Data Analysis Procedures

Not all 680+ probes of the 43 flow surface determinations were of usable quality. Only 606 were included in the final analysis after considerable effort to inspect the data and to remove the unusable probes. The first rule for elimination of probes was that the probe must have at least 30 readings; some did not. Other rules eliminated probes on the basis of poorness-of-fit for the representations of elastic and plastic portions of the response. And finally all probes were inspected on the basis of their value of Ω_{max} (Ω when strain rate was 100 $\mu\epsilon$/min). Outliers were removed.

In fact, very little data were actually eliminated, which is consistent with the investigative nature of this early study. At some later time it may be possible to devise better criteria for data elimination. Certainly, it would be preferable to estimate probe quality at the time of test so that the poorer probes could be repeated and thus the SCISR data set not compromised with low quality data. Perhaps information from this study will help guide future test improvements in this area.

The assumptions of the data analysis procedures are given below. Some assumptions are obviously valid while others are substantiated in the results shown.

At the probe level the following assumptions are utilized:

1. There is assumed a distinct breakpoint t_0 or threshold time separating elastic and inelastic behavior. Each probe begins with elastic responses for both components of strain; then, at the breakpoint, both strain components enter the inelastic regime.
2. The elastic portion of the probe (prior to the breakpoint) is assumed fully characterized by two constants, E and G, where E is the least-squares fit of the linear portion of σ_{11} vs ϵ_{11} and G the fit of σ_{12} vs $2\epsilon_{12}$.
3. For the inelastic regime both components of strain rate are assumed to have a zero value at t_0 and then to increase (in value) in a linear fashion with time after t_0.
4. Finally, for every probe it is assumed that inelastic strain is the difference between measured total strain and calculated elastic

strain, and that the inelastic components can be calculated using Hook's law for an isotropic material as

$$\epsilon_{11}^{p} = \epsilon_{11} - \sigma_{11}/E \tag{21}$$

and

$$\epsilon_{12}^{p} = \epsilon_{12} - \sigma_{12}/2G \ . \tag{22}$$

Here ϵ_{11} and ϵ_{12} are the measured total strains, and σ_{11} and σ_{12} are the measured stresses. E and G are the computed elastic constants for the probe.

These four assumptions allow the following statements to be made for a given probe. (Remember that $\dot{\sigma}_{11}$ and $\dot{\sigma}_{12}$ are both constant-valued for a probe.) First, the plastic strain components are proportional to t^2

$$\epsilon_{ij}^{p} \ \alpha \ t^2 \ , \tag{23}$$

where t is time after t_0. The J_2 measure of inelastic strain rate is given by

$$\bar{\dot{\epsilon}}^{p} = \sqrt{C_{11}^2 + 4C_{12}^2/3}\ t \ , \tag{24}$$

where $C_{11} = \dot{\epsilon}_{11}^{p}/t$ and $C_{12} = \dot{\epsilon}_{12}^{p}/t$ are akin to constant accelerations. The Ω term simplifies to the following

$$\Omega = (\dot{\sigma}_{11}C_{11}/2 + \dot{\sigma}_{12}C_{12})t^2 \ . \tag{25}$$

And, it is clear that Ω is related to the square of J_2-strain rate as

$$\Omega = \frac{(\dot{\sigma}_{11}C_{11}/2 + \dot{\sigma}_{12}C_{12})}{(C_{11}^2 + 4C_{12}^2/3)} \ (\bar{\dot{\epsilon}}^{p})^2 \ . \tag{26}$$

At this point an additional theoretical note is offered. It may be shown that for a fully isotropic "J_2 material" (C = 0), the SCDP surfaces are also SCISR surfaces. Using this statement in conjunction with Eq. (26), it is pointed out that the quotient on the right-hand side should

have a fixed constant value for all probes of a flow surface determination if the surface is a J_2 surface.

For the 43 tests, each with a collection of probes, the SCISR and SCDP surfaces are fitted by ellipses in the axial-torsional stress space. The major and minor ellipse axes and the σ_{11} and σ_{12} locations of the center of the ellipse constitute a four-parameter family which can be determined in a least-squares fashion. For any flow surface the 16 data points, composed of (σ_{11}, σ_{12}) pairs for the 16 probes, are the readings for which the state variable ($\bar{\dot{\epsilon}}^p$ for the SCISR or Ω for the SCDP) is calculated to have the specified constant value.

The four-parameter family for the ellipse is then used to help quantify terms of the expanded flow surface with a form given earlier in Eq. (13),

$$F = \frac{(J_2^3 - CJ_3^2)^{1/3}}{\kappa^2} - 1 \ .$$

For example, the center of the ellipse quantifies the internal stress, a_{ij} involved in J_2 and J_3. a_{ij} is produced by the preloading but remains "nearly" constant during probing. Furthermore, the ratio of the major to minor ellipse axes, $\overset{*}{\sigma}_{11}$ and $\overset{*}{\sigma}_{12}$, helps determine C of Eq. (13). If $\overset{*}{\sigma}_{12}/\overset{*}{\sigma}_{11}$ approaches $\sqrt{3}$ as a representative number, the surface is essentially a von Mises (or J_2) surface and the correct value for C is C = 0. If $\overset{*}{\sigma}_{12}/\overset{*}{\sigma}_{11} > \sqrt{3}$ then C takes on negative values showing that the J_3 contribution produces a higher shear-to-axial "flow stress" ratio than a von Mises material. Likewise, if $\overset{*}{\sigma}_{12}/\overset{*}{\sigma}_{11} < \sqrt{3}$ then C takes on positive values and the material has a lower shear-to-axial "flow stress" ratio than a von Mises material. For historical example, Tresca characterized C to have a value of +4 for certain materials and temperatures; Drucker[2] characterized C as +2.25 for other materials. For the type 316 stainless steel of this study, a positive value of C is suggested by the data, at least for the temperature of 650°C.

2.5 HOTLIPS Data Reduction at the Probe Level

Data reduction tasks performed for a given probe are controlled by a series of supervisory command statements. These tasks are as follows.

Probe data are first read from the test data file and stored in five arrays for t (time), σ_{11}, σ_{12}, ϵ_{11}, and ϵ_{12}. The axial stress rate and the shear stress rate are computed using least square fits of the linear portions of the relationships σ_{11} vs t and σ_{12} vs t. The effective stress rate is then calculated by the J_2-relation

$$\bar{\dot{\sigma}} = \sqrt{\dot{\sigma}_{11}^2 + 3\,\dot{\sigma}_{12}^2} \tag{27}$$

and compared with the nominal value "applied" during the probing ($\bar{\dot{\sigma}} = 10$ ksi/min for all probes). A warning message is sent to the reflection file when the comparison is poor. Young's and shear moduli (E and G) are then computed in a least-squares fashion as earlier detailed. The axial and shear inelastic strains are next determined from Eqs. (21) and (22). In another task the effective plastic strain is calculated for each reading using the J_2-form

$$\bar{\epsilon}^p = \sqrt{(\epsilon_{11}^p)^2 + 4/3(\epsilon_{12}^p)^2}\ . \tag{28}$$

Once these tasks are performed, HOTLIPS determines the precise breakpoint of inelastic behavior as detailed in the next section.

2.6 Determination of the Threshold of Inelastic Response

Recall that we assumed that each probe contained elastic readings followed by inelastic readings separated at a distinct breakpoint t_0. Further, we assumed a common breakpoint for both components of the inelastic strain vector. The procedure adopted to find t_0 is one of isolating the point of departure-from-linearity of the strain $\bar{\epsilon}^p$. (Though we chose the J_2-form to combine the components into a representative scalar quantity, we contend that the process for isolating t_0 is not sensitive to this assumption; for example, a simple root-mean-squares scalar representation produces the same t_0 isolation.) Also, it is important to note that because of the observed scatter in the E and G representations, we decided it was inappropriate to impose an assumption of zero-slope on the linear portion of the $\bar{\epsilon}^p$ vs time curve as would seem reasonable using strict theoretical arguments. Rather we relaxed this assumption allowing the data

representations to have the best straight-line fit regardless of slope. (All resulting slopes were small compared to 100 $\mu\epsilon$/min, as expected.)

In the algorithm adopted, the selection process for isolating the precise point of departure-from-linearity becomes one of investigating a series of candidate least squares lines. In the process, the best representation of the elastic portion of $\bar{\epsilon}^p$ vs time results and the departure point is found. Twenty candidate lines are considered in which each contains a different number of readings from the probe. First, all but the last 5 readings are included; then, all but the last 6; and so forth down to all but the last 25. The correct selection for the t_0 reading was generally somewhere between the 25th-removed and the 5th-removed-from-last reading. This is true because of the standard scan rate employed as related to the constant stress/load rate of the radial probes and the similar size and position of all flow surfaces determined. Based on the scatter of probe readings around the candidate lines, a criterion was developed to select the one line that is the best and thus to pinpoint t_0.

Because this method is rather empirical, all results were plotted and studied to "visually" confirm that the selected points were sensible. When the $\bar{\epsilon}^p$ vs time response oscillated (as occasionally it did), the selection process produced a systematic choice for t_0 which can be argued to be the "best" choice, or at least a consistent choice.

2.7 Representation of Inelastic Strain Response

All probe readings prior to t_0 are discarded in the inelastic representations. Each component of inelastic strain is fitted vs time with a least-squares parabola. As mentioned earlier, we assumed that the peak of the parabola occurs at t_0 (thus, the component strain rates are zero at t_0). The fitting process forces compliance with this assumption.

2.8 Determination of Inelastic Strain Rate and Dissipation Potential for the Probe

Once the components of inelastic strain are represented as functions of time as in Sect. 2.7, it then becomes a very simple matter to represent

both effective inelastic strain rate and dissipation potential. $\bar{\dot{\epsilon}}^p$ is calculated using Eq. (24); Ω comes from Eq. (25).

To reconfirm earlier SCISR representations (Ref. 8), three different probe times t_0, t_{50}, and t_{100} are identified, one each for 0, 50, and 100 $\mu\epsilon$/min rates. This information and the corresponding (σ_{11}, σ_{12}) pairs are kept in memory for later use in SCISR flow surface determinations.

The process of choosing representative Ω values is more complicated since each probe reached a different value of Ω_{max}. It was decided to select three different probe times for three different Ω values. First $\Omega = 0$ is selected. (Incidentally, this is precisely the same probe time as for a zero inelastic strain rate.) The largest representative value of Ω is chosen as 1/3 of the average of all Ω_{max} values for the 16 (at most) probes of the sequence, $\bar{\Omega}_{max}/3$. The intermediate value is chosen as 1/6 of the average. As with SCISR values, the SCDP values produce different probe times which are solved for using Eq. (25). As a nomenclature convention the three times of each SCDP probe are also referred to as t_0, t_{50}, and t_{100} for 0, 50, and 100% of $\bar{\Omega}_{max}/3$. The three Ω values and corresponding (σ_{11}, σ_{12}) pairs are likewise kept in memory for later use in SCDP flow surface determinations.

2.9 Probe-Level Plotting

The types of plots generated by HOTLIPS can be grouped in two different categories, probe-level plots and surface-level plots. The list of probe-level plots is as follows:

σ vs t

τ vs t

ϵ vs t

$\gamma/2$ vs t

σ vs ϵ

τ vs $\gamma/2$

ϵ^p_{11} vs t

ϵ^p_{12} vs t

$\bar{\epsilon}^p$ vs t

In the above nomenclature $\sigma = \sigma_{11}$, $\tau = \sigma_{12}$, $\epsilon = \epsilon_{11}$, and $\gamma = 2\epsilon_{12}$. Plots of data points alone or with least-square fits can be obtained. Examples of these nine types are shown as Figs. 5–13. If all probe-level plots of the data were constructed, over 12,000 figures would result. This was not done in the current study. After studying many examples, it was determined that the data reduction process described in 2.4–2.8 was adequate, and that visual inspection of all probe-level data was unnecessary.

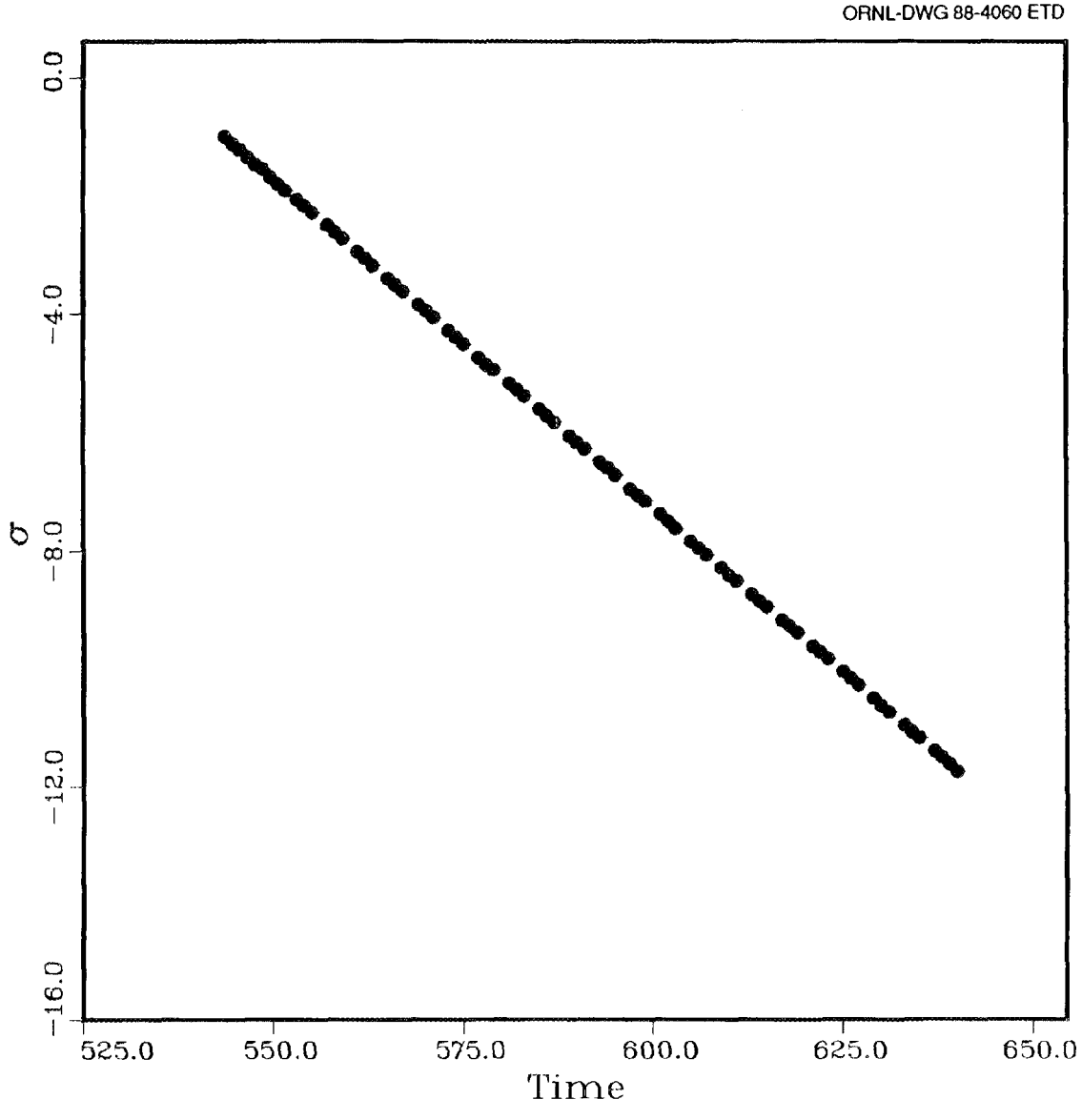

Fig. 5. Typical probe plot of σ vs time.

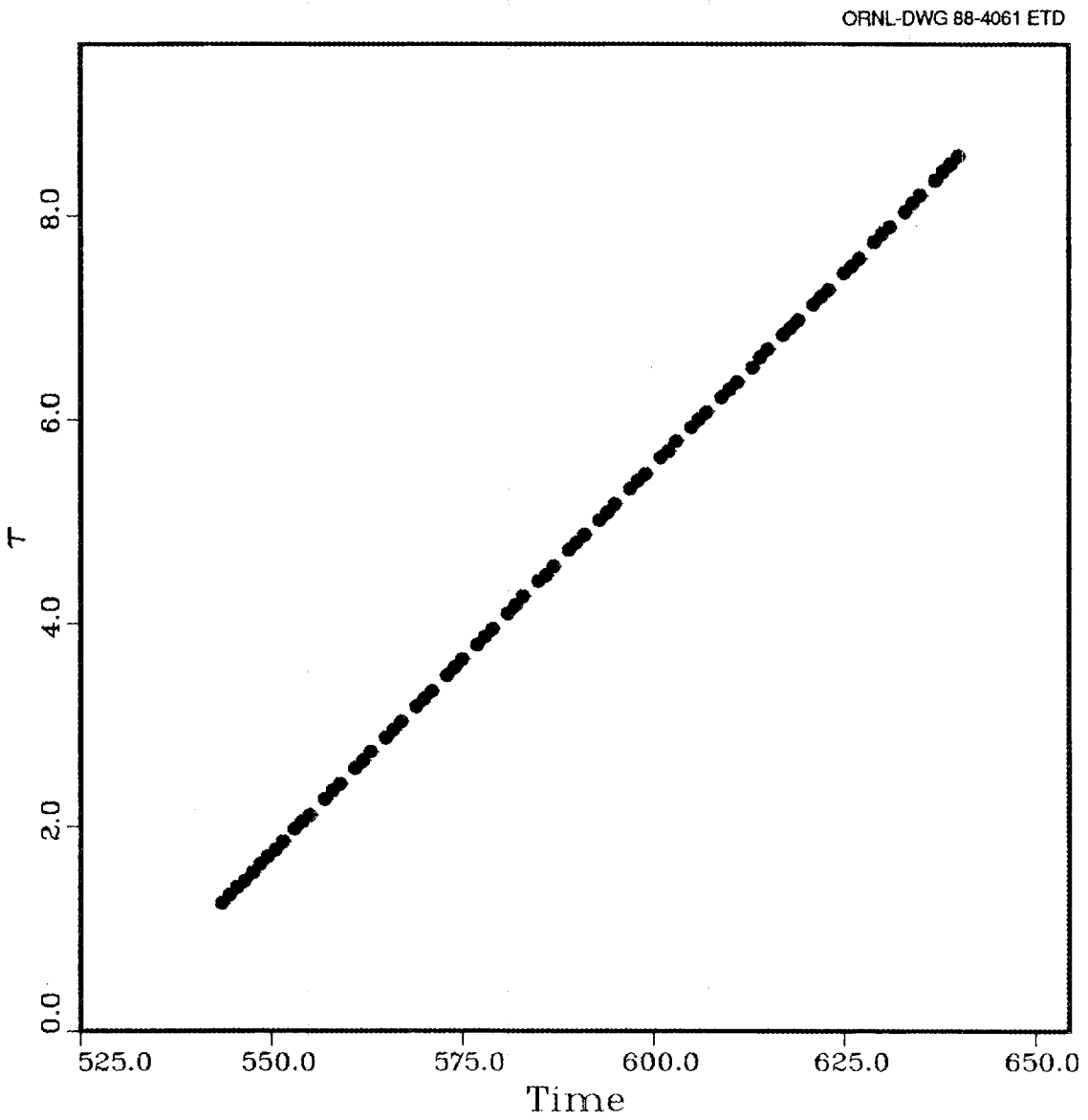

Fig. 6. Typical probe plot of τ vs time.

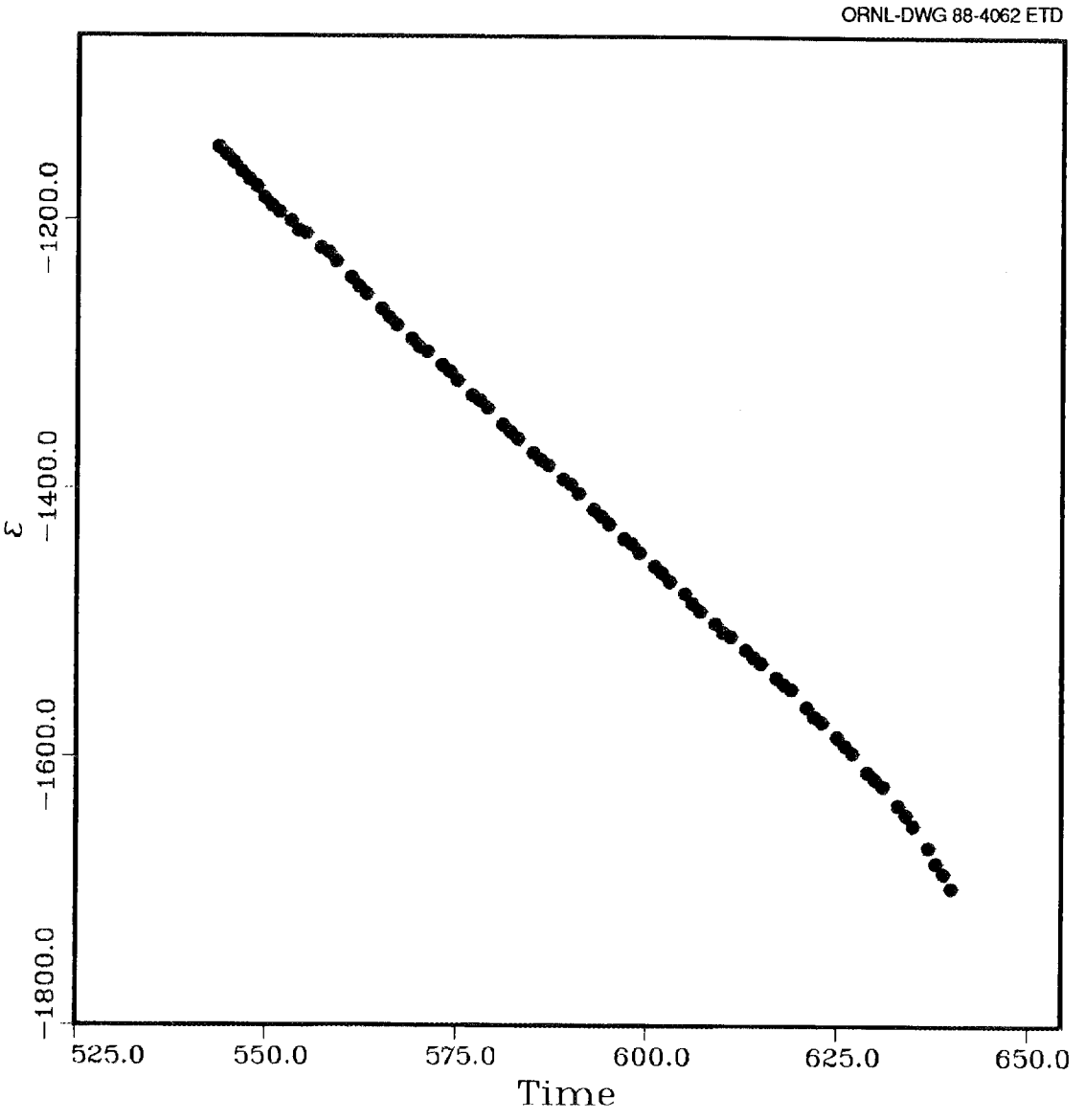

Fig. 7. Typical probe plot of ϵ vs time.

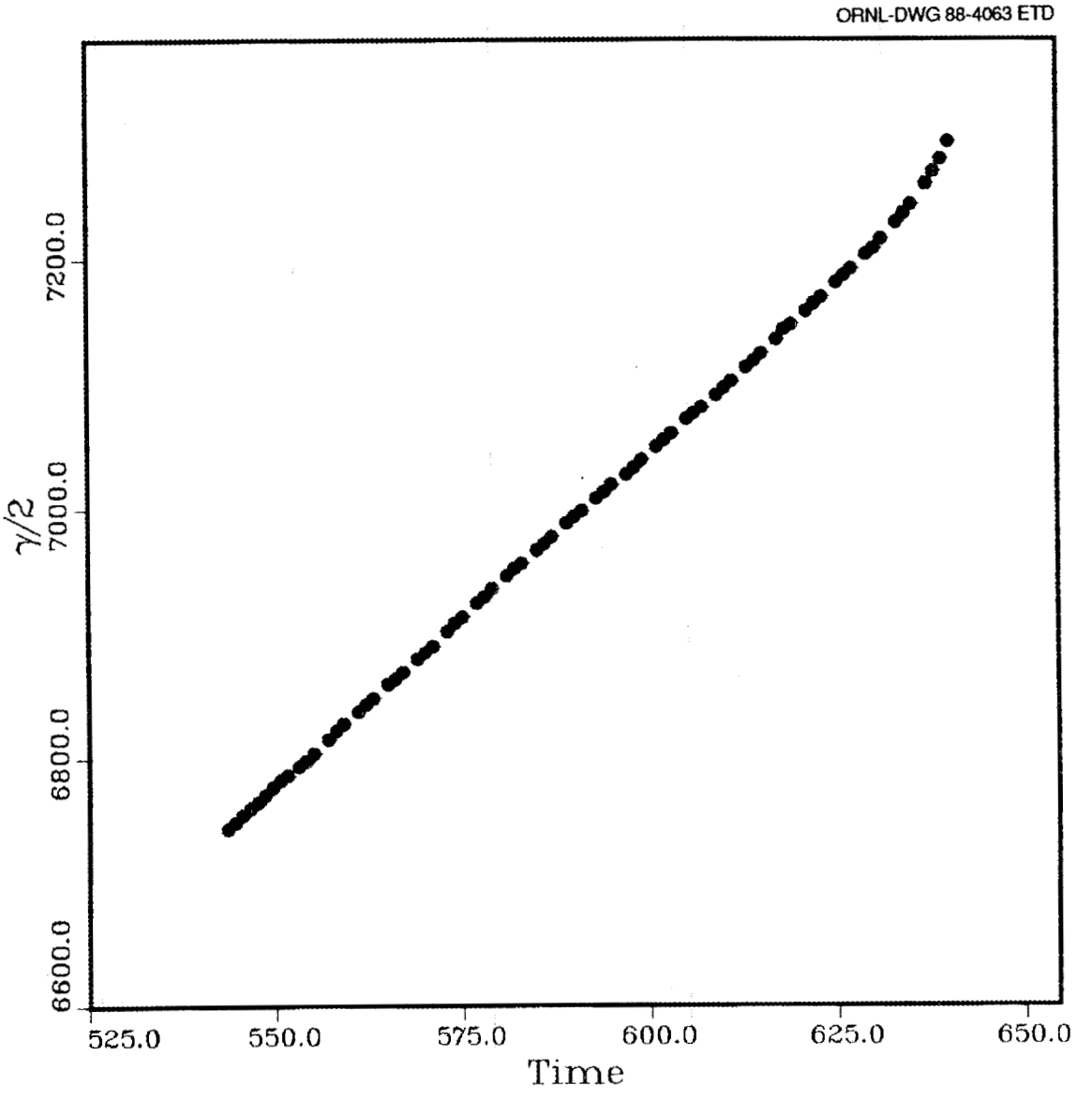

Fig. 8. Typical probe plot of $\gamma/2$ vs time.

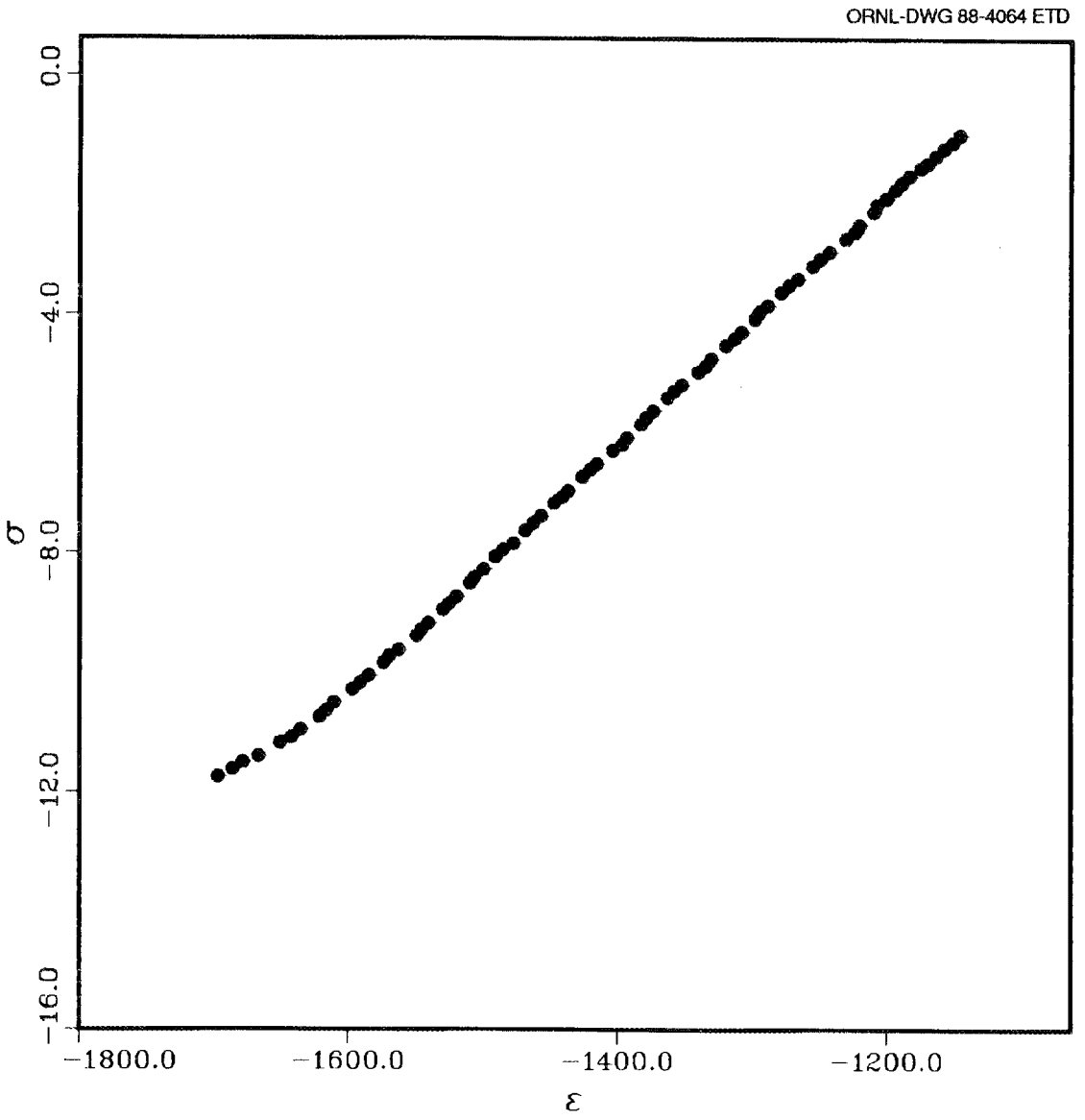

Fig. 9. Typical probe plot of σ vs ϵ axial stress-strain response.

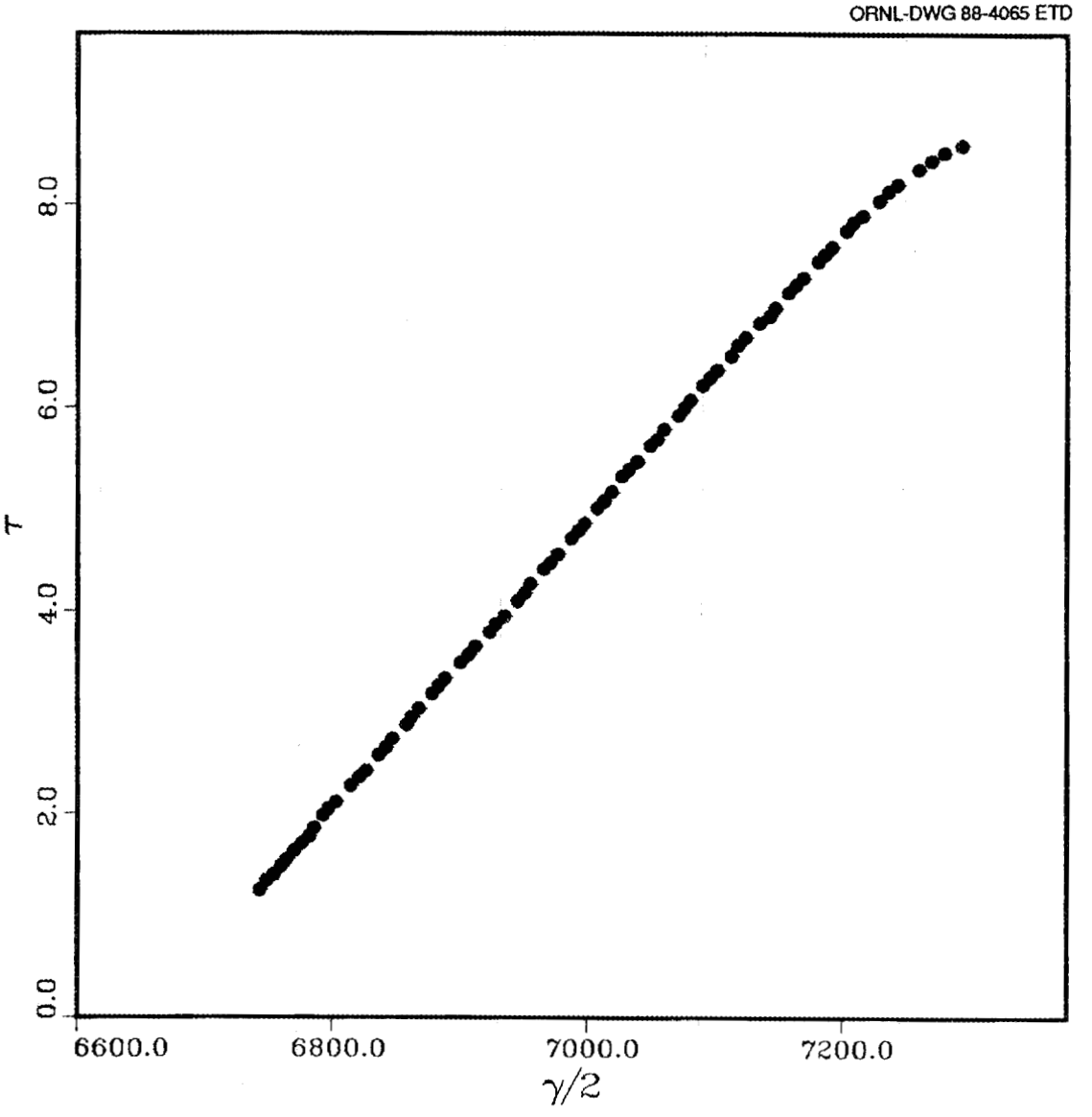

Fig. 10. Typical probe plot of τ vs $\gamma/2$ shear stress-strain response.

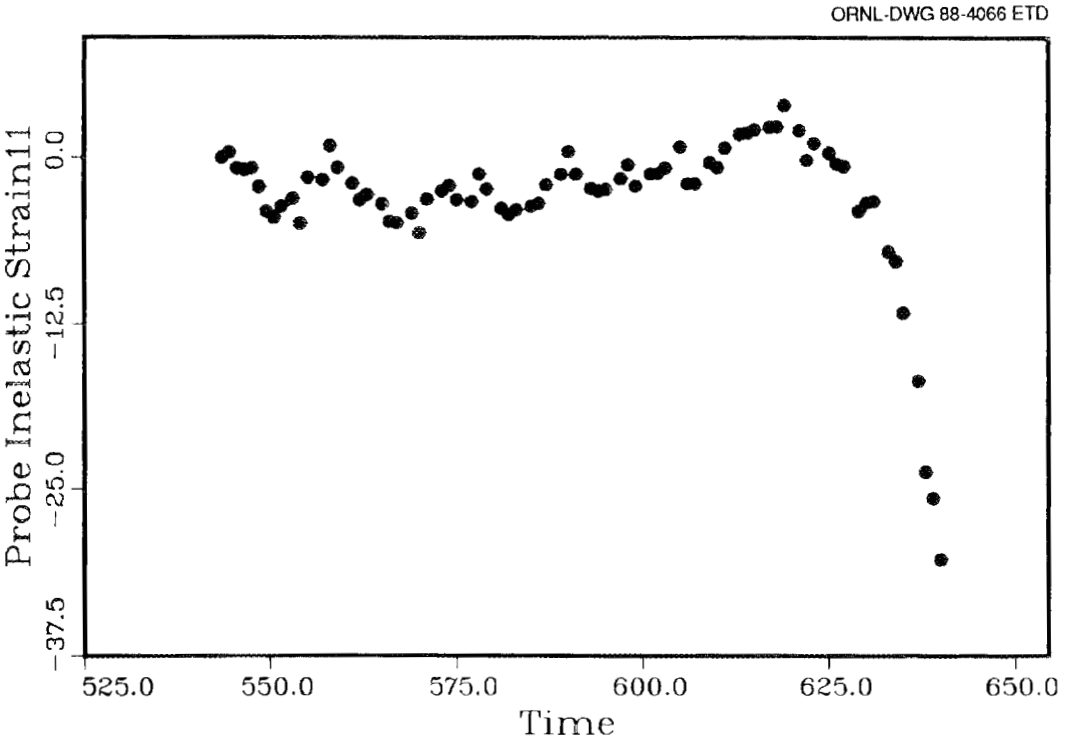

Fig. 11. Typical probe plot of ϵ_{11}^{p} vs time.

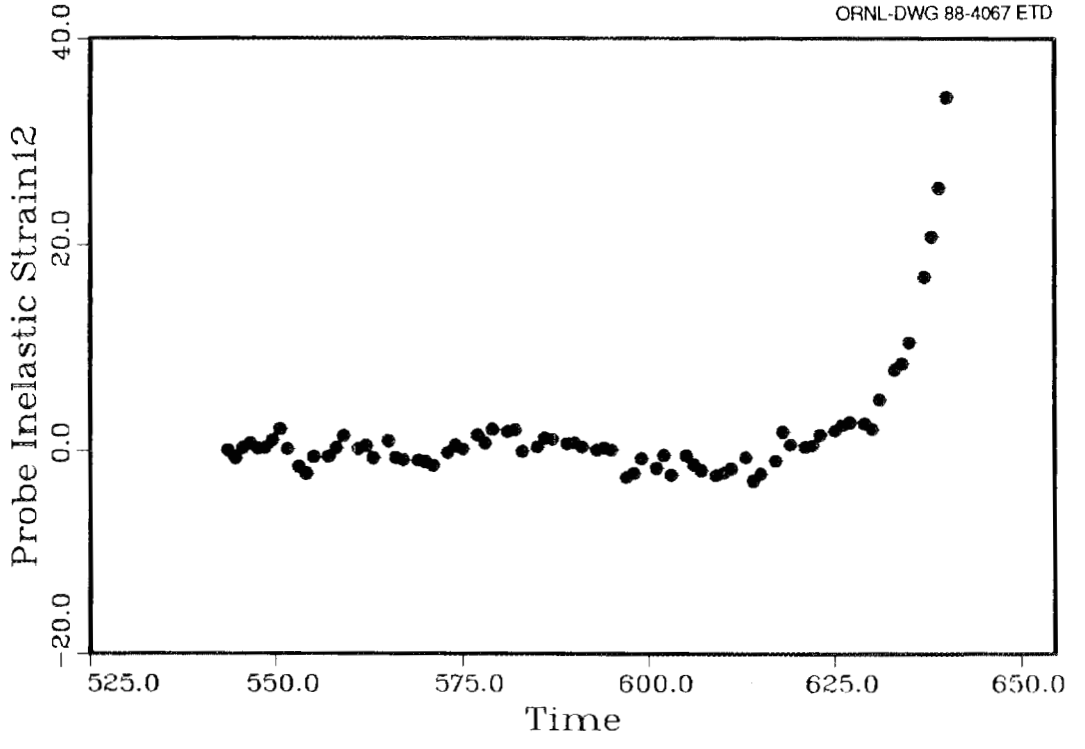

Fig. 12. Typical probe plot of ϵ_{12}^{p} vs time.

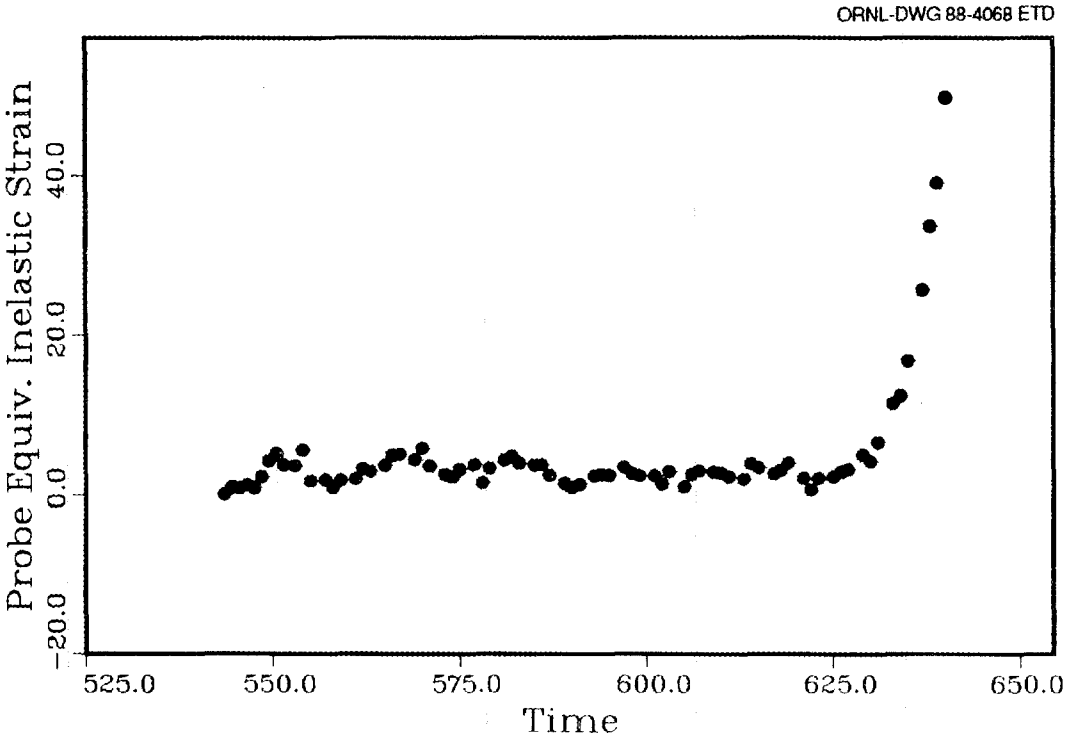

Fig. 13. Typical probe plot of $\bar{\epsilon}^p$ vs time.

2.10 Representation of Flow Surfaces

Surface-level plots generated by HOTLIPS are:

- Ellipse fit of SCISR
- Ellipse fit of SCDP
- Ellipse fit for a specific Ω value
- CPPS (cubic parametric periodic spline) fit of SCISR
- CPPS fit of SCDP
- Ω vs t for the probe family
- Ω vs $\bar{\epsilon}^p$ for the probe family

Ellipse fit and CPPS fit of SCISR and SCDP surfaces can be obtained for all combination of the three times (t_o, t_{50}, and t_{100}). Examples of these seven types of surface-level plots are shown as Figs. 14–20. Some additional SCDP plots are included in Appendix A. Other surface-level plots can be produced by inserting related plot request commands in the SCISR subsection of the command supervisor.

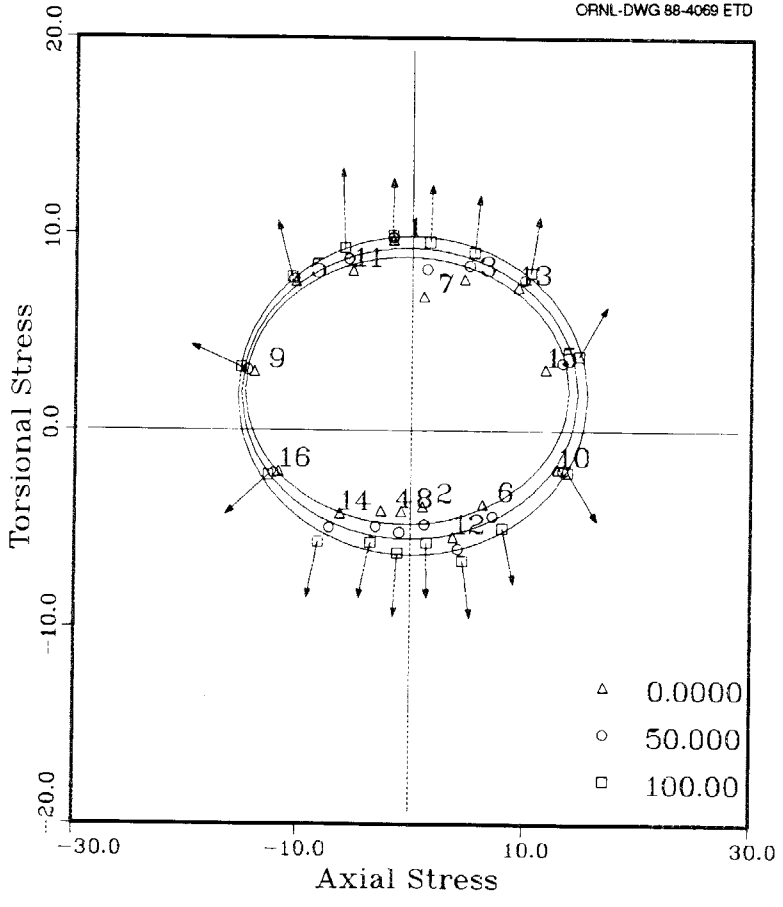

Fig. 14. Typical flow surface plot of a SCISR ellipse fitted to data.

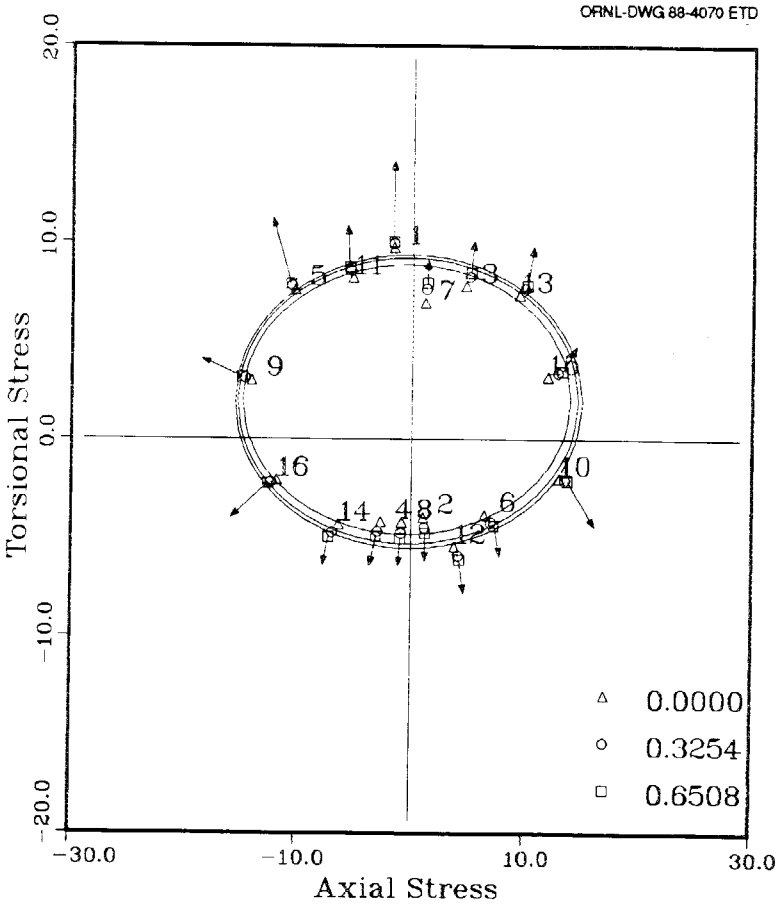

Fig. 15. Typical flow surface plot of a SCDP ellipse fitted to data.

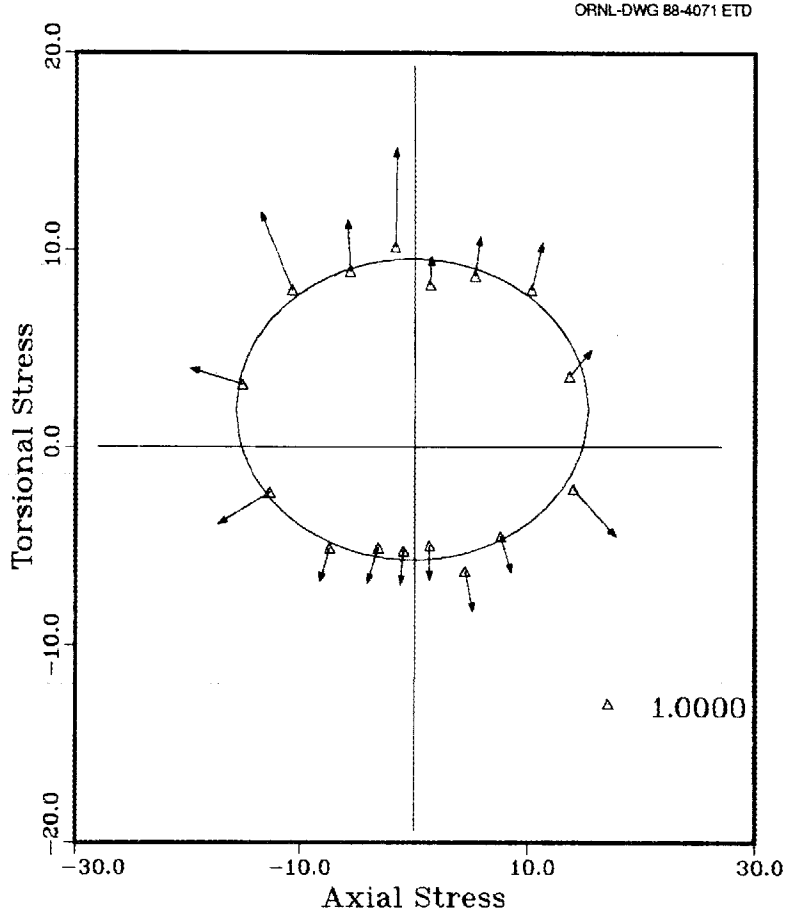

Fig. 16. Typical flow surface plot of a SCDP ellipse fitted for data with a specific Ω value.

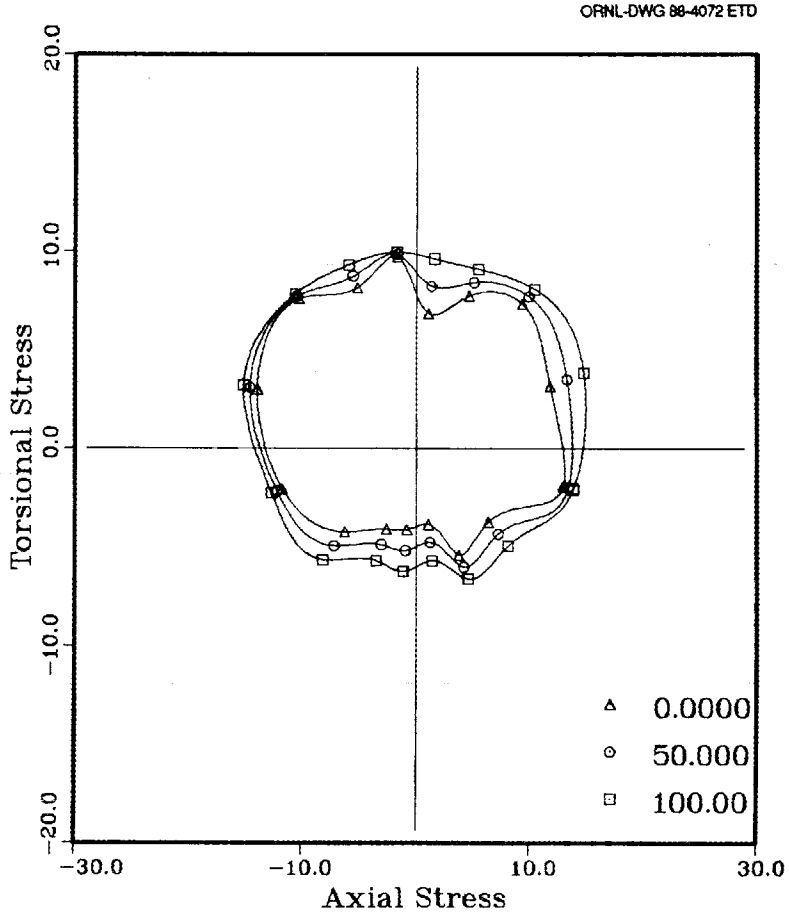

Fig. 17. Typical CPPS spline fit for SCISR data.

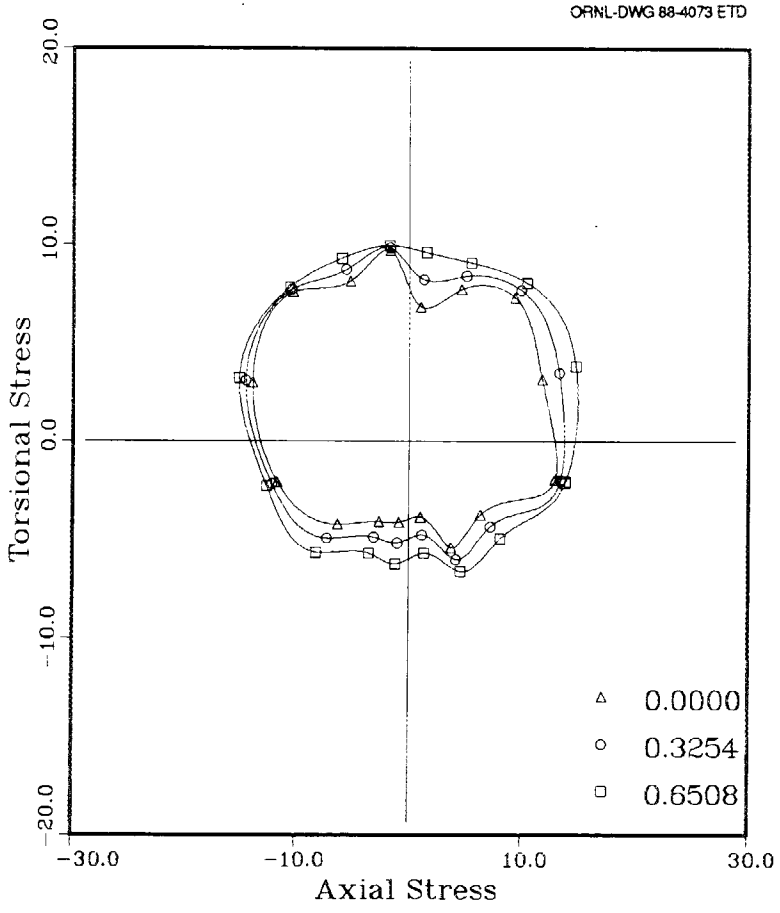

Fig. 18. Typical CPPS spline fit for SCDP data.

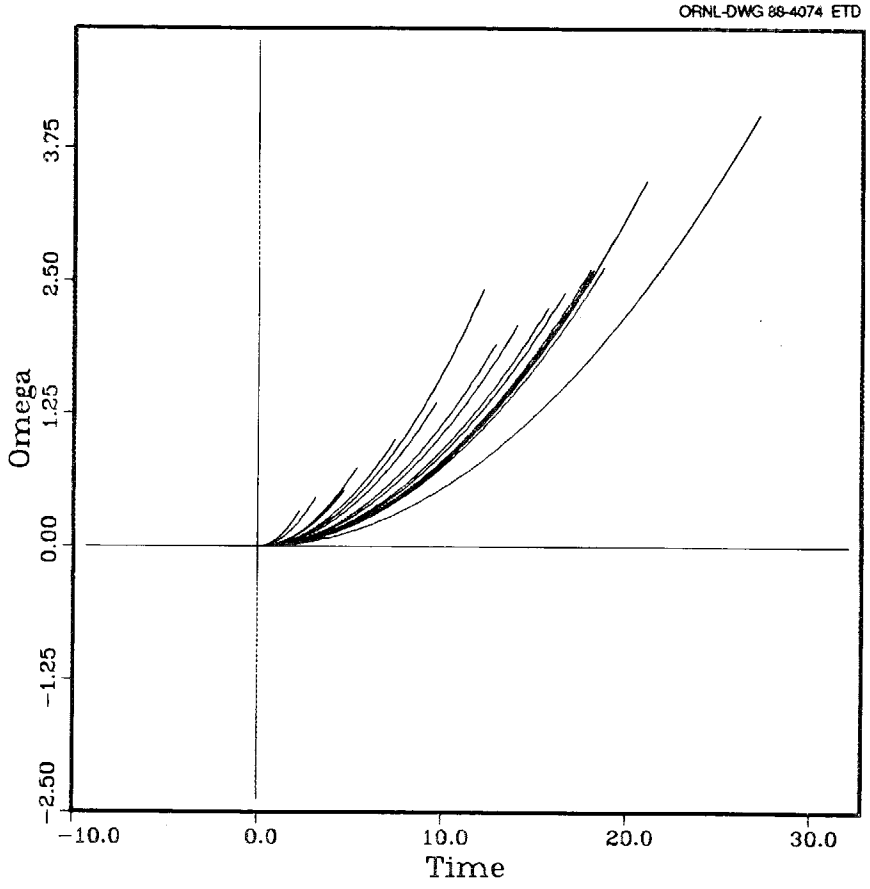

Fig. 19. Typical family of Ω vs time traces for all probes of a flow surface determination.

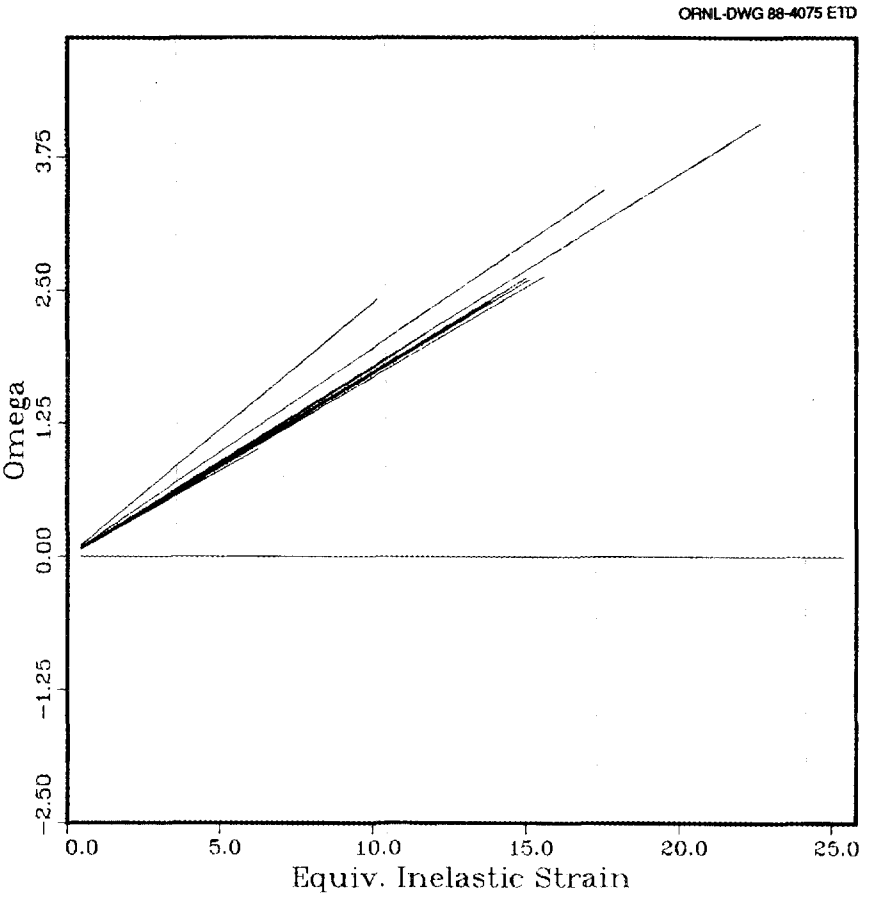

Fig. 20. Typical family of Ω vs $\bar{\epsilon}^p$ traces for all probes of a flow surface determination.

SCISR and SCDP surfaces can be generated using two different fitting schemes as seen in the example Figs. 16 and 17. The first scheme is the fit of probe data by an ellipse. This fit is a four parameter residual minimization scheme. The four parameters are the major and minor ellipse axes and the axial and shear ellipse center. The second scheme of surface fit is the cubic parametric periodic spline fit. This scheme, abbreviated to CPPS, is a spline characterized by two facts: the fit interpolates to every data point and the slope is continuous at every data point.

3. SUMMARY OF RESULTS AND FINDINGS

First the information relative to probe level responses must be presented and discussed before it is appropriate to consider resulting representations of the flow surfaces. From this presentation comes validation of the assumptions of the probe-level data reduction methodology presented in the previous section.

Because testing variability was discovered to be systematically related to the probe direction, much of the probe-level data are presented vs an angular term β which is related to the inverse-tangent of $\dot{\sigma}_{12}/\sqrt{3}/\dot{\sigma}_{11}$. β of the study is defined to vary from 0° to 360° in a counterclockwise fashion as the angle sweeps the first through fourth quadrants of the $(\sigma_{11}-\sigma_{12})$ plane. β angles are such that pure axial loading occurs at 0° and 180°, while pure torsional loading occurs at 90° and 270°. The 16 distinct probe angles used in the study are given in Table 3.1. Each of the 43 flow surface determinations was carried out in the same sequence, 1–16.

Table 3.1. Probing sequence vs β angle

Probe sequence	β (°)	Probe sequence	β (°)
1	96	9	162
2	276	10	342
3	70	11	111
4	251	12	291
5	130	13	52
6	310	14	232
7	84	15	21
8	265	16	201

Note that consecutive probes (such as 1–2, 3–4, 9–10, etc) are 180° out-of-phase.

3.1 Elastic Responses for Probes

As earlier stated E and G were determined probe-by-probe as the least-squares fits to the linear portion of the σ_{11} vs ϵ_{11} and σ_{12} vs $2\epsilon_{12}$ responses respectively. The computed E's determinations for the 606 probes

are shown vs β in Fig. 21, and the corresponding values for "coefficient of correlation" ($R = \sqrt{\text{explained variation/total variation}}$) are shown in Fig. 22. E has a mean value of 20.9×10^6 psi and a standard deviation of 2.9×10^6 psi. Scatter in E is concentrated around β angles near the shear axis at 90° and 270° where axial strain is small. Figure 21 also shows that the scatter is fairly balanced, plus and minus, around the mean value. Figure 22 gives a representation of the goodness-of-fit. The average value of R is 0.9942 with a standard deviation of 0.02. Only a few probes display a poor linear correlation for E; these are again concentrated around 90° and 270°.

Turning to the elastic shear responses, Fig. 23 shows the computed G's for the 606 probes while corresponding R values are in Fig. 24. G has a mean value of 14.6×10^6 psi with a standard deviation of 1.5×10^6 psi. Scatter in G is concentrated around β angles near the axial axis at 0° and 180° where shear strain is small. The scatter is fairly balanced. Figure 24 shows that the linear fit is everywhere quite good. The average value of R is 0.9997 with a standard deviation of 0.0006. The G fits, though nearly perfect regardless of the β angle, show a small degradation in R near 0° and 180°, as expected.

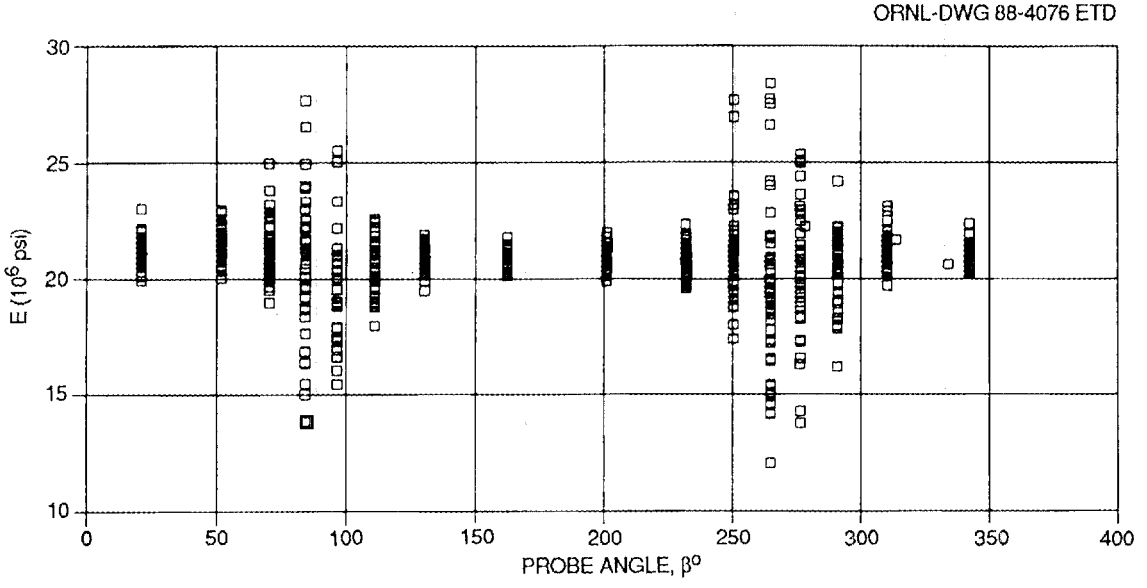

Fig. 21. Computed elastic moduli for 606 probes plotted against probe angle.

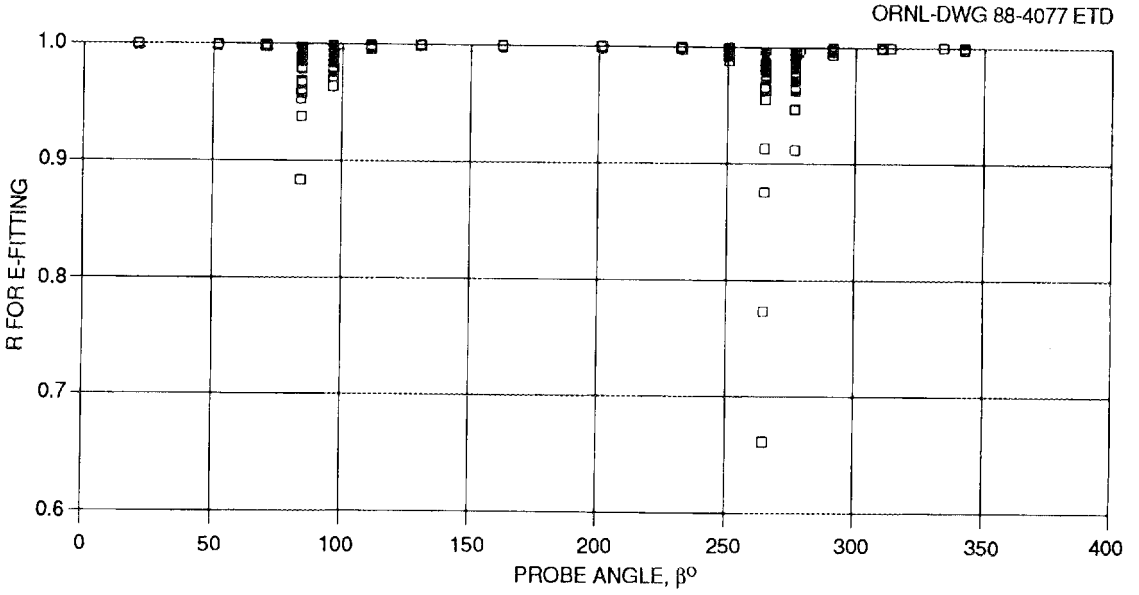

Fig. 22. R, the coefficient of correlation, for the elastic moduli of Fig. 21.

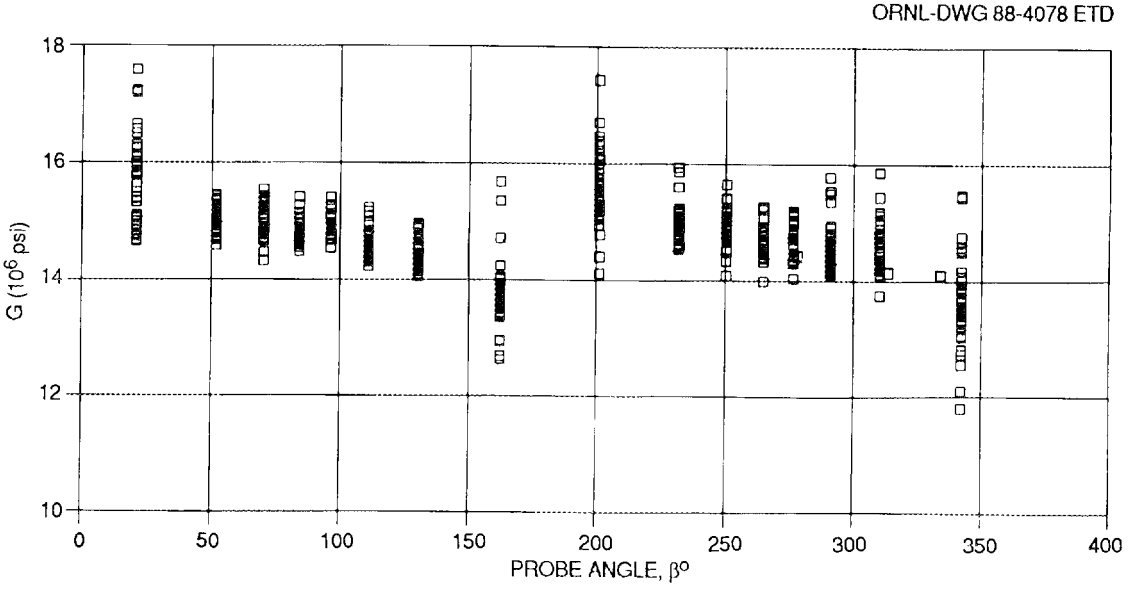

Fig. 23. Computed shear moduli for 606 probes plotted against probe angle.

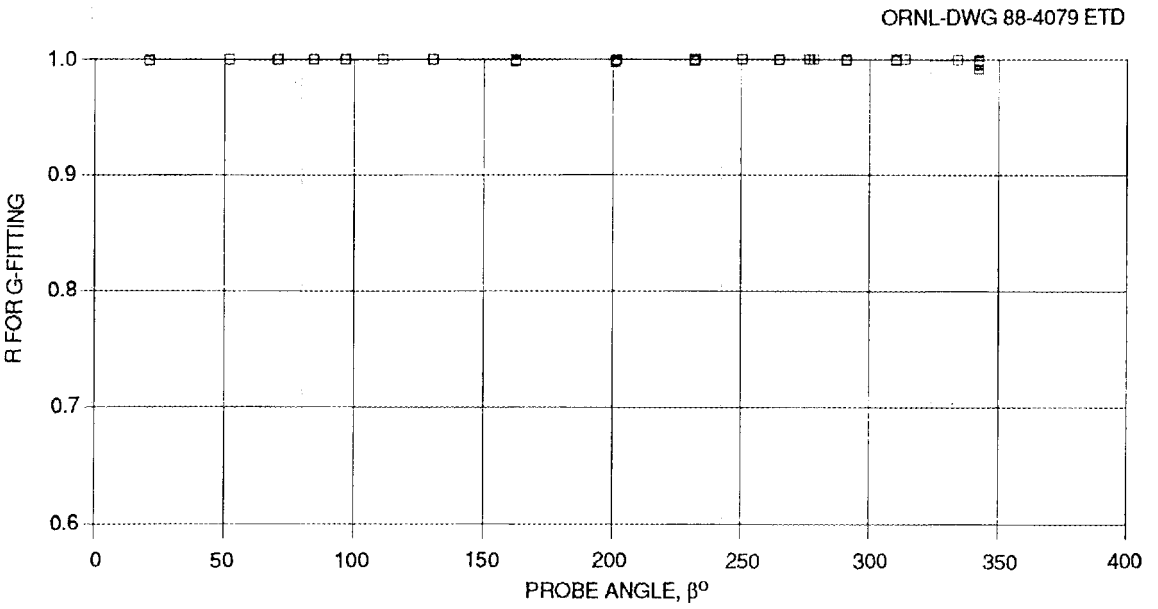

Fig. 24. R, the coefficient of correlation, for the shear moduli of Fig. 23.

In general we conclude that the elastic responses, E and G, are successfully determined by the data reduction method. Certainly there is evidence that G is more successfully determined than E for the full range of probe angles. Scatter in all elastic quantifications is concentrated in regions where strain is small.

3.2 Inelastic Strain Responses for Probes

The components of the inelastic strain response vs time were fitted with parabolas as earlier discussed. The success of this method can be judged by examination of the R values as seen in Fig. 25 for ϵ^{p}_{11} and in Fig. 26 for ϵ^{p}_{12}. R for the axial fit has a mean value of 0.82 and a standard deviation of 0.24. R for the shear fit has mean value of 0.956 and a standard deviation of 0.12. Scatter, as with the elastic responses, is systematic in β. Shear strain is apparently more successfully measured than axial strain ... at least it is better-represented by a parabolic relationship. Study of the plots of various probe-level inelastic strain fits shows that data scatter in regions of small strain is considerable; thus, it is believed of no advantage to employ higher order polynomials.

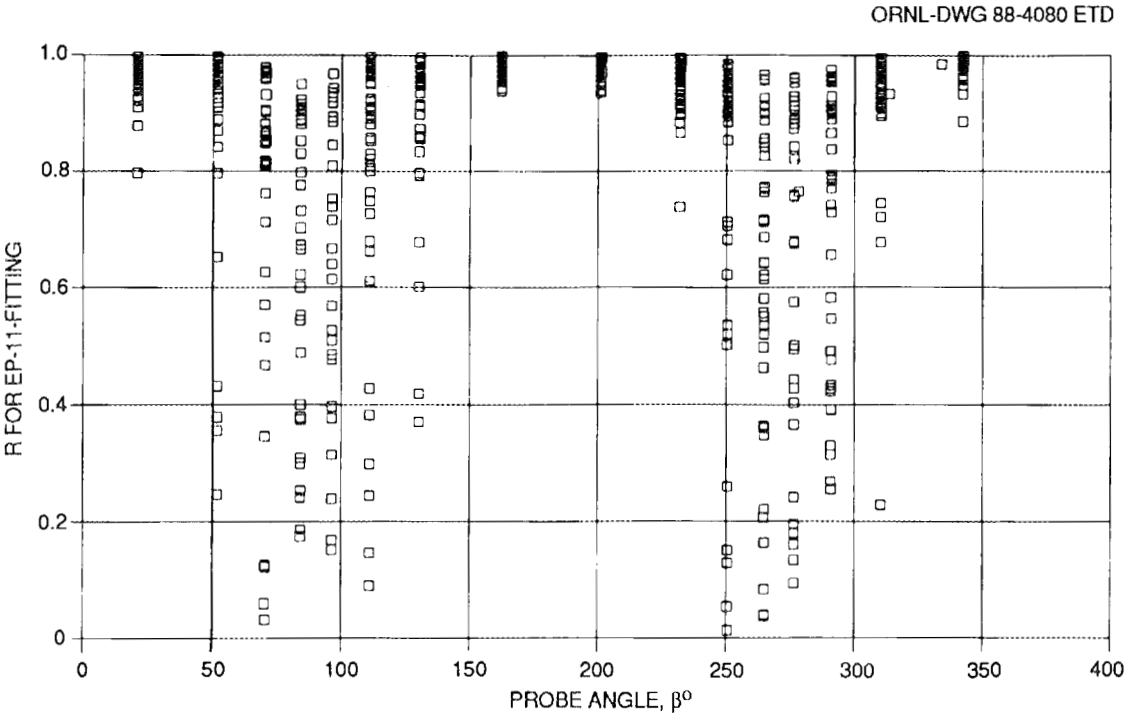

Fig. 25. R's for the fitted parabolas of axial inelastic strain plotted against probe angle.

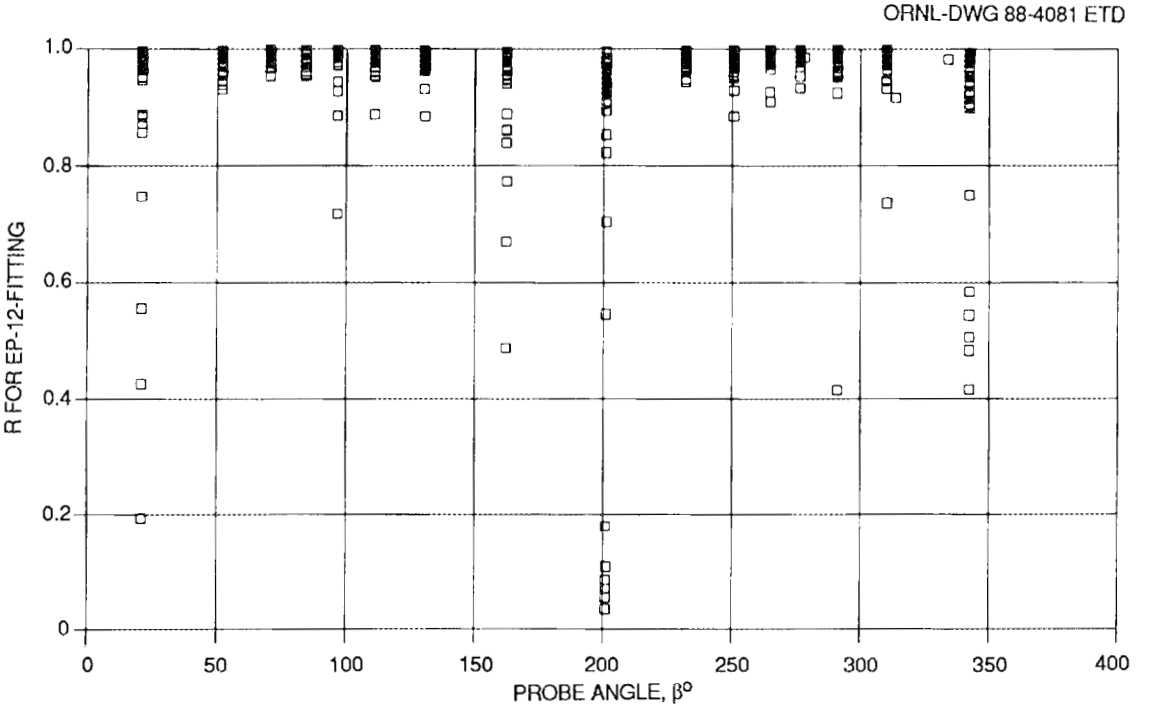

Fig. 26. R's for the fitted parabolas of shear inelastic strain plotted against probe angle.

In regions of large strain where scatter is not large, the parabolic representations appear quite adequate. Thus, we conclude then the data reduction methodology cannot be greatly improved upon for the representation of inelastic strain responses.

As was pointed out in presenting Eqs. (23)–(26), the coefficients on the t^2 terms of the fitted parabolas, C_{11} for $\dot{\epsilon}^p_{11}$ vs time and C_{12} for $\dot{\epsilon}^p_{12}$ vs time, are akin to constant accelerations. C_{11} and C_{12} are further studied using Figs. 27 and 28 respectively where the independent variable is the probe angle. All 606 probes are included. The data for C_{11} are best described as a $\cos\beta$ function with an amplitude of 0.0563 $\mu\epsilon/\text{sec}^2$. The data for C_{11} are best described as a $\sin\beta$ function with an amplitude of 0.071 $\mu\epsilon/\text{sec}^2$. The data for C_{11} and C_{12} are normalized by 0.0563 $\cos\beta$ and 0.071 $\sin\beta$ and plotted against the $\log(1 - R)$ for the probe fits in Figs. 29 and 30. The use of the $\log(1 - R)$ is to spread out the data with $R = 0.999$ corresponding to -3 and $R = 0.99$ corresponding to -2, etc. In these two plots we have the worst fits toward the right side of the figures. It is easy to see that C_{12} is much better described than C_{11}. All negative values for the normalized C_{11} and C_{12} most probably represent fallacious representations caused by oscillatory data scatter. Such oscillations might occur due to electronics problems in the data system's front-end and/or to inadequate precision to measure very small strain values.

3.3 Ω Responses for Probes

The dissipation potential Ω for tension-torsion space is defined in Eq. (20) and expanded upon in Eqs. (25) and (26) for the special case of the subject test procedure with constant stress rates during probing. Since $\dot{\sigma}_{11}$ and $\dot{\sigma}_{12}$ were controlled by the test system, essentially all variability in the data is constrained to the measured strain responses. This subject has been covered relatively well in the above discussion of inelastic strain representations.

Remember that during the probing, stress was continuously increased in J_2-value (typically at 10^4 psi/min) until the effective inelastic strain rate of 100 $\mu\epsilon$/min was sensed by the test system. The test's rate sensing method for inelastic response (though quite different from the postprocessing algorithm) proves reasonably accurate in all but a few cases when

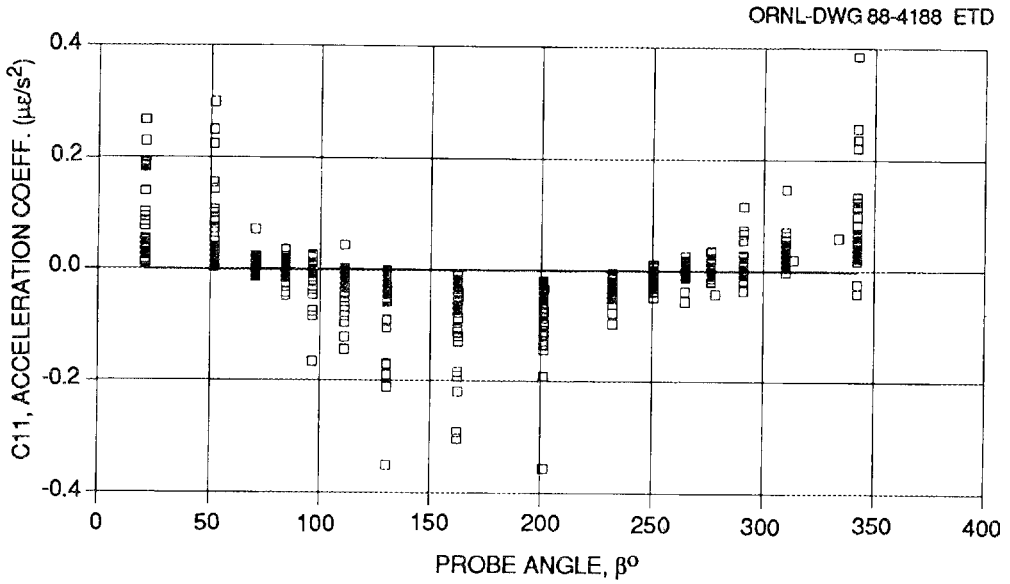

Fig. 27. The "acceleration" coefficient C_{11} vs probe angle for all 606 probes.

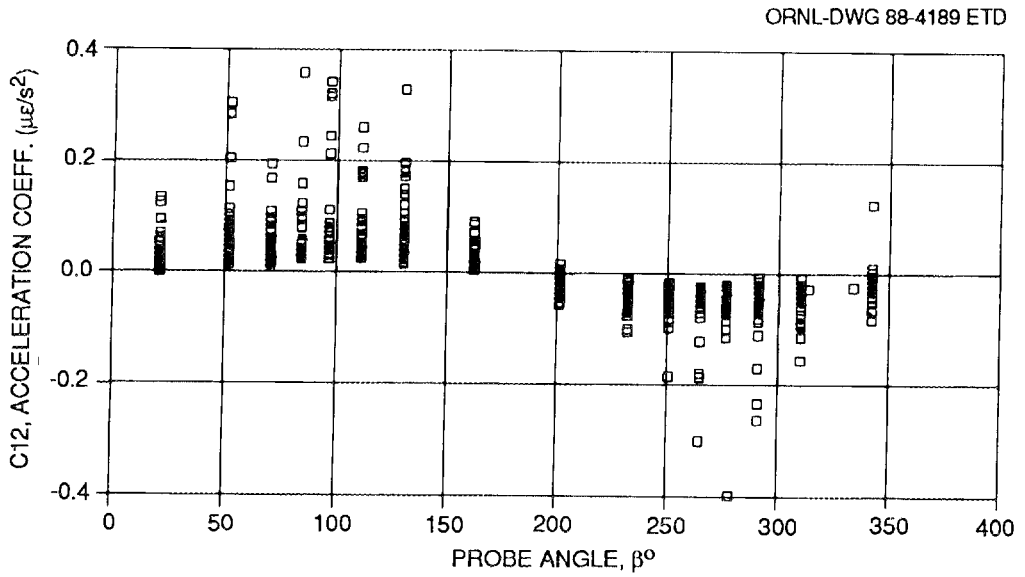

Fig. 28. The "acceleration" coefficient C_{12} vs probe angle for all 606 probes.

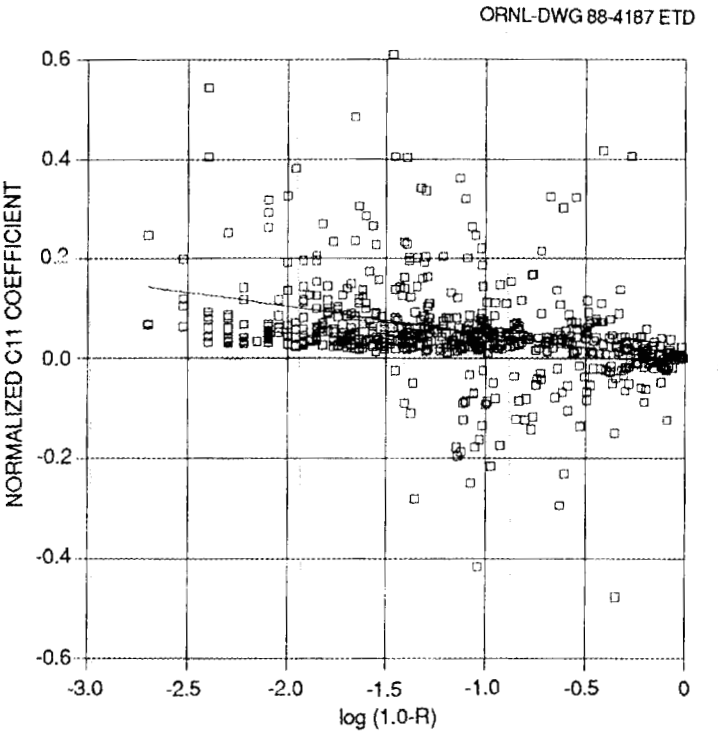

Fig. 29. Normalized C_{11} vs log of (1-correlation coefficient) for all 606 probes.

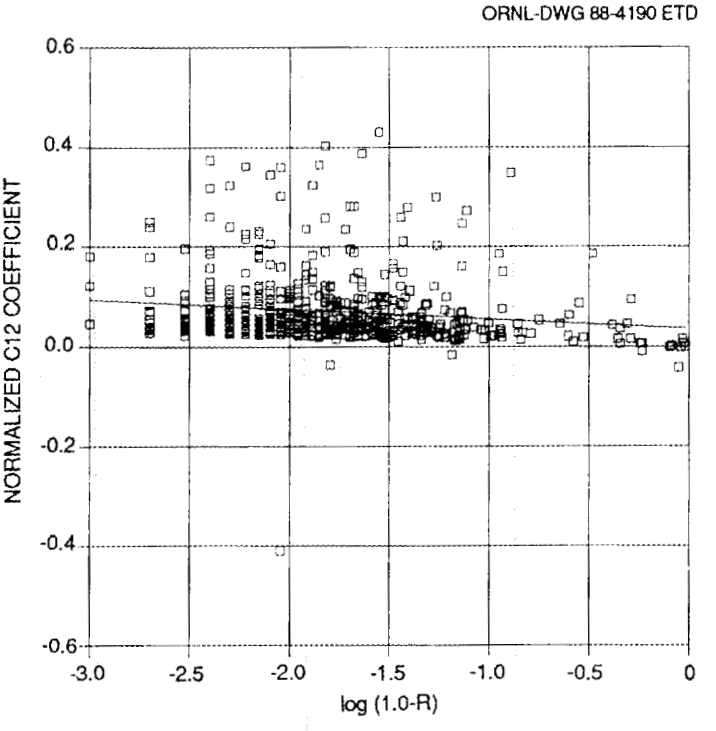

Fig. 30. Normalized C_{12} vs log of (1-correlation coefficient) for all 606 probes.

judged against the postprocessing re-evaluations of the measured SCISR data. Since we are concentrating our present study on SCDP flow surfaces, it is important to discuss the Ω responses for the probes, where every probe produces a different value of Ω and the variation in Ω is considerable.

Ω_{max} is plotted vs β probe angle and against probe sequence in Figs. 31 and 32, respectively. Again, Ω_{max} is defined as the Ω corresponding to the strain rate of 100 $\mu\epsilon$/min. The Ω_{max} values have a mean of 2.62 psi/min and a standard deviation of 1.48 psi/min. Ω_{max} displays considerable scatter across all probes, regardless of angle or sequence. However, there is a systematic variation of the axial and shear contributions to Ω_{max}, where using Eq. (25) we write the axial contribution

$$\Omega^{11}_{max} = \frac{1}{2}\,\dot{\sigma}_{11}\,C_{11}\,t^2_{max}\ , \tag{28}$$

and the shear contribution

$$\Omega^{12}_{max} = \dot{\sigma}_{12}\,C_{12}\,t^2_{max}\ . \tag{29}$$

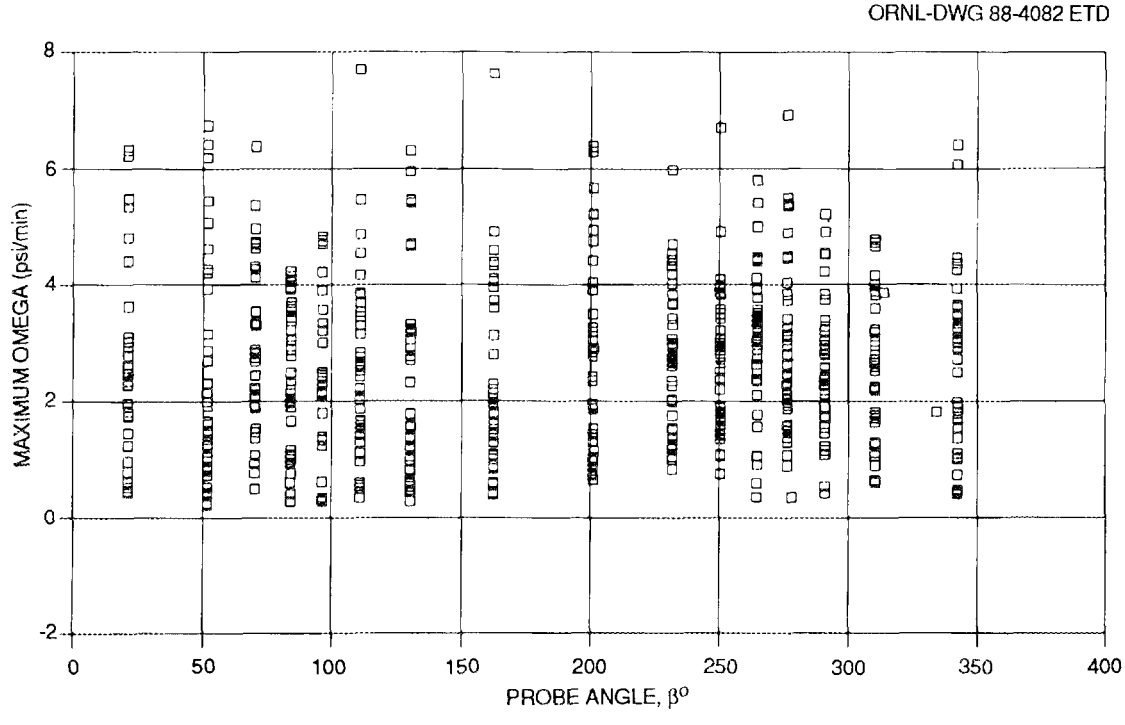

Fig. 31. Maximum omegas reached for the probes vs the angle.

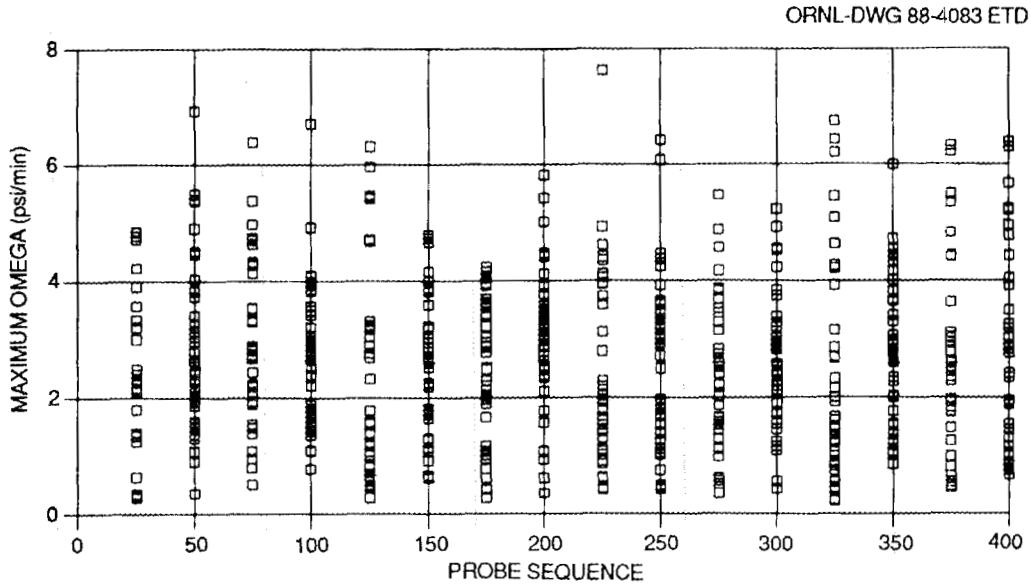

Fig. 32. Maximum omegas reached for the probes vs the test sequence.

Figures 33 and 34 show the axial and shear contributions to Ω_{max} respectively vs the probe angle β. The mean and standard deviation for the axial part are 0.804 psi/min and 1.16 psi/min. The mean and standard deviation for the shear part are 1.815 psi/min and 1.44 psi/min. As in all other discussions concerning variation with β, axial contribution is small near 90° and 270° and shear contribution is small near 0° and 180°. Scatter in both contributions to Ω_{max} is large especially where the component strain response is not small. It is interesting to note that the shear and axial contributions sometimes take on small negative values in Figs. 33 and 34 and that these occurrences are for the same probes showing negative normalized accelerations in Figs. 29 and 30. This is possible in the data reduction process only when the sign of the $\dot{\sigma}$ component disagrees with the sign of the $\dot{\epsilon}$ component. Whereas this condition could be the consequence of material anisotropy, it occurs herein as a consequence of data scatter. The degree to which negative Ω contribution persists in data reduction is another indication of strain-measurement system deficiencies. Certainly Figs. 33 and 34 show that the negative-valued axial Ω_{max} occurrences outnumber the negative-valued shear Ω_{max} occurrences by a large margin. Again, there is a suggestion that shear inelastic response is better-measured than axial inelastic response.

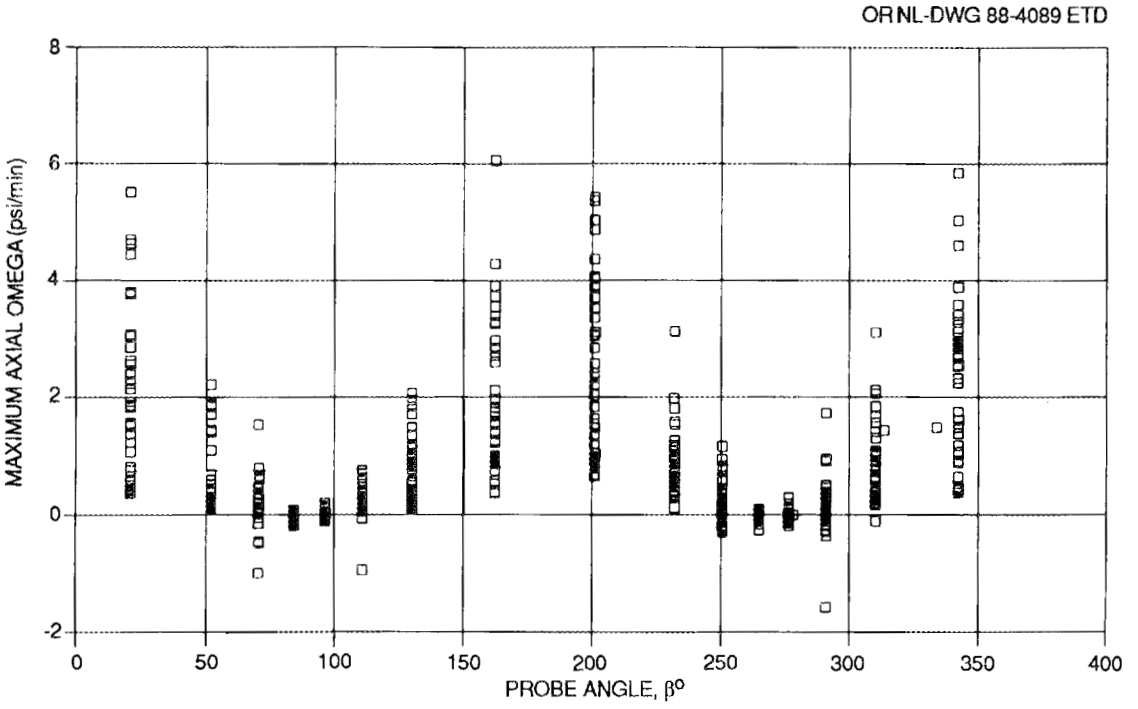

Fig. 33. Maximum omegas (axial portions) for the probes vs the angle.

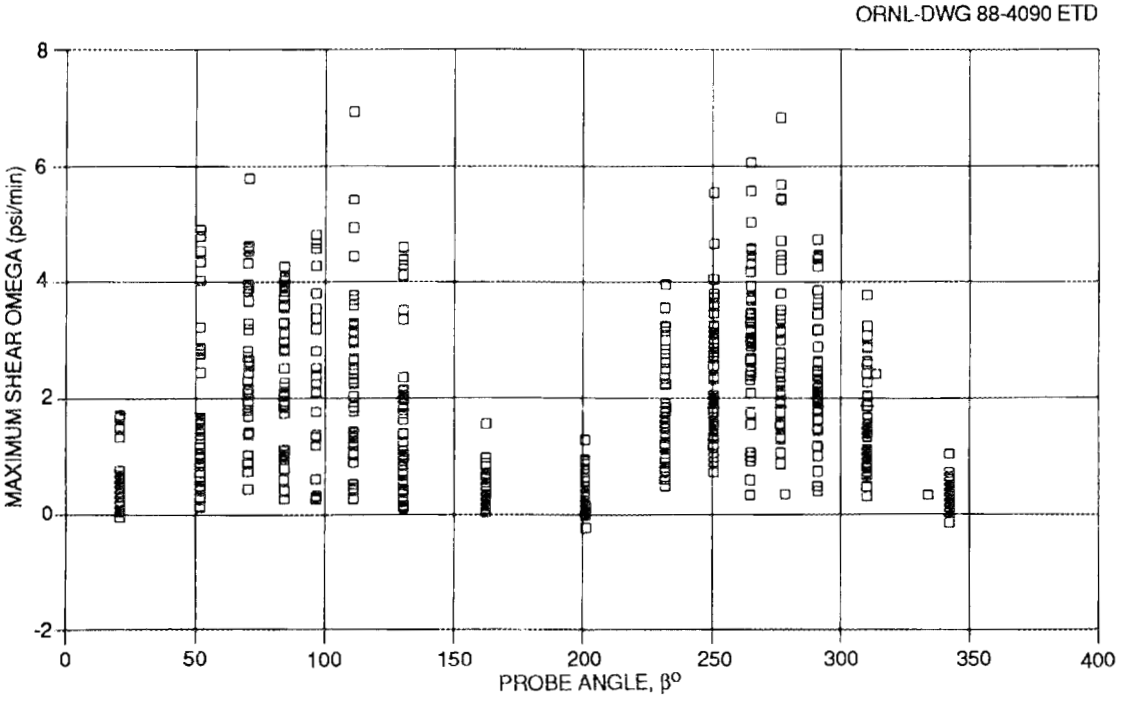

Fig. 34. Maximum omegas (shear portions) for the probes vs the angle.

3.4 Reconstruction of SCISR Ellipses

To reconfirm earlier SCISR flow surfaces of Ref. 8, ellipse functions were fitted to the loci of probe points with equal (constant) inelastic strain rate. Each of the 43 datasets was fitted. Three different SCISR ellipses were determined for each dataset for three values of strain rate, 0, 50, and 100 $\mu\epsilon$/min. The fitted ellipses have the form

$$\frac{(\sigma_{11} - \sigma_{11}^0)^2}{\overset{*}{\sigma}_{11}^2} + \frac{(\sigma_{12} - \sigma_{12}^0)^2}{\overset{*}{\sigma}_{12}^2} = 1 \ . \tag{30}$$

where $\overset{*}{\sigma}_{11}$ and $\overset{*}{\sigma}_{12}$ are the major/minor axes and σ_{11}^0 and σ_{12}^0 are the ellipse center coordinates. Equation (30) becomes a von Mises ellipse if $\overset{*}{\sigma}_{11}/\sqrt{3}/\overset{*}{\sigma}_{12} = 1$.

Figures 35–37 are summary plots for the 129 (43 × 3) ellipse fits. Figure 35 shows $\overset{*}{\sigma}_{11}$ variability with strain rate, and Fig. 36 is the equivalent plot for $\overset{*}{\sigma}_{12}$. Figure 37 shows variability in the ratio $\overset{*}{\sigma}_{11}/\sqrt{3}/\overset{*}{\sigma}_{12}$ with strain rate. At this point we pay no regard to locations in the preloading histograms (either Fig. 2 or Fig. 3) where the SCISR ellipses were determined. Some discussion is later offered concerning that subject. In all three figures (Figs. 35–37), the values for the dependent variable show a normal distribution for a specific strain rate. The straight lines are least-squares fits to the 129 points. While the R factors for the lines in Figs. 35–37 are very small, it appears valid to say that both $\overset{*}{\sigma}_{11}$ and $\overset{*}{\sigma}_{12}$ systematically increase with increasing strain rate, whereas the ratio in Fig. 37 appears to decrease toward the von Mises value, 1, as the rate increases.

3.5 SCDP Ellipses

This subsection presents summary information for the 129 ellipse fits of SCDP flow surfaces, again using the Eq. (30) form. Since every probe of a flow surface determination reached a different value of Ω, it was necessary to devise an algorithm for selection of representative values of Ω for determination of the SCDP surfaces. The approach was briefly discussed in preceding Sect. 2.8 but will be repeated for clarity. It was decided that

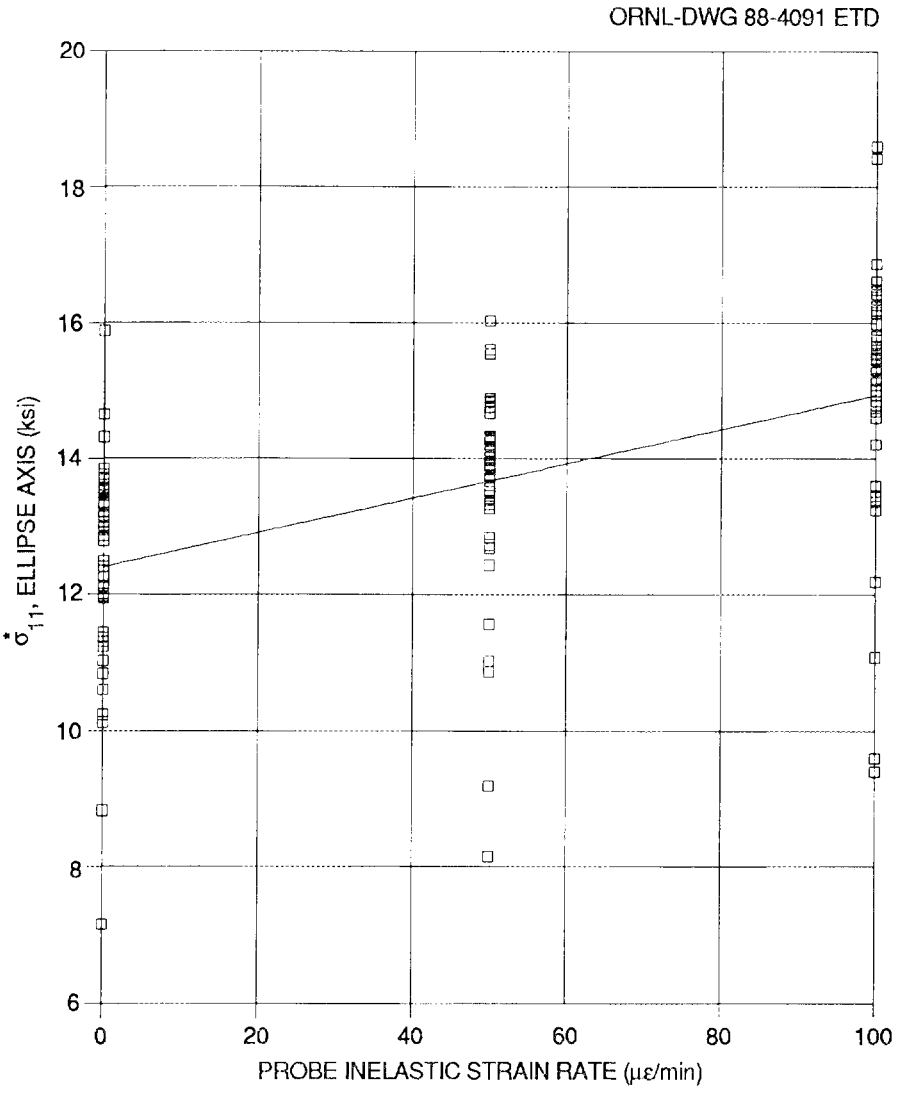

Fig. 35. Axial ellipse axis vs inelastic strain rate for the 129 fitted SCISR surfaces.

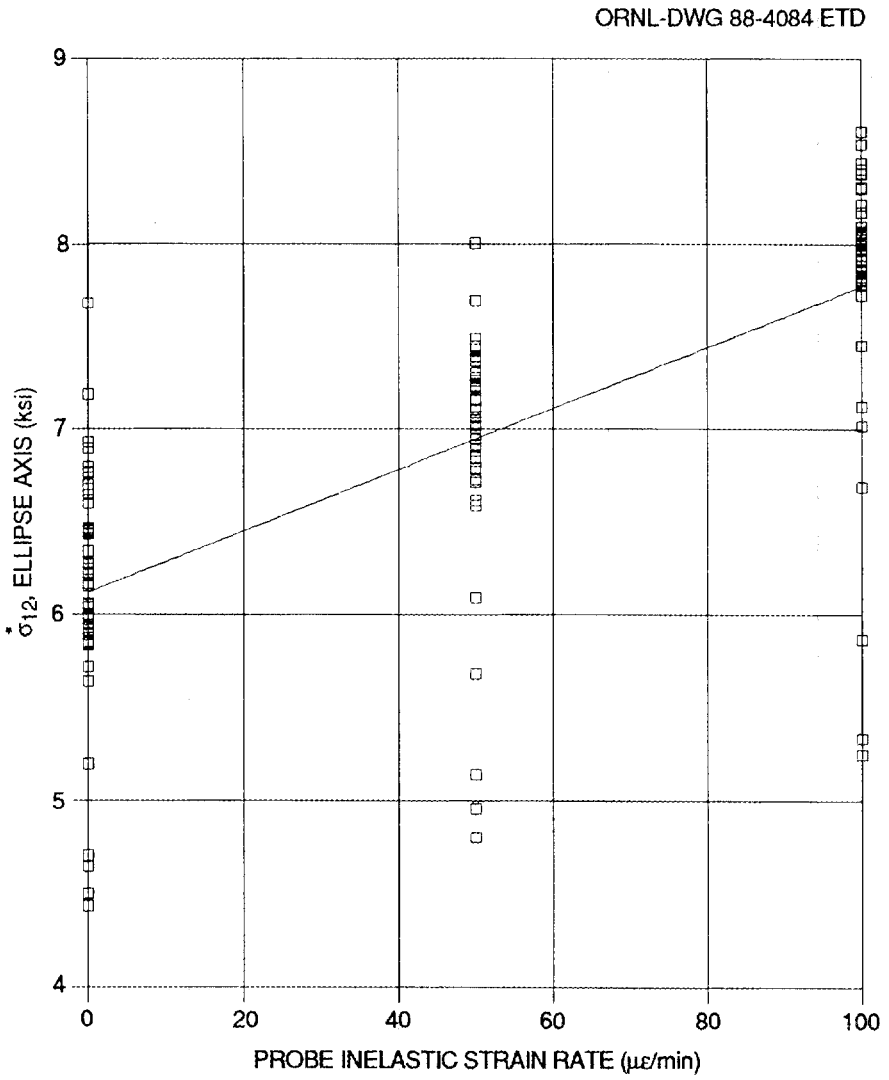

Fig. 36. Shear ellipse axis vs inelastic strain rate for the 129 fitted SCISR surfaces.

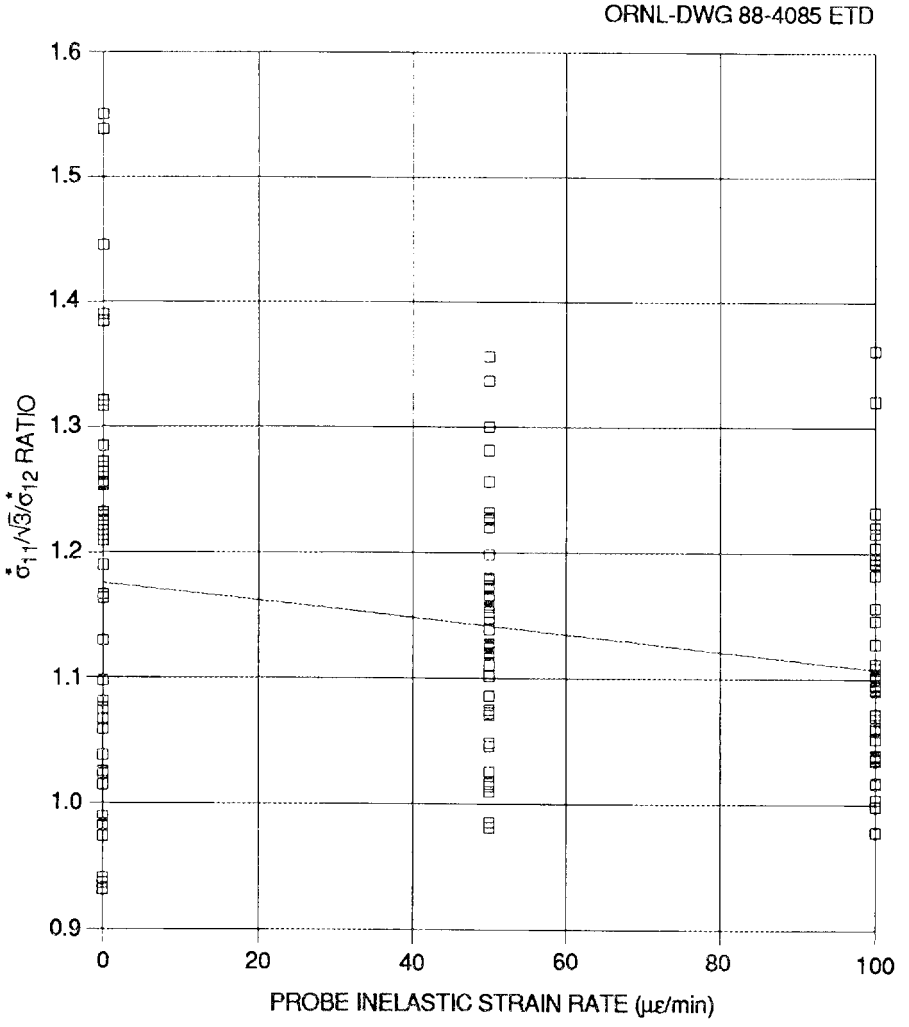

Fig. 37. Ellipse axes ratio vs inelastic strain rate for the 129 fitted SCISR surfaces.

an appropriate largest value of Ω for any set of 16 probes was the average maximum Ω divided by 3. In general, this procedure requires that a few of the probes be extrapolated for any SCDP determination for $\Omega = \bar{\Omega}_{max}/3$. In all 43 cases, a second value, $\Omega = \bar{\Omega}_{max}/6$, was also used requiring very few extrapolations. Lastly the SCDP with value $\Omega = 0$, equivalent to $\bar{\dot{\epsilon}}^P = 0$, was created serving as a check for HOTLIPS data handling operations.

Summary plots for the resulting 129 SCDP ellipses are shown as Figs. 38–40. The relationship of $\overset{*}{\sigma}_{11}$ to Ω is suggested in Fig. 38 while Fig. 39 investigates $\overset{*}{\sigma}_{12}$ vs Ω. As with the case of strain rate shown earlier in Fig. 37, the ratio $\overset{*}{\sigma}_{11}/\sqrt{3}/\overset{*}{\sigma}_{12}$ vs Ω in Fig. 40 shows a slight tendency for the SCDP ellipse to move toward a von Mises ellipse as Ω increases.

The ellipses for SCISR and SCDP are approximations to the more complicated stress function F given in Eq. (13). To examine the shape of F for various values of C, Fig. 41 was constructed. The Fig. 41 high-order surfaces are the axial-torsional solutions to Eq. (13) normalized for the case $\kappa = 1$ and zero internal stress ($a_{ij} = 0$) and solved for various selected values of C.

The ellipse ratio $\overset{*}{\sigma}_{11}/\sqrt{3}/\overset{*}{\sigma}_{12}$ can be used to approximate C since the F family (Fig. 41) resembles ellipses. At least this is a reasonable approximation as long as C is less than say about 5 or so. Two least-squares approximations were carried out to establish a relationship between C and the $\overset{*}{\sigma}_{11}/\sqrt{3}/\overset{*}{\sigma}_{12}$ ratio. When the ratio is 1.2, then C is about 5; when the ratio is 1.1, C = 2.7. Of course, when the ratio is 1.0, then C = 0 producing a von Mises ellipse. The average value of $\overset{*}{\sigma}_{11}/\sqrt{3}/\overset{*}{\sigma}_{12}$ for all 129 SCDP ellipses is 1.14 indicating an average C of about 3.7.

3.6 Study of Normality

Normality for the SCDP surfaces was studied using the 43 ellipse surfaces fitted for $\Omega = \bar{\Omega}_{max}/3$. An off-normal angle η was defined as the angle between the normal vector N_{ij} and the inelastic strain rate vector $\dot{\epsilon}^P_{ij}$. More specifically in the definition for η

$$\vec{N} = \frac{2(\sigma_{11} - \sigma^0_{11})}{\overset{*}{\sigma}^2_{11}}\vec{i} + \frac{2(\sigma_{12} - \sigma^0_{12})}{\overset{*}{\sigma}^2_{12}}\vec{j} \tag{31}$$

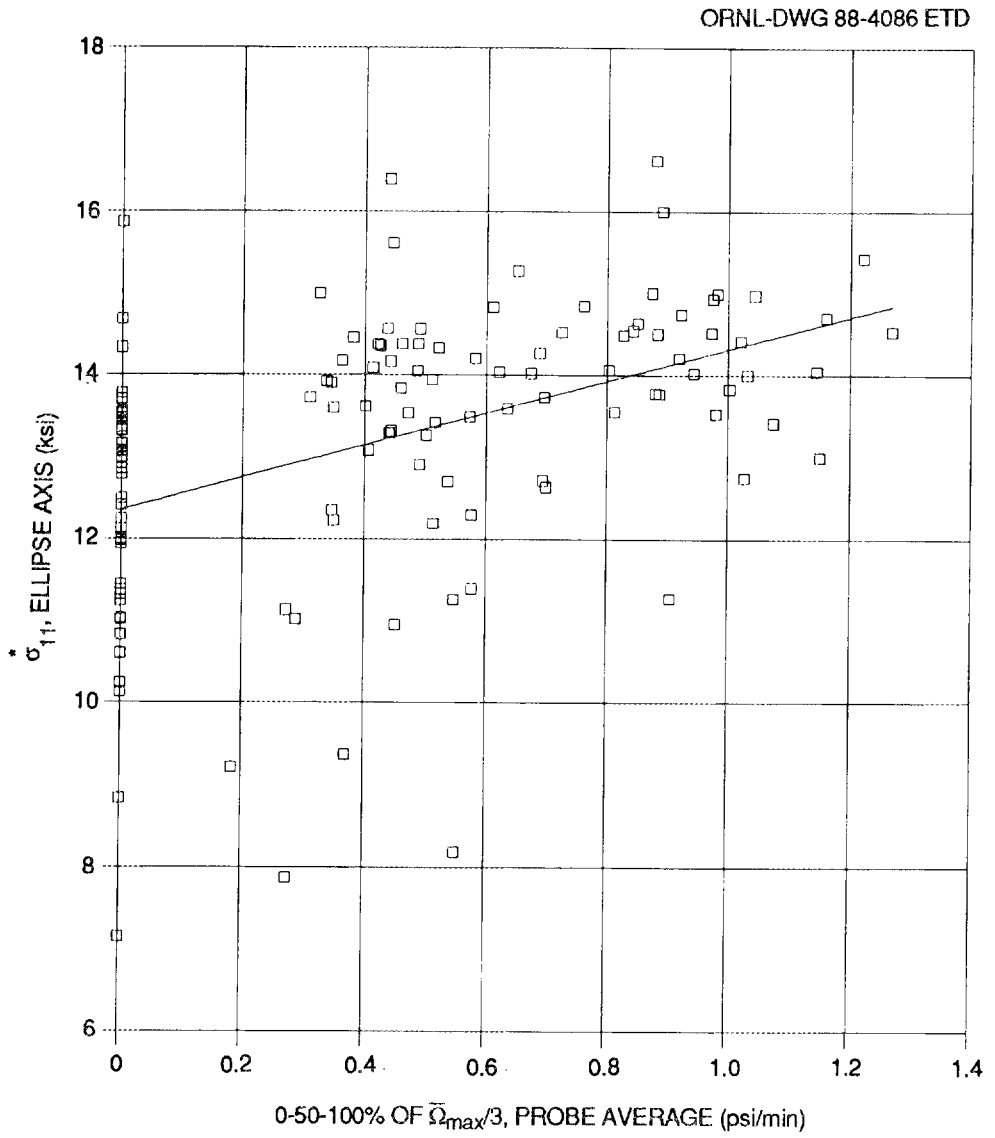

Fig. 38. Axial ellipse axis vs omega value for the 129 fitted SCDP surfaces.

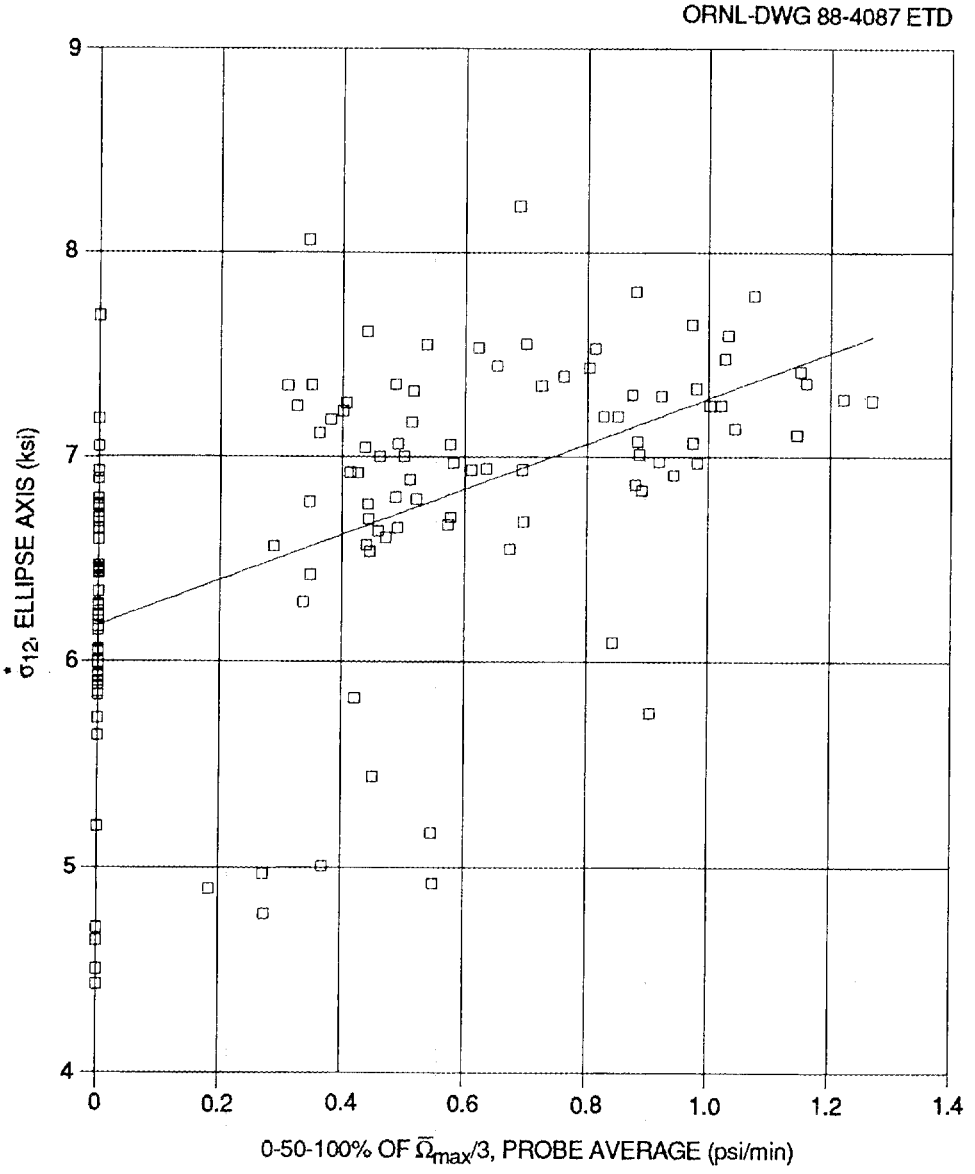

Fig. 39. Shear ellipse axis vs omega value for the 129 fitted SCDP surfaces.

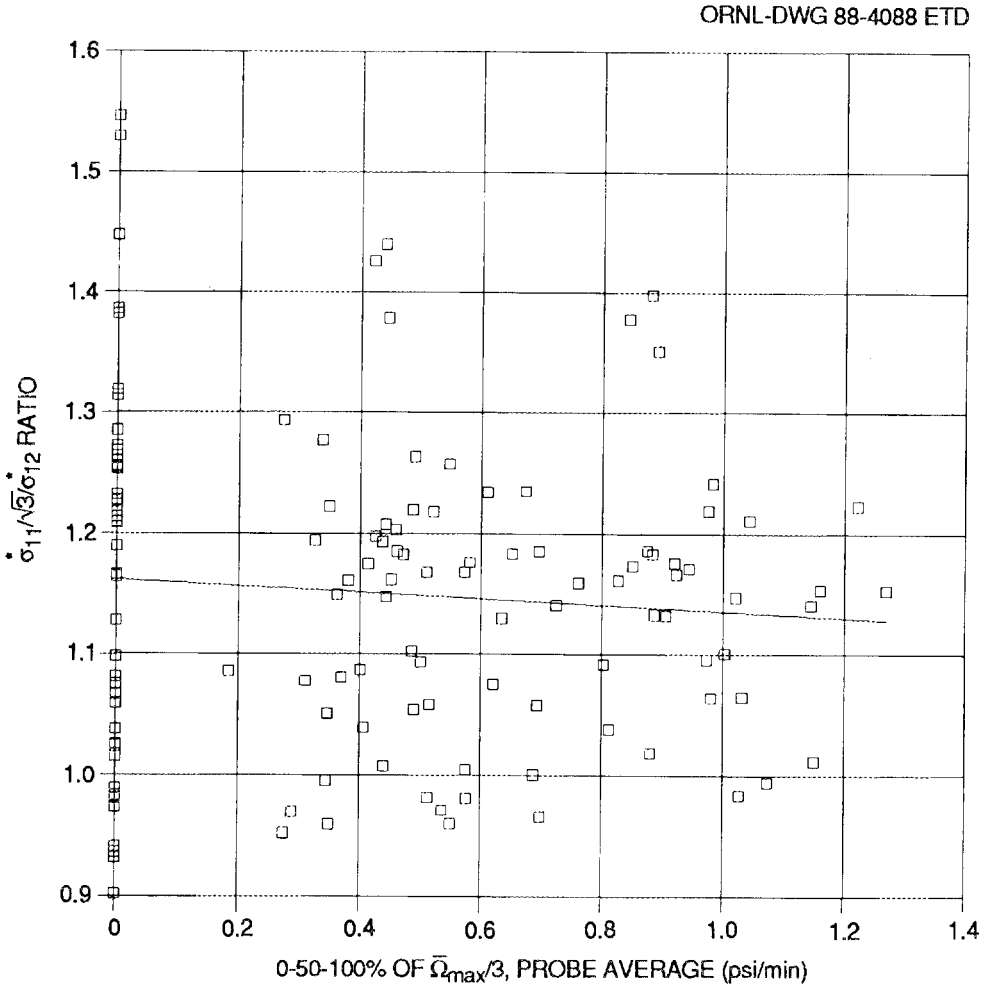

Fig. 40. Ellipse axes ratio vs omega value for the 129 fitted SCDP surfaces.

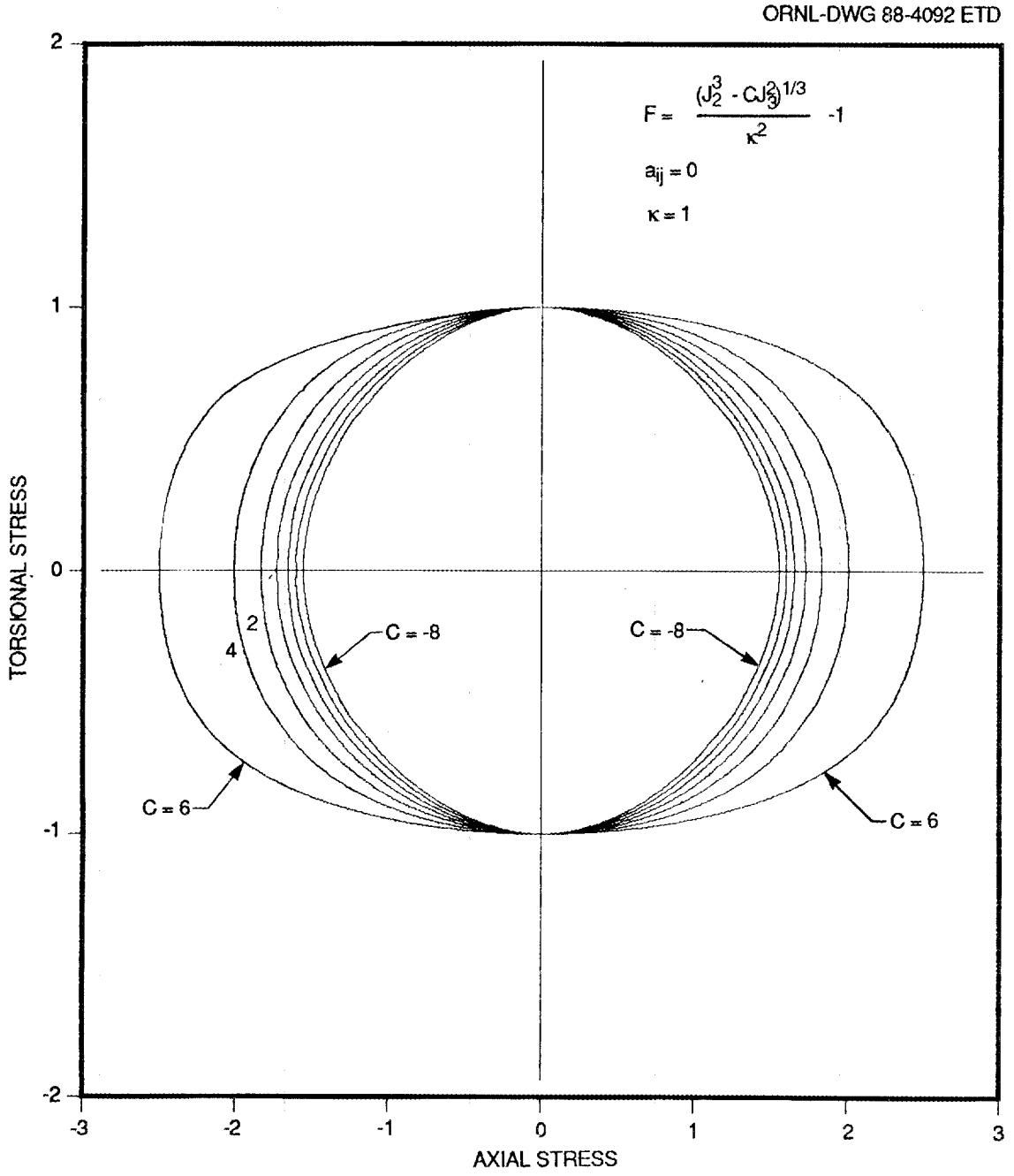

Fig. 41. Normalized $J_2 + J_3$ flow surfaces showing the effect of C value on shape in the axial-torsional stress space. $a_{ij} = 0$ and $\kappa = 1$.

is used where $\vec{i}$ and $\vec{j}$ are unit vectors in the σ_{11} and σ_{12} directions. And $\dot{\vec{\epsilon}}^p$ can be written

$$\dot{\vec{\epsilon}}^p = \dot{\epsilon}^p_{11}\,\vec{i} + 2\dot{\epsilon}^p_{12}\,\vec{j} \quad . \tag{32}$$

Then the off-normal angle is defined as

$$\eta = \cos^{-1}\left[\frac{(\vec{N} \cdot \dot{\vec{\epsilon}}^p)}{\left|\vec{N}\right| \left|\dot{\vec{\epsilon}}^p\right|}\right] , \tag{33}$$

where the inner (dot) product is standard, and the absolute values are the magnitudes of $\vec{N}$ and $\dot{\vec{\epsilon}}^p$ using Eqs. (31) and (32) component definitions. A positive value for η implies a counterclockwise angle from $\vec{N}$ to $\dot{\vec{\epsilon}}^p$.

The normality results are presented in Figs. 42–44 where η and η-statistics are plotted against the probe angle, β. Figure 42 shows all 606 probes for the 43 SCDP high-temperature surfaces. While there is scatter, in general the off-normal angles vary around $\eta = 0°$; or, there is an indication of normality to the fitted SCDP ellipses. To allow better understanding of the Fig. 42 information, the ~40 probes for each of the 16 β

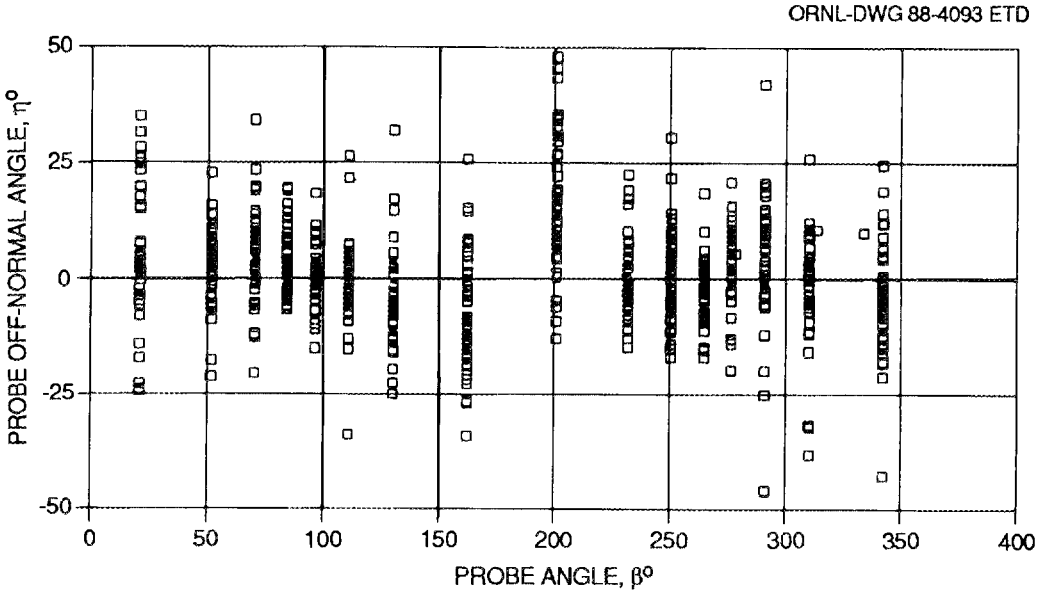

Fig. 42. Off-normal angle vs probe angle for 606 probes.

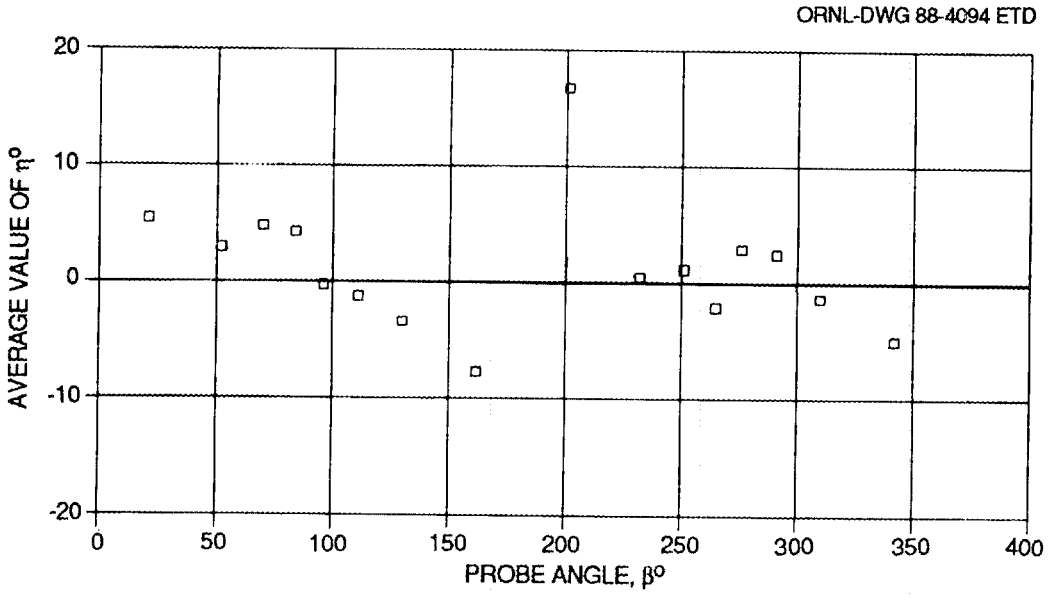

Fig. 43. Average off-normal angle vs the 16 probe angles.

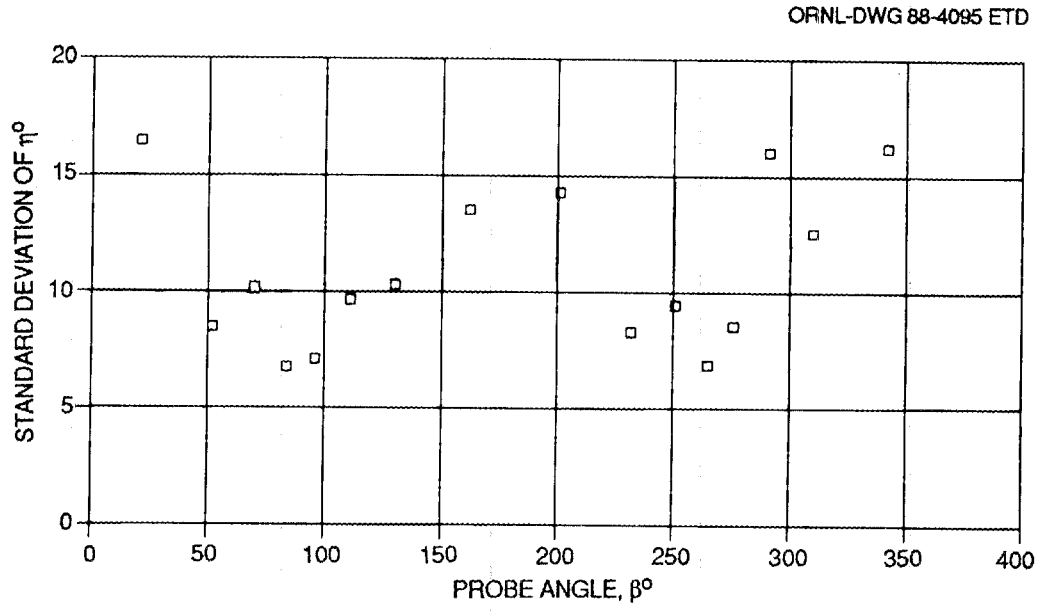

Fig. 44. Standard deviation of off-normal angle vs the 16 probe angles.

angles were averaged and the standard deviations determined. The average values of η are shown in Fig. 43. The average off-normal is always $<\pm 10°$ except for $\beta = 201°$, the 16th probe of the test sequence. One can see dependence of η on $\cos\beta$ with zero values at $\beta = 90°$ and 270°, maximum values at $\beta = 0°$ and 360°, and minimum value at $\beta = 180°$. It is believed that the occurrence of the largest η values near 180° (pure axial compression) is directly related to a problem of the load frame and/or specimen alignment within the frame.

The standard deviations are shown in Fig. 44. The average of all standard deviations is about 11°, and there is an obvious dependence of the standard deviation on $\cos 2\beta$. Maximum scatter at the axial-dominated probes is consistent with previous observations, as is minimum scatter at the torsion-dominated probes.

3.7 SCISR and SCDP Surfaces vs the Test Histogram

The results for the 34 surfaces determined during the Fig. 3 long-term creep test were further studied to establish relationships among the test sequence and the flow surface parameters. A more detailed test histogram is presented as Fig. 45. Points 1–7 constitute the first creep period of length 1002 hours where the stress was held constant (except for interruptions for surface determinations) at a shear stress value of 40 MPa (5.8 ksi). Points 7–12 are the recovery period, and points 12–17 are the second creep period. The zero-stress recovery period lasted 984 hrs. The second creep period had two parts: a 106-h period at 40 MPa shear stress followed by a 316-h period at 60 MPa (8.7 ksi) for a total period of 467 h. Surface determinations were carried out twice at each of the 17 histogram points providing the 34 data sets used.

The behavior for the 50 $\mu\epsilon$/min SCISR ellipses as well as for the 1.0 psi/min and the 2.5 psi/min SCDP ellipses were studied. In a qualitative sense, each of the three ellipse-types behaved very much the same across the Fig. 45 test period. The results are discussed below in terms of the parameter of Eq. (30), $\overset{*}{\sigma}_{11}$ and $\overset{*}{\sigma}_{12}$ ellipse axes and σ^{o}_{11} and σ^{o}_{12} ellipse centers. The figures are from the study of the $\Omega = 2.5$ psi/min SCDP ellipses. Scales are such that slopes (stress rates) appear the same across the figures.

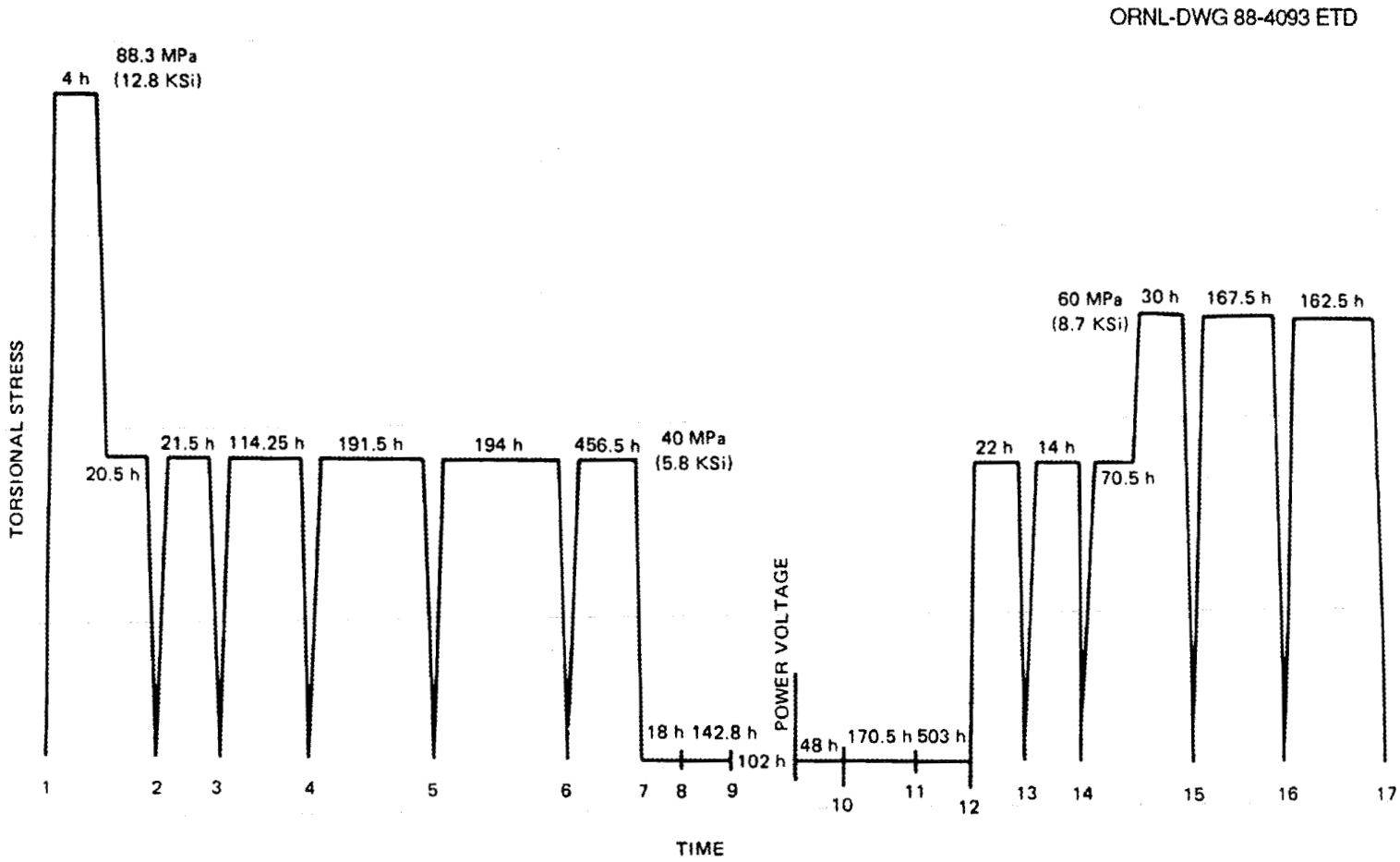

Fig. 45. Expanded form of the test histogram for the long-term creep test. Flow surfaces were determined at each of the 17 points indicated.

First creep period (see Fig. 46)

1. $\overset{*}{\sigma}_{11}$ fluctuates around 16 ksi.
2. $\overset{*}{\sigma}_{12}$ fluctuates around 8 ksi.
3. The σ^{0}_{11} center fluctuates around 0 ksi.
4. The σ^{0}_{12} center appears to slightly increase in positive value, but there is a great deal of scatter.

Recovery period (see Fig. 47)

1. $\overset{*}{\sigma}_{11}$ fluctuates around 15 ksi.
2. $\overset{*}{\sigma}_{12}$ fluctuates around 8 ksi.
3. The σ^{0}_{11} center fluctuates around 0 ksi, but seems to move in a negative direction with time.
4. The σ^{0}_{12} center seems to recover toward a zero value, but there is a great deal of scatter.

Second creep period (see Fig. 48)

1. $\overset{*}{\sigma}_{11}$ fluctuates around 15+ ksi.
2. $\overset{*}{\sigma}_{12}$ fluctuates around 8 ksi.
3. The σ^{0}_{11} center fluctuates around 0 ksi.
4. The σ^{0}_{12} center seems to systematically increase in positive value from 0 ksi toward 2 ksi. Confusion is provided by the last two SCDP surfaces determined at point 17 in the Fig. 45 histogram for which the σ^{0}_{12} center is below 1 ksi.

Thus there is very little that can be substantiated about the behavior of the flow surfaces when one looks at the conglomerate picture provided by Figs. 46–48. The scatter is large. Also, it should be pointed out that the preloadings were modest. It is unfortunate that other more severe preloadings were not used in testing which might have provided measureable behavior. The results for the modest preloadings provide a weak conclusion that the behavior of the SCDP is a kinematic behavior. $\overset{*}{\sigma}_{11}$ and $\overset{*}{\sigma}_{12}$ are constant across the 14-week test. The shear center seems to move and to recover in response to shear loadings and to recovery time. The more pronounced response is to the higher preloading of the second creep period.

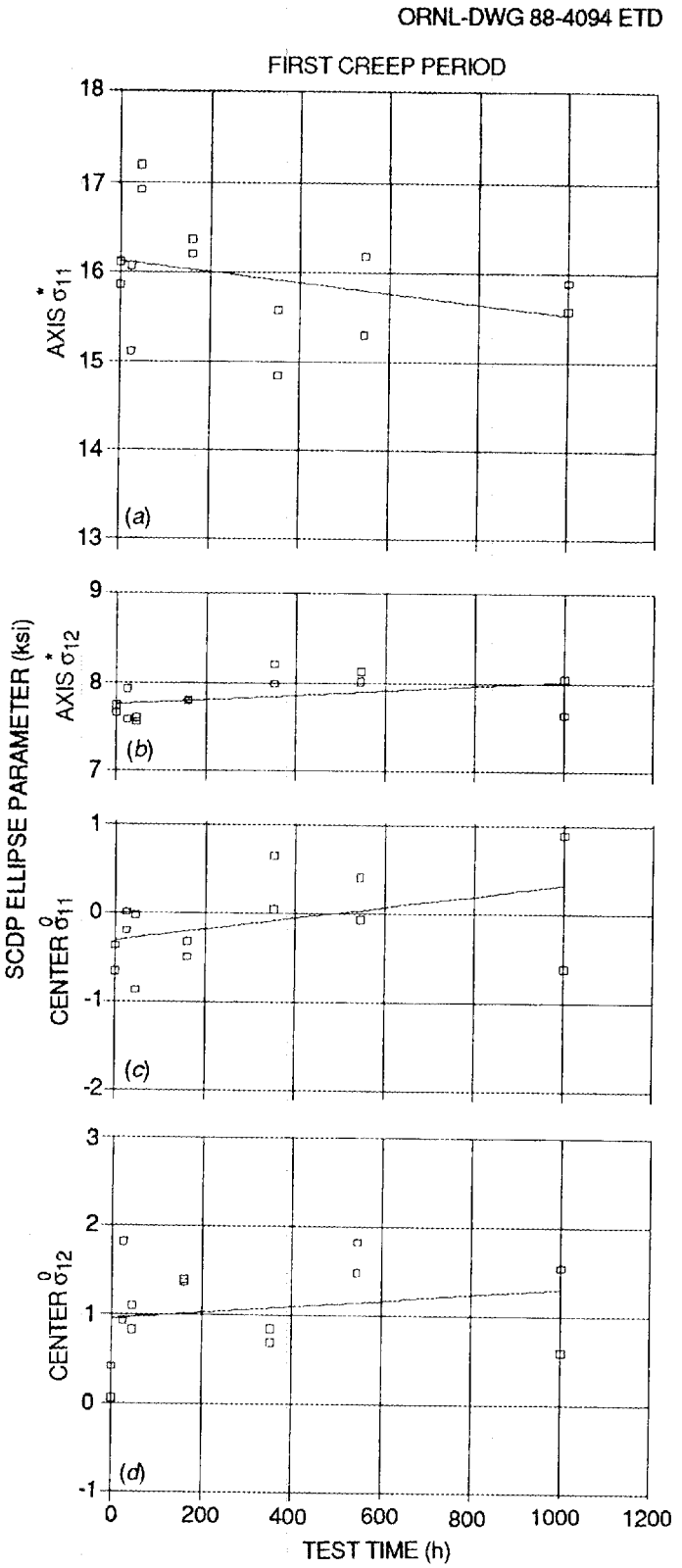

Fig. 46. SCDP ellipse parameters vs time for the first creep period of Fig. 45. $\Omega = 2.5$.

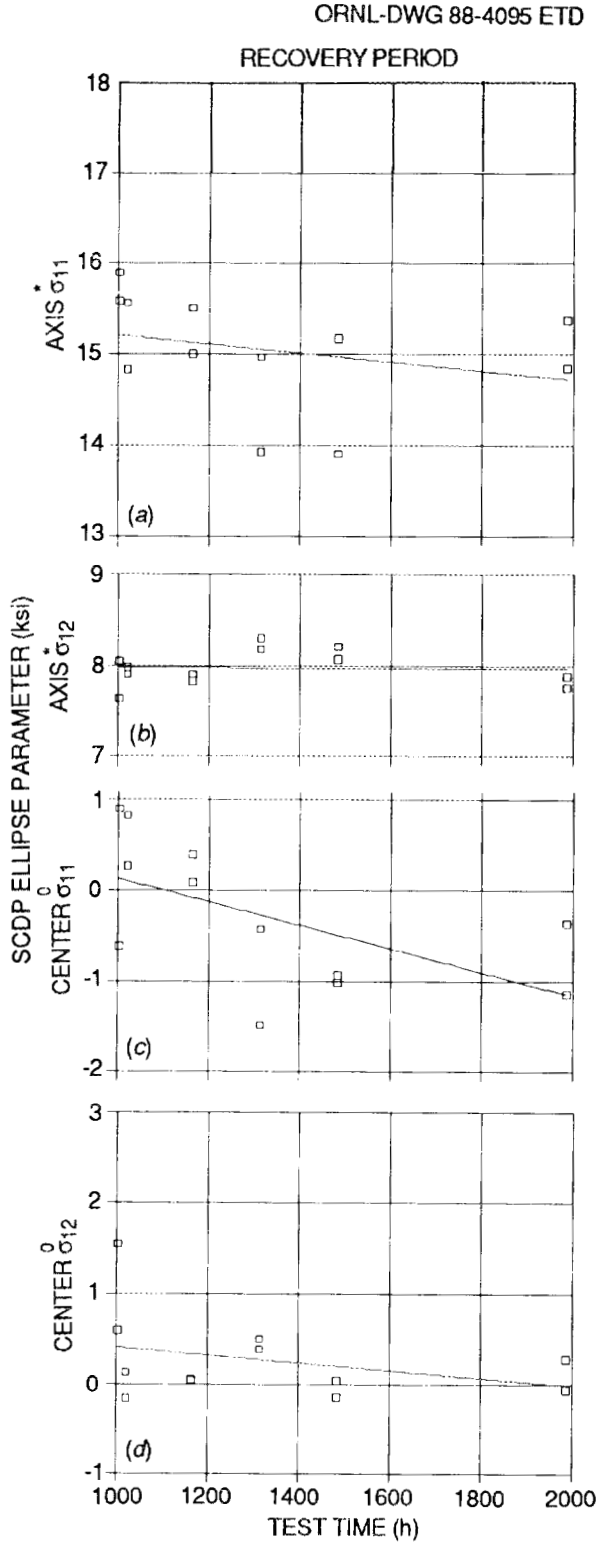

Fig. 47. SCDP ellipse parameters vs time for the recovery period of Fig. 45. $\Omega = 2.5$.

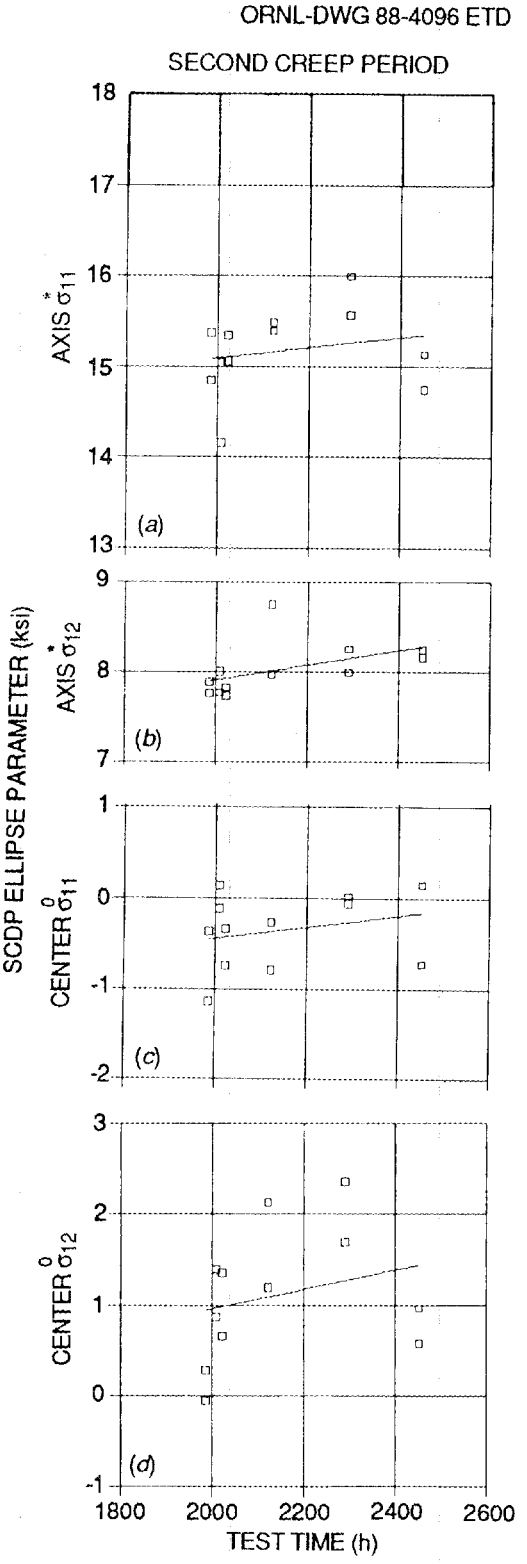

Fig. 48. SCDP ellipse parameters vs time for the second creep period of Fig. 45. $\Omega = 2.5$.

4. CLOSURE

In the study, the data for the multiaxial flow surface tests are reduced and compiled in a systematic fashion. Algorithms for data interpretation were developed and implemented in a computer program called HOTLIPS. Results are discussed in reference to the development of theoretical models for multiaxial flow which rely upon a dissipation potential function to produce specific flow and growth laws of viscoplastic material behavior.

Sources of data scatter are revealed in the systematic approach and are attributed mostly to the strain measurement system for axial strain. A problem with the load frame and/or specimen alignment appears to adversely effect axial compression loadings, mostly. Certainly the "problem" of data scatter is amplified by the requirement of extreme sensitivity for studying small excursions into inelastic response as was the philosophy used in probing to not significantly disturb a "fixed" inelastic state. Also, the preloadings used in the tests were quite modest making it difficult to adequately remove the data scatter from the true material behavior as is required to investigate forms of the flow and growth laws.

Results point to a J_3-dependence of the multiaxial behavior. Preliminary quantification of the C parameter is provided for the candidate form of the dissipation potential surface. Also, it should be noted that C itself is a sensitive parameter which is again difficult to convincingly quantify in the presence of data uncertainty.

The specific choices of data reduction algorithms, though somewhat arbitrary and/or empirical , appear to be adequate. Error studies show that choices of specific form and method result in very good correlations for probes with more pronounced inelastic responses. When the inelastic response is of the same order as the scatter/data-error, then the reduction techniques produce poor correlations. Since the data were provided to NASA as a deliverable of the current effort, independent follow-on studies are possible. A challenging study would be to develop methods to systematically strip data error from the experimental results. Of course, a more scientific approach would be to repeat the experiments with improved loading methods, extensometry, and test-control methods. Also, perhaps the

probes should be conducted to larger Ω values, say Ω = 8–10 psi/min. If this retesting option is exercised, then the results presented herein will be quite valuable in guiding and planning such future testing.

5. ACKNOWLEDGMENTS

The authors wish to acknowledge the contributions of various individuals. R. L. Battiste and S. J. Ball were responsible for developing test procedures and methods and for conducting the original SCISRs tests. The current data analysis study was initially envisioned by J. R. Ellis (previously of ORNL but currently of NASA) who is also partly responsible for funding the study through the NASA-Lewis Research Center.

Ideas on methods to reinvestigate the SCISR data for SCDP surface determinations were formulated with the help of Ball, Battiste, and Ellis and with the additional involvement of J. M. Corum. R. L. Thompson (of NASA) and Corum were responsible for producing the Interagency Agreement between NASA and DOE that allowed funding.

B. L. P. Booker was instrumental in collecting and reformatting the data for ease-of-use in the HOTLIPS computer program. She was also responsible for programming the graphics portions using the DISSPLA commercial software package.

The report manuscript was prepared by L. B. Dockery. R. L. Battiste and W. K. Sartory reviewed the document.

REFERENCES

1. D. N. Robinson, *A Unified Creep-Plasticity Model for Structural Metals at High Temperature*, ORNL/TM-5969, Oak Ridge National Laboratory, 1978.

2. D. C. Drucker, "On the Role of Experiment in the Development of Theory" *Proceedings of the Fourth U.S. National Congress of Applied Mechanics*, ASME, 1962.

3. D. N. Robinson and J. R. Ellis, "A Multiaxial Theory of Viscoplasticity for Isotropic Materials," in *Turbine Engine Hot Section Technology 1986*, NASA Conf. Pub. 2444, October 1986, Cleveland, OH.

4. D. N. Robinson et al., "Constitutive Equations for Describing High-Temperature Inelastic Behavior of Structural Alloys," in *Proceedings of the Specialists Meeting on High-Temperature Structural Design Technology of LMFBRs*, IWGFR/11, IAEA, Champion, PA, April 27–30, 1976.

5. D. N. Robinson and R. W. Swindeman, *Unified Creep-Plasticity Constitutive Equations for 2-1/4 Cr–1 Mo Steel of Elevated Temperature*, October 1982.

6. D. N. Robinson, "Constitutive Relationships for Anisotropic High-Temperature Alloys," *J. Nucl. Eng. and Des.*, Vol. 83, pp. 389–96 (1984).

7. D. N. Robinson and J. R. Ellis, "Experimental Determination of Flow Potential Surfaces Supporting a Multiaxial Formulation of Viscoplasticity," *Proc. 5th International Seminar on Inelastic Analysis and Life Prediction in High Temperature Environments*, Paris, France, 1985.

8. R. L. Battiste and S. J. Ball, "Determination of Surfaces of Constant Inelastic Strain Rate at Elevated Temperature," in *Turbine Engine Hot Section Technology 1986*, NASA Conf. Pub. 2444, October 1986, Cleveland, OH.

APPENDIX

EXPANDED RESULTS

This Appendix presents the fitted ellipses for SCISR values $\bar{\dot{\epsilon}}^p = 0$, 50, and 100 $\mu\epsilon$/min and for SCDP values $\Omega = 0$, 50, and 100% of $\bar{\Omega}_{max}/3$ for the 22 "initial" determinations of flow surfaces. (The 21 repetitions of surface determinations are not included since each is not very different from the corresponding initial determination.) Recall that the first 5 test interruptions were at histogram points of the short-term cyclic preloading shown earlier as Fig. 2. The other 17 test interruptions were at histogram points of the long-term creep preloading shown in Fig. 3.

In all Appendix figures the arrows drawn are for the maximum $\bar{\dot{\epsilon}}^p$ and Ω-valued SCISR/SCDP surfaces. They use ratioed components of $\dot{\epsilon}^p_{ij}$ to allow study of normality to the flow surfaces. Also, in every case the length of the arrow is proportional to $\bar{\dot{\epsilon}}^p$. In the case of the SCISR ellipses the arrows have a length equal to a redetermined $\bar{\dot{\epsilon}}^p_{max}$ which is usually close to 100 $\mu\epsilon$/min determined during the actual testing. Note that for the SCDP ellipses, though the direction of the strain rate arrow is the same as for the SCISR surface drawing, the variation in length is quite substantial, probe-to-probe, with values usually less than, but sometimes much greater than 100 $\mu\epsilon$/min.

Figures A.1–A.5 are the SCISR and SCDP ellipses for points 1–5 of Fig. 2. The figures are labeled corresponding, P1–P5, and legends are provided to show $\bar{\dot{\epsilon}}^p$ and Ω values. Figure A.1 for the virgin specimen has the smallest ellipses. Figures A.2 and A.4 SCDP surfaces particularly show plus and minus shear motion in response to the plus and minus preloadings. The SCDP surfaces in Fig. A.5 show a residual plus shear motion at P5 at the conclusion of the Fig. 2 preloading.

Figures A.6–A.22 are the SCISR and SCDP ellipses for points 1–17 of Fig. 3. The figures are labeled correspondingly, C1–C17, and legends are provided to show $\bar{\dot{\epsilon}}^p$ and Ω values. Considerable discussion of the behavior of such ellipses vs the Fig. 3 test histogram was presented earlier in Chapter 3 and will not be elaborated again. Briefly, the point C1 determination in Fig. A.6 shows that the ellipses are centered around the stress origin but are larger than the virgin surfaces of Fig. A.1. At the end of

the first creep period, point C7 as in Fig. A.12, the SCDP surfaces have shifted in the direction of the plus shear creep strain. Recovery of the surface motion appears in Figs. A.13–A.18 for points C8–C13 of the recovery period. During the more pronounced creeping of the second creep period, surfaces in Figs. A.19–A.22 for points C14–C17 again show shifting in the direction of the accumulated shear creep strain.

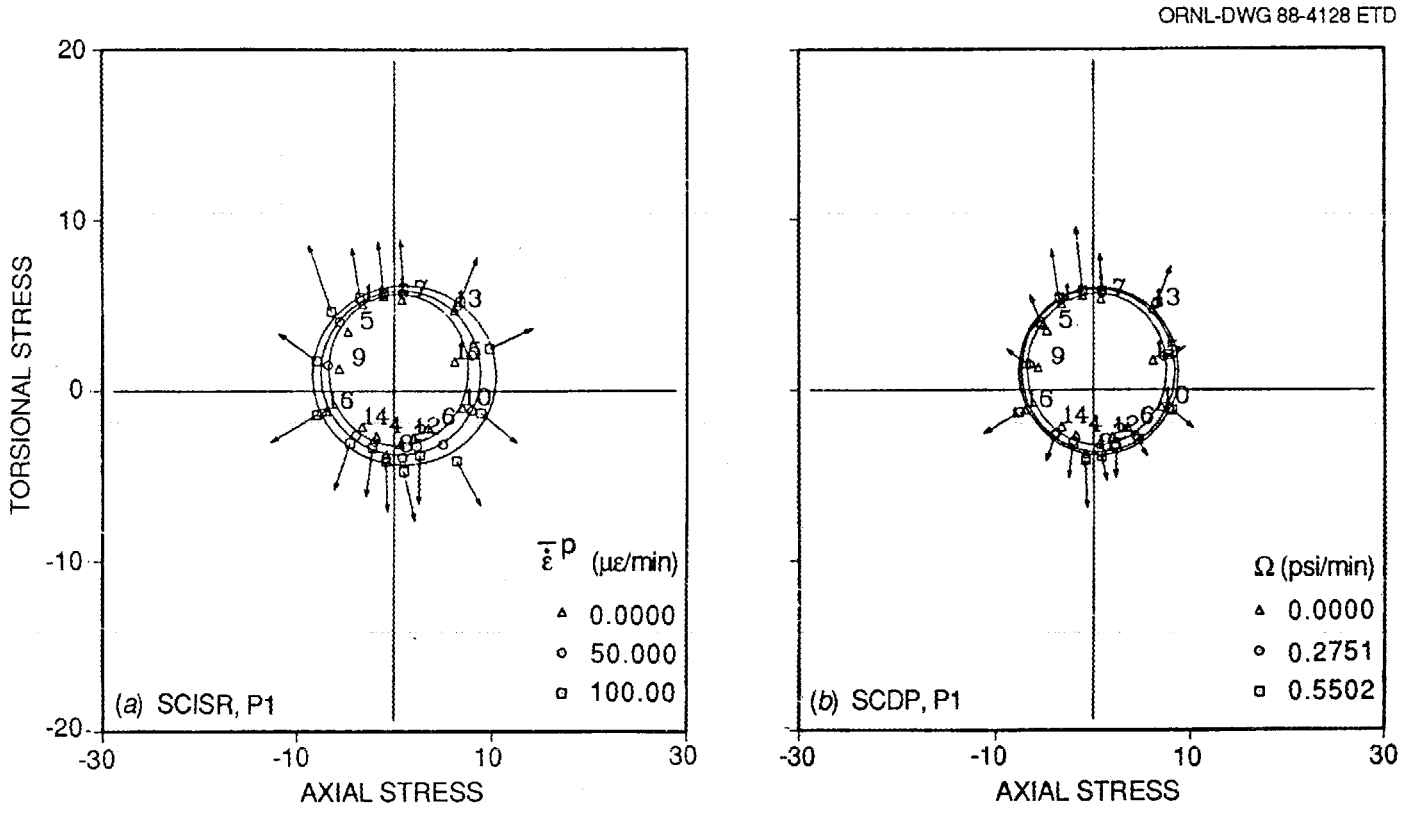

A.1. Flow surfaces for point 1 of Fig. 2 preloading.

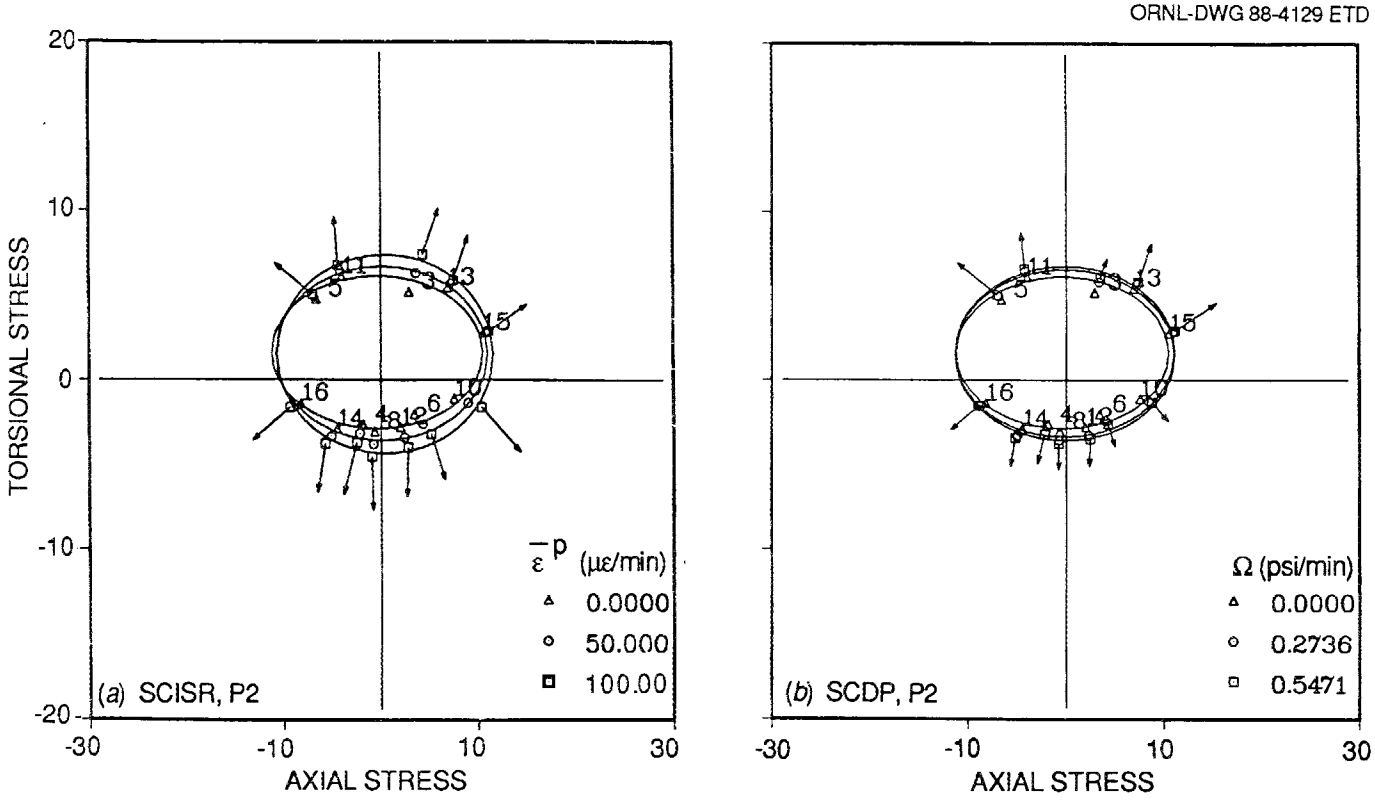

A.2. Flow surfaces for point 2 of Fig. 2 preloading.

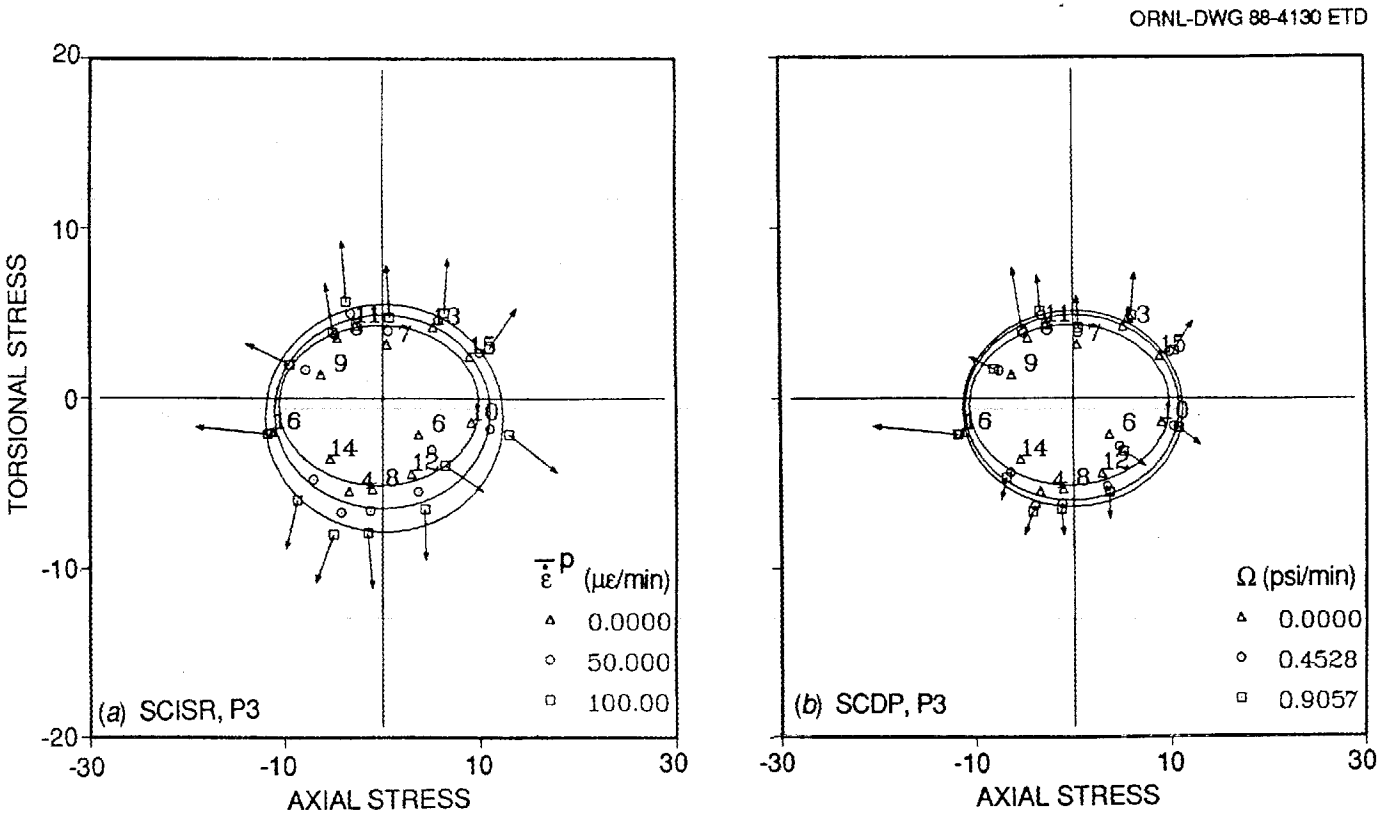

A.3. Flow surfaces for point 3 of Fig. 2 preloading.

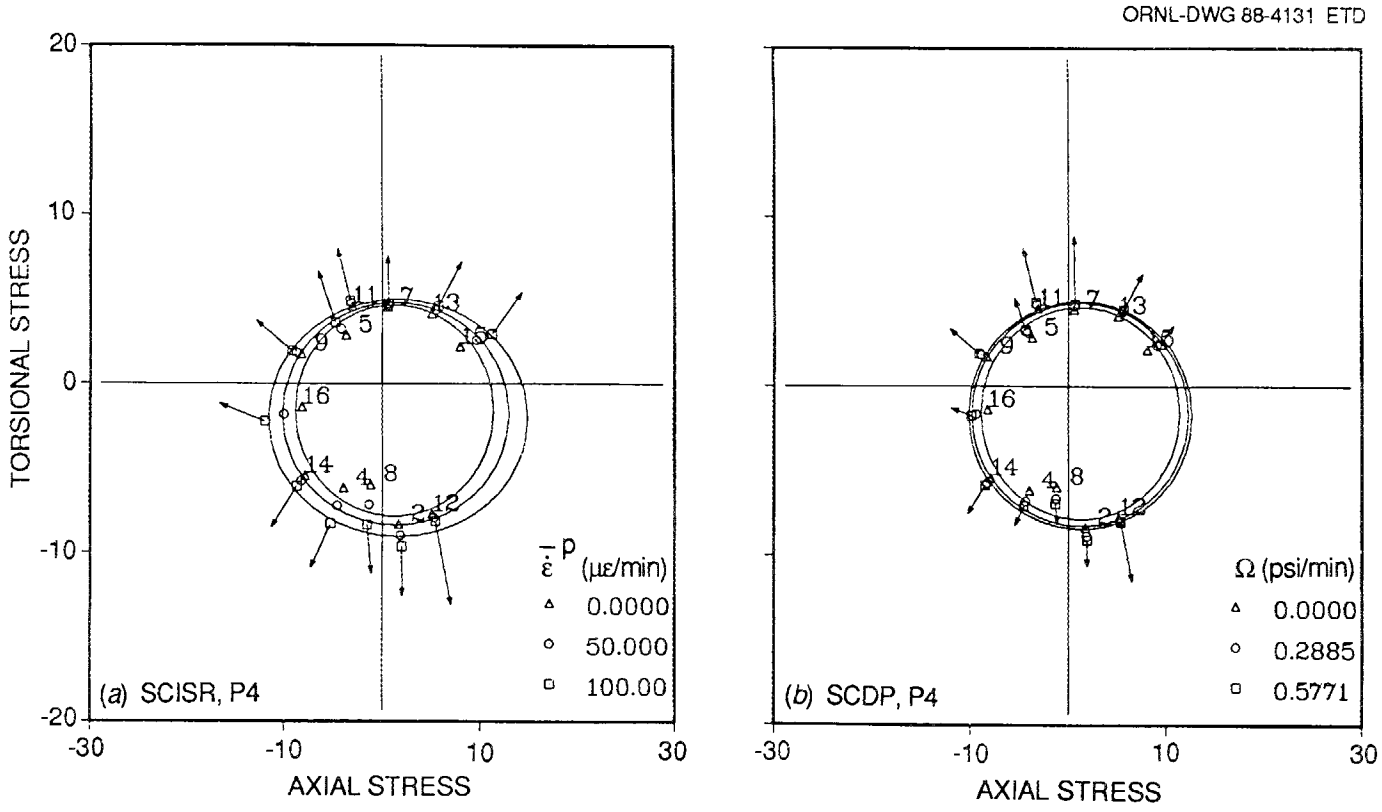

A.4. Flow surfaces for point 4 of Fig. 2 preloading.

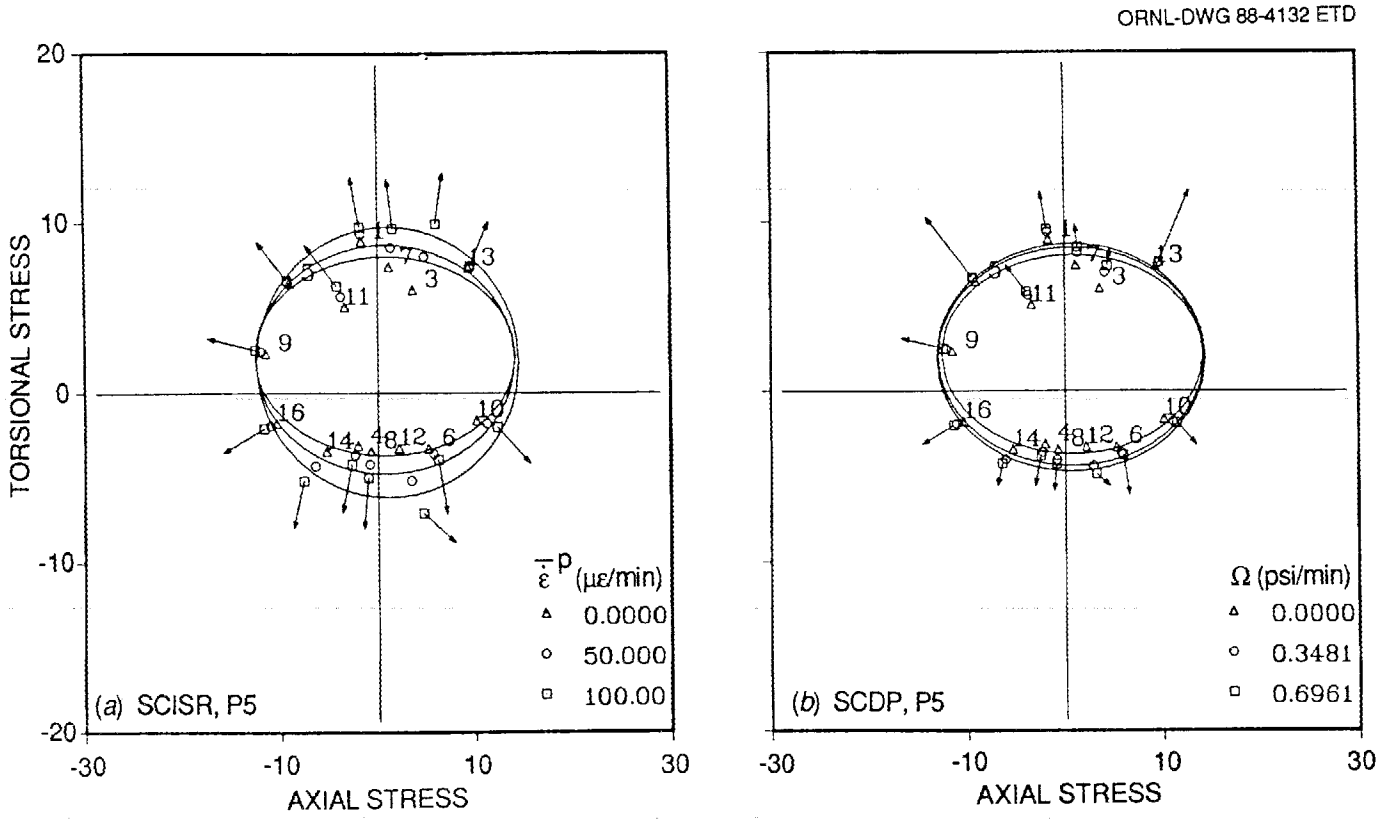

A.5. Flow surfaces for point 5 of Fig. 2 preloading.

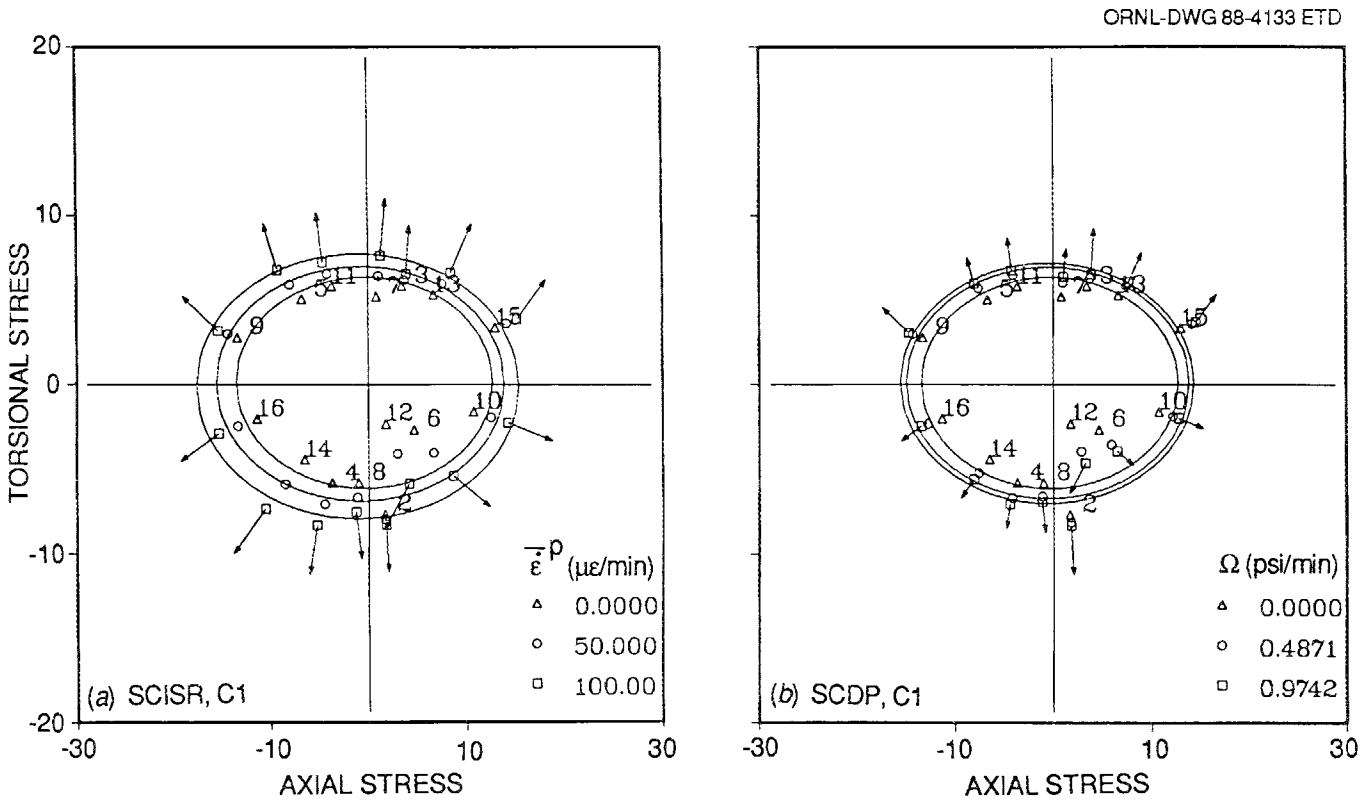

A.6. Flow surfaces for point 1 of Fig. 3 preloading.

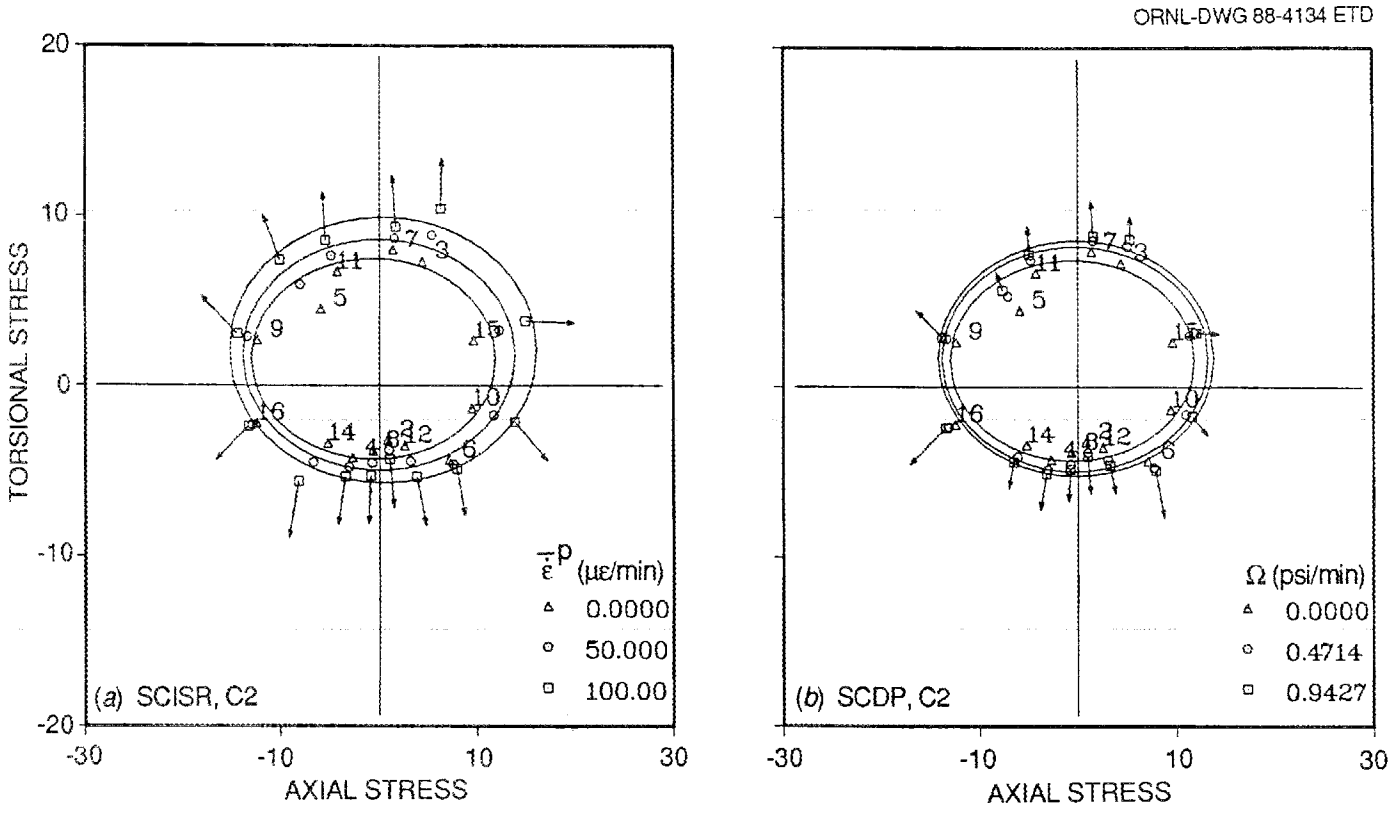

A.7. Flow surfaces for point 2 of Fig. 3 preloading.

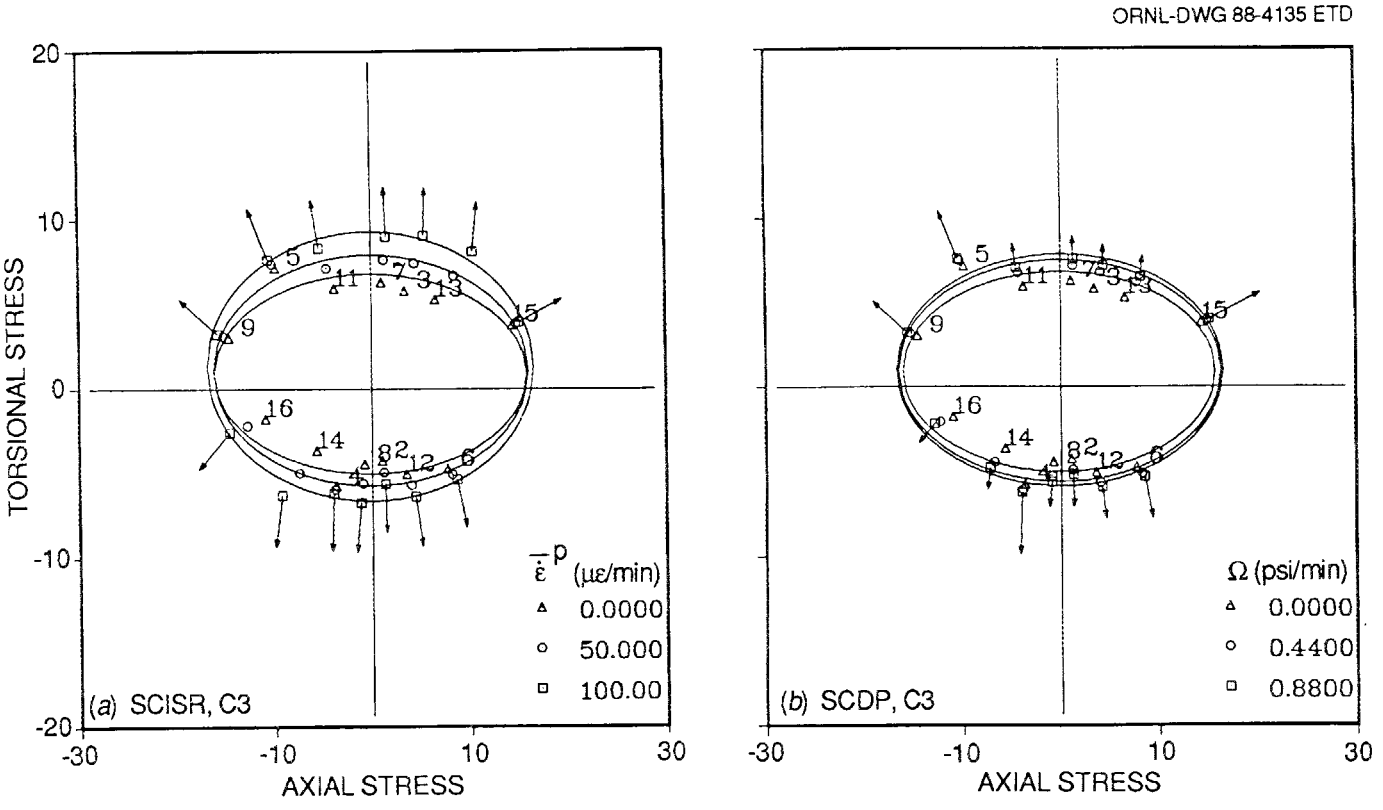

A.8. Flow surfaces for point 3 of Fig. 3 preloading.

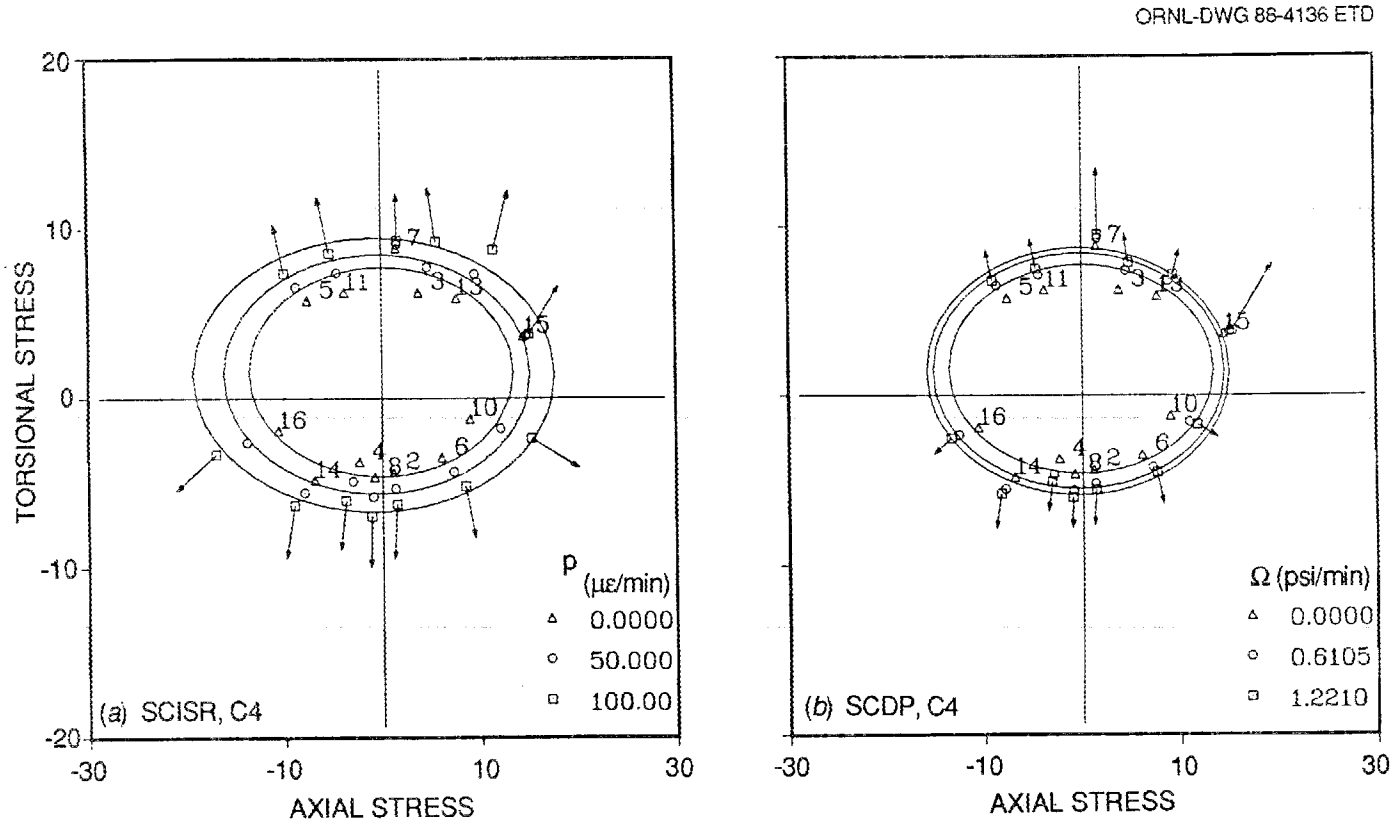

A.9. Flow surfaces for point 4 of Fig. 3 preloading.

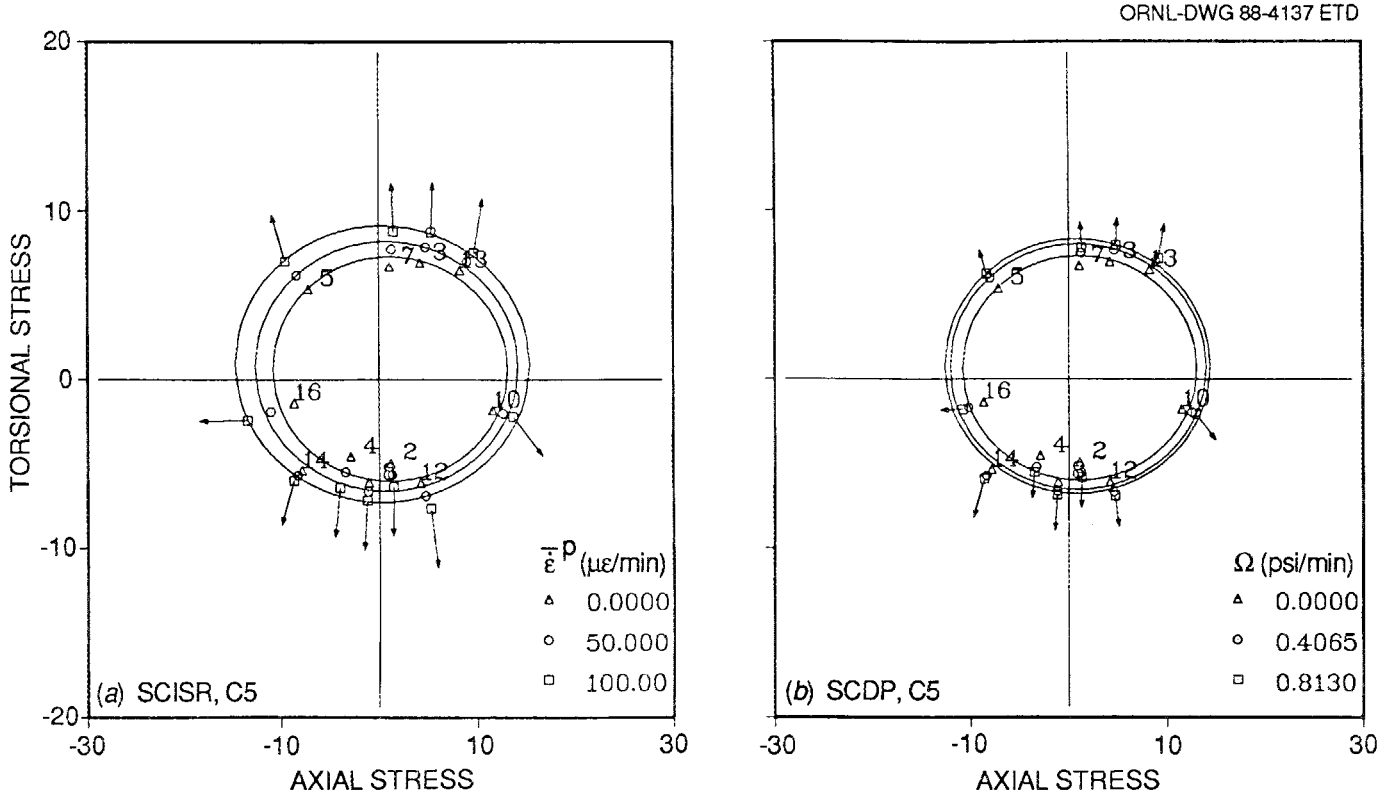

A.10. Flow surfaces for point 5 of Fig. 3 preloading.

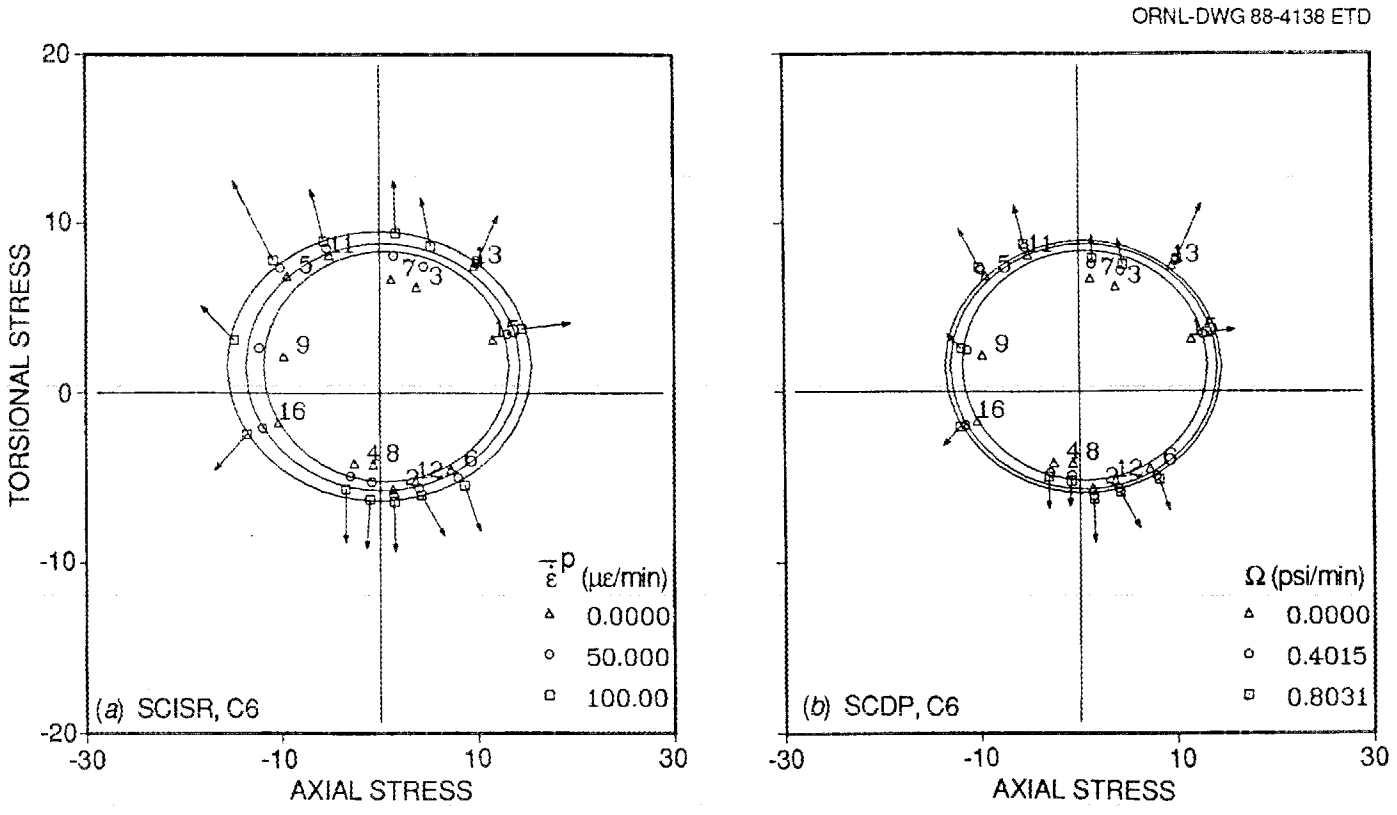

A.11. Flow surfaces for point 6 of Fig. 3 preloading.

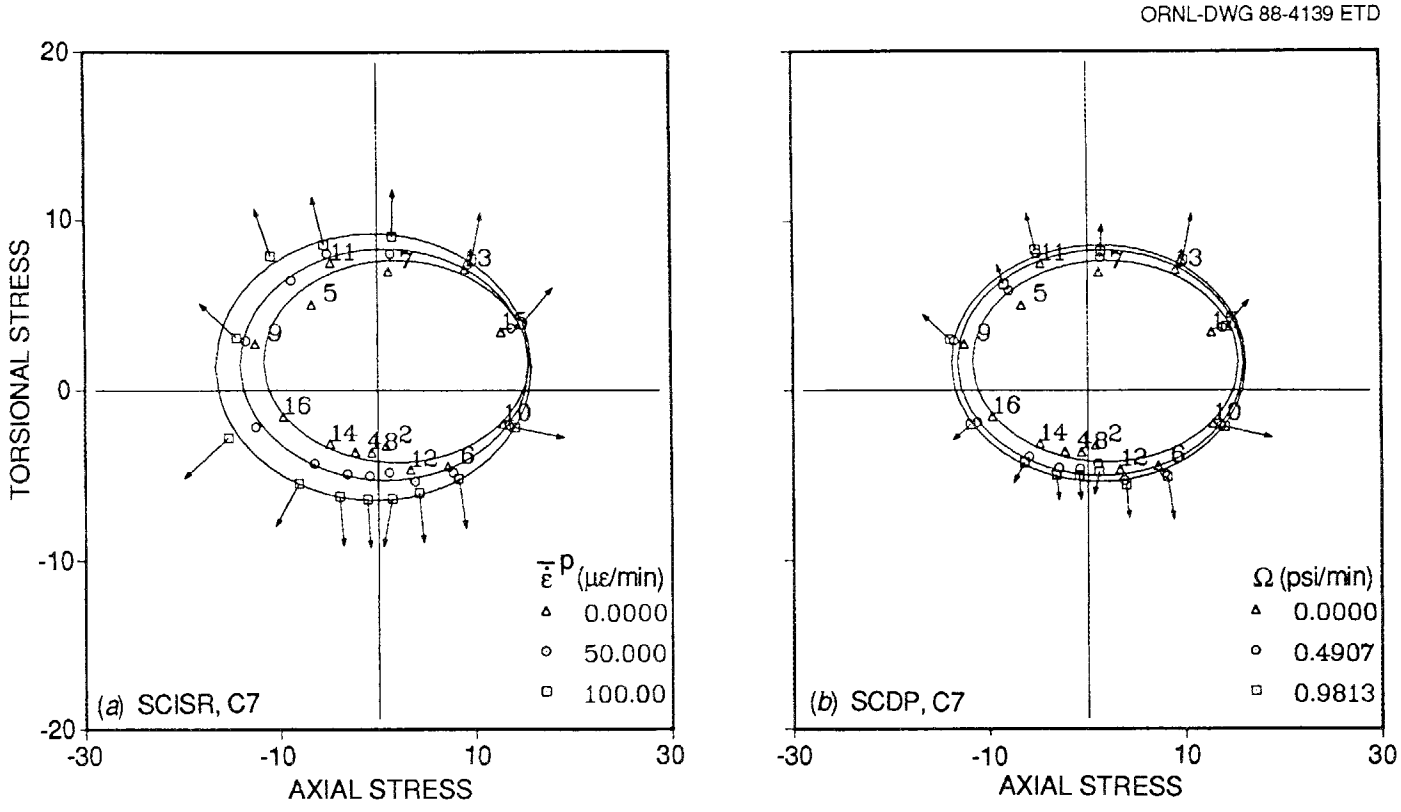

A.12. Flow surfaces for point 7 of Fig. 3 preloading.

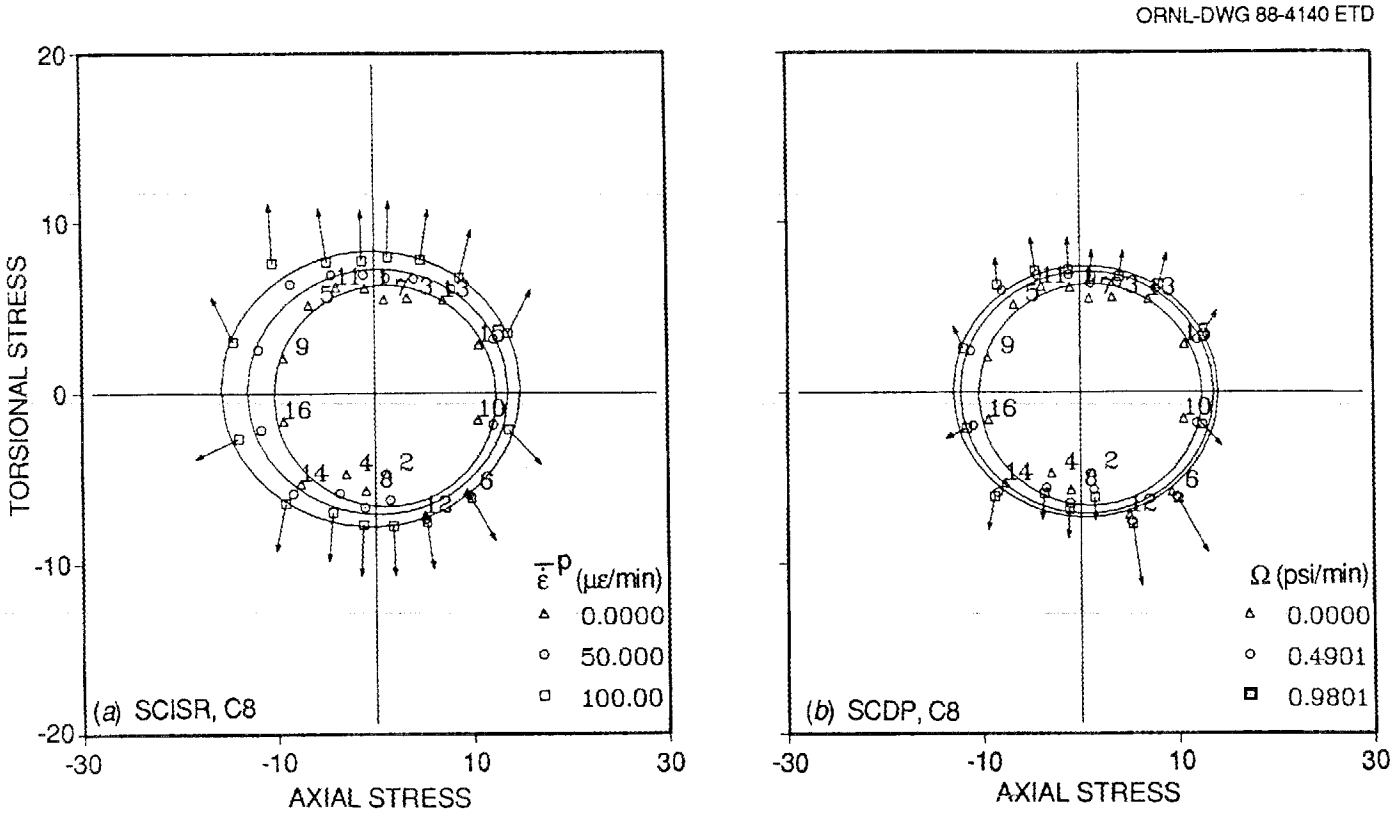

A.13. Flow surfaces for point 8 of Fig. 3 preloading.

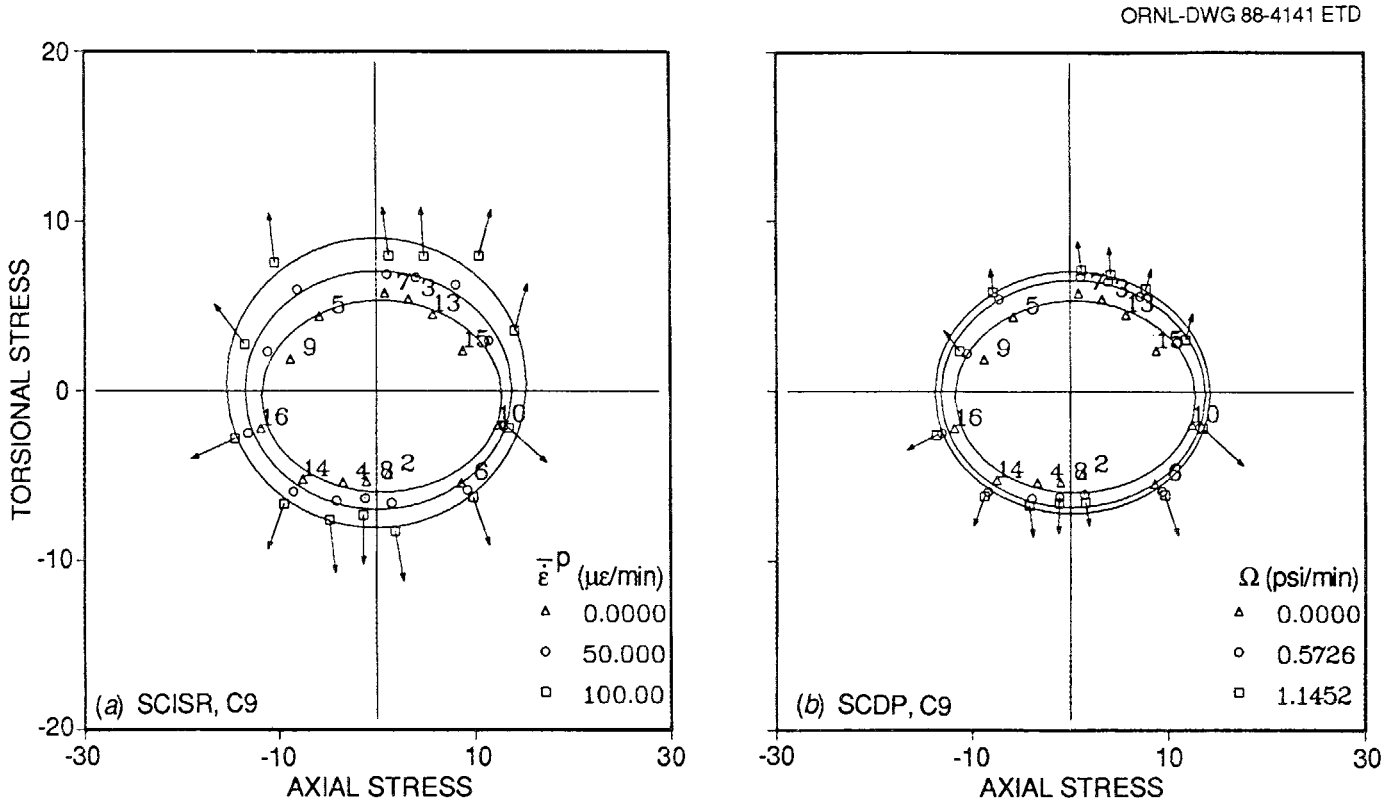

A.14. Flow surfaces for point 9 of Fig. 3 preloading.

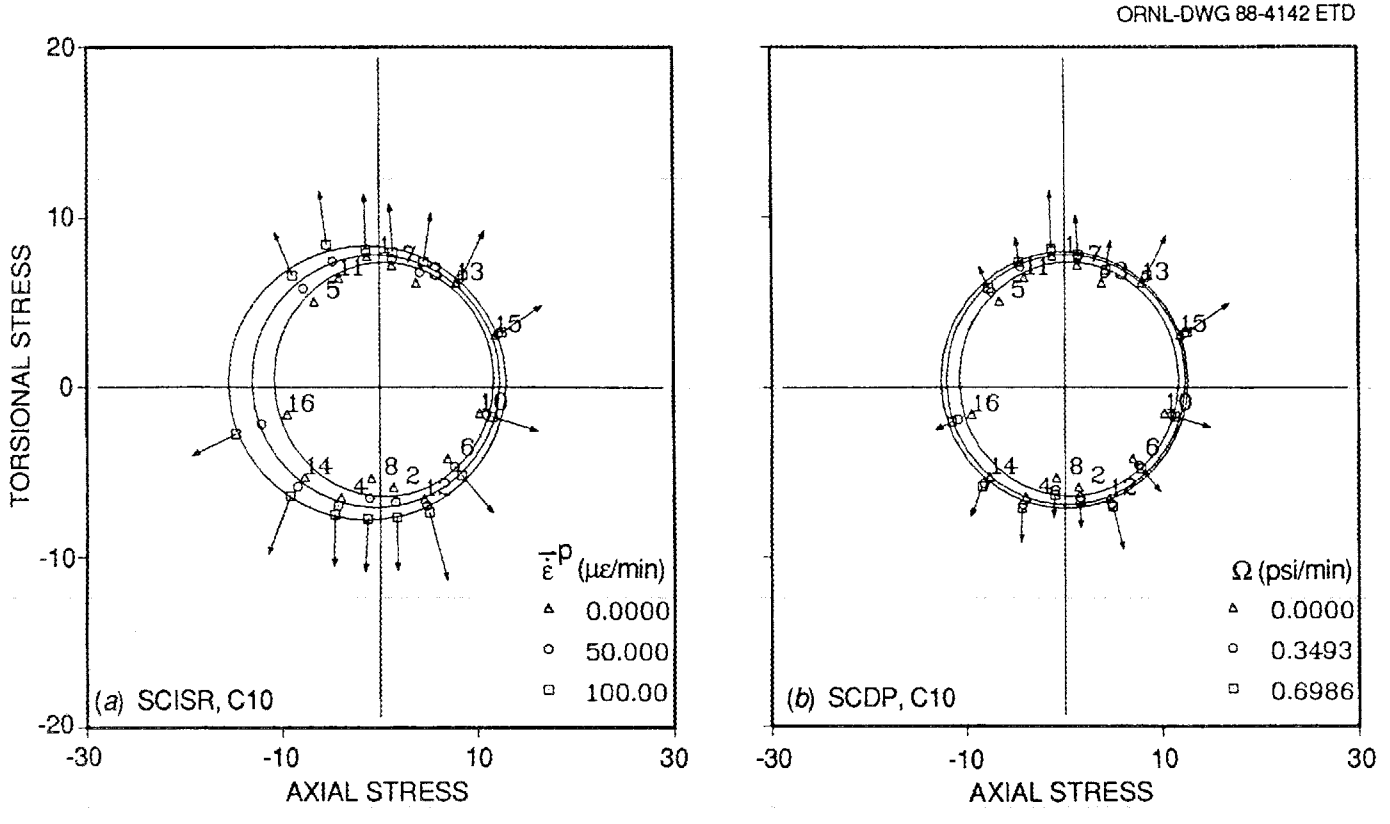

A.15. Flow surfaces for point 10 of Fig. 3 preloading.

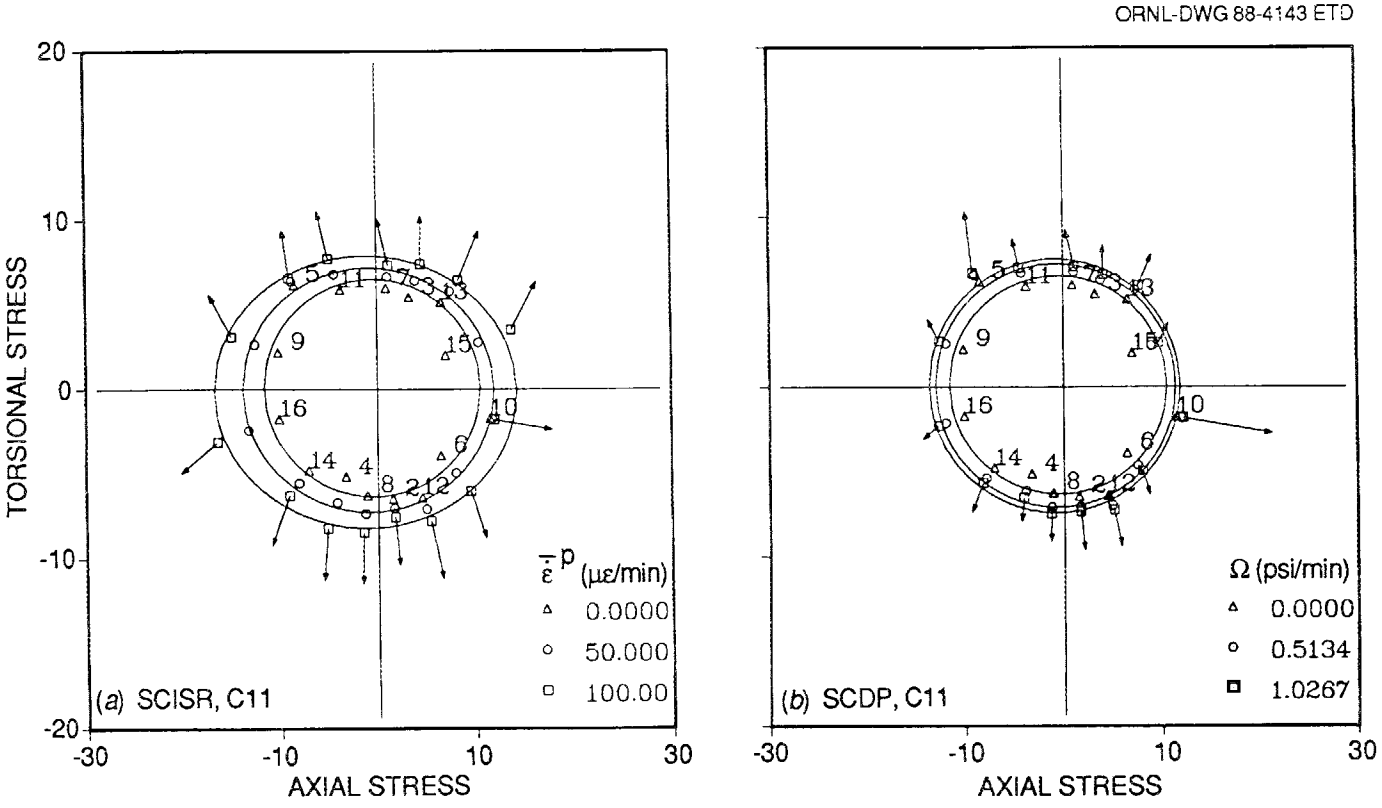

A.16. Flow surfaces for point 11 of Fig. 3 preloading.

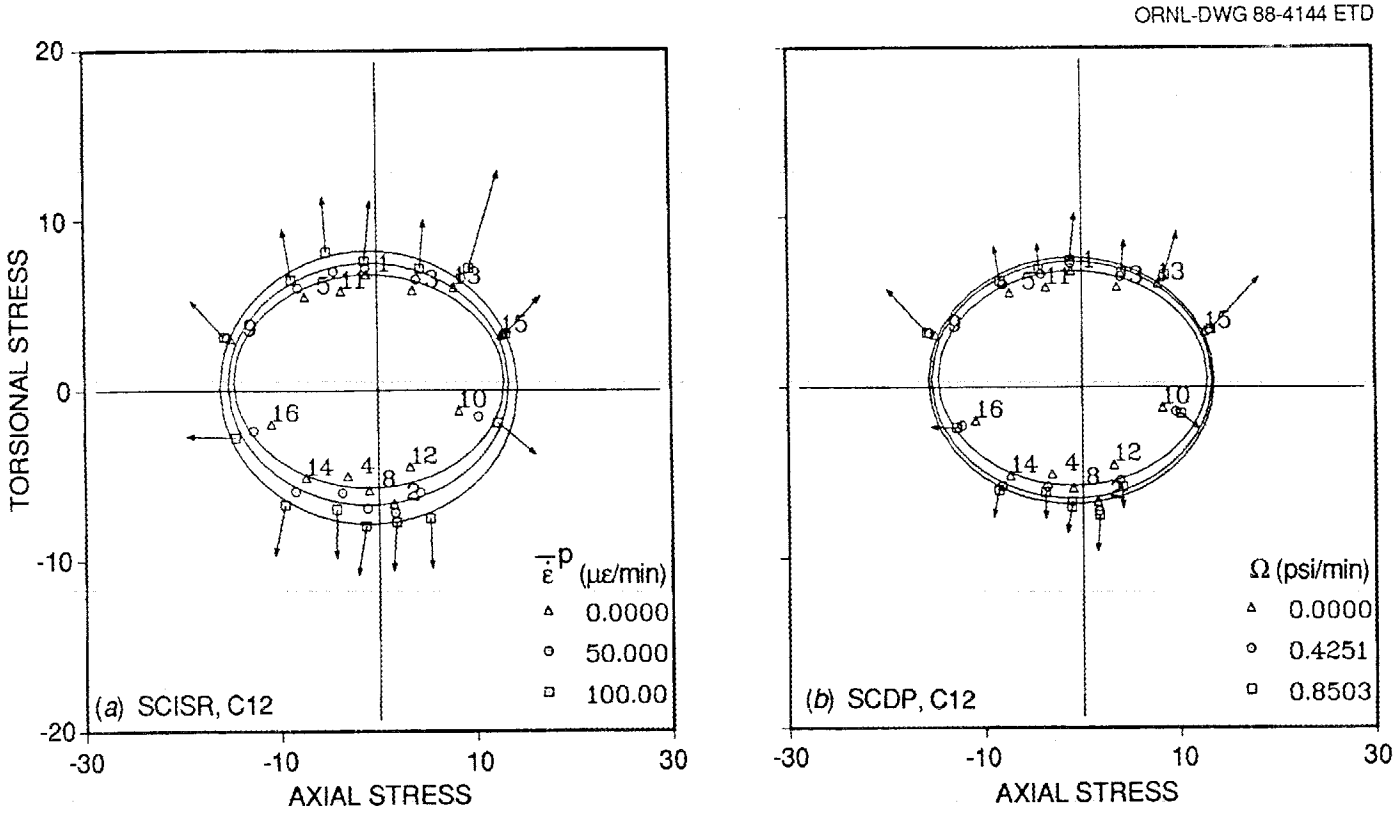

A.17. Flow surfaces for point 12 of Fig. 3 preloading.

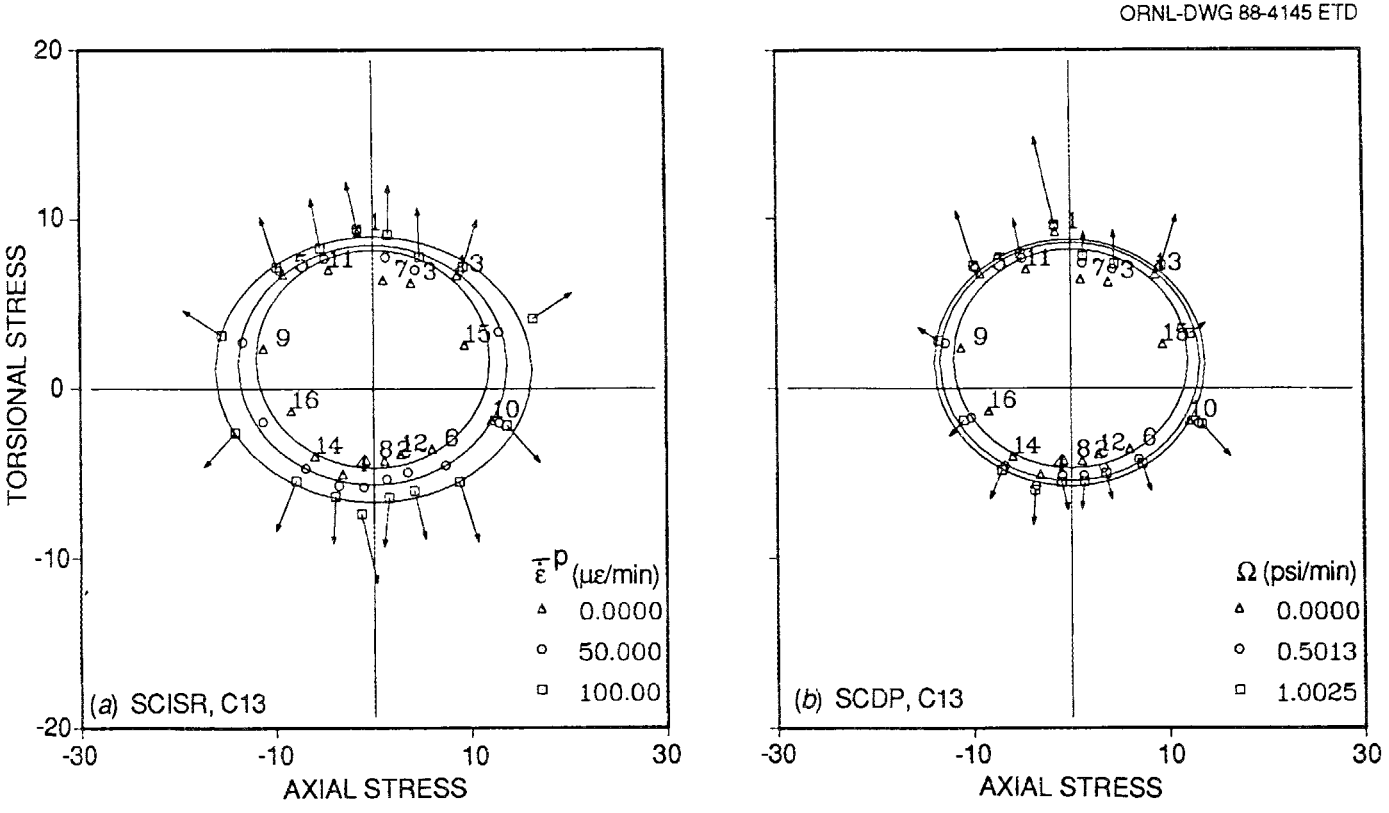

A.18. Flow surfaces for point 13 of Fig. 3 preloading.

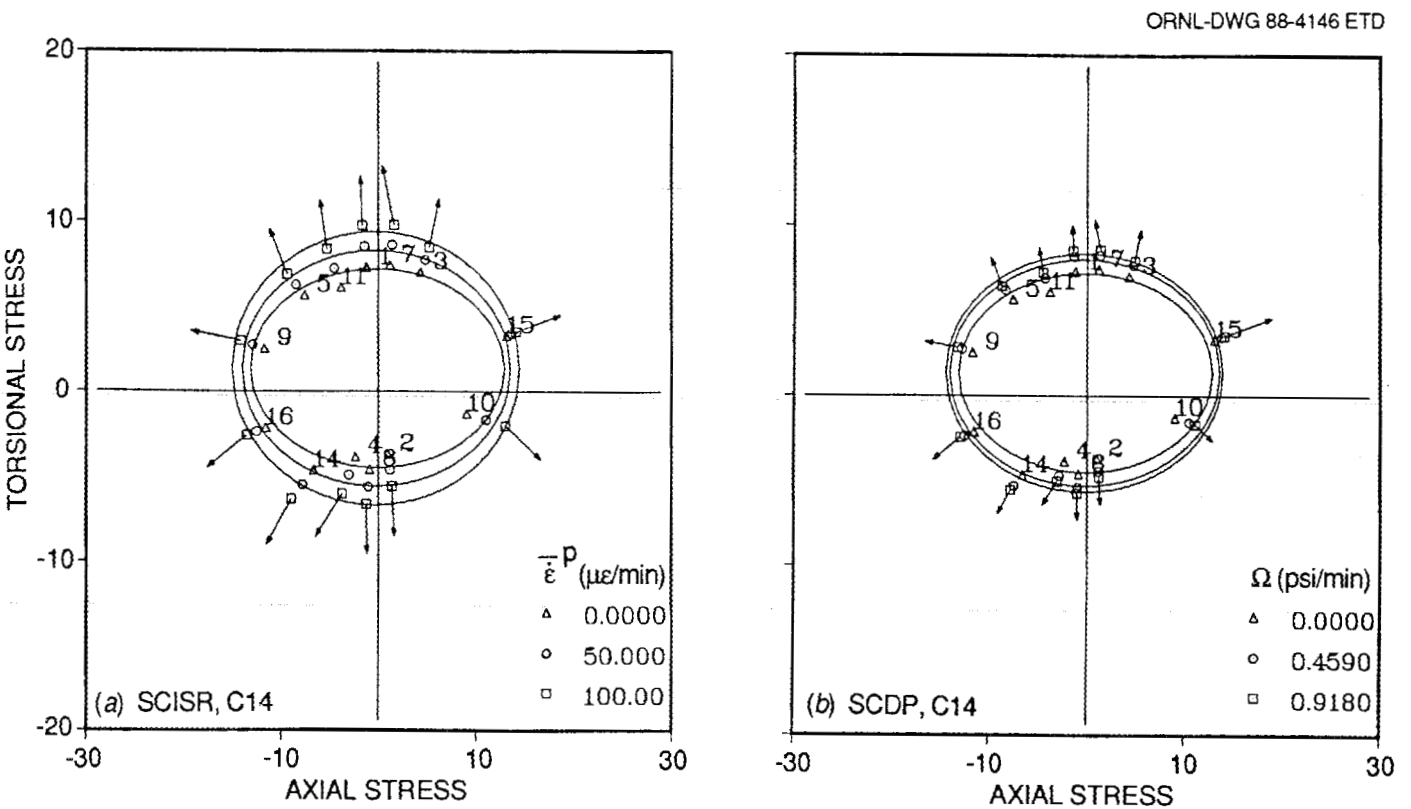

A.19. Flow surfaces for point 14 of Fig. 3 preloading.

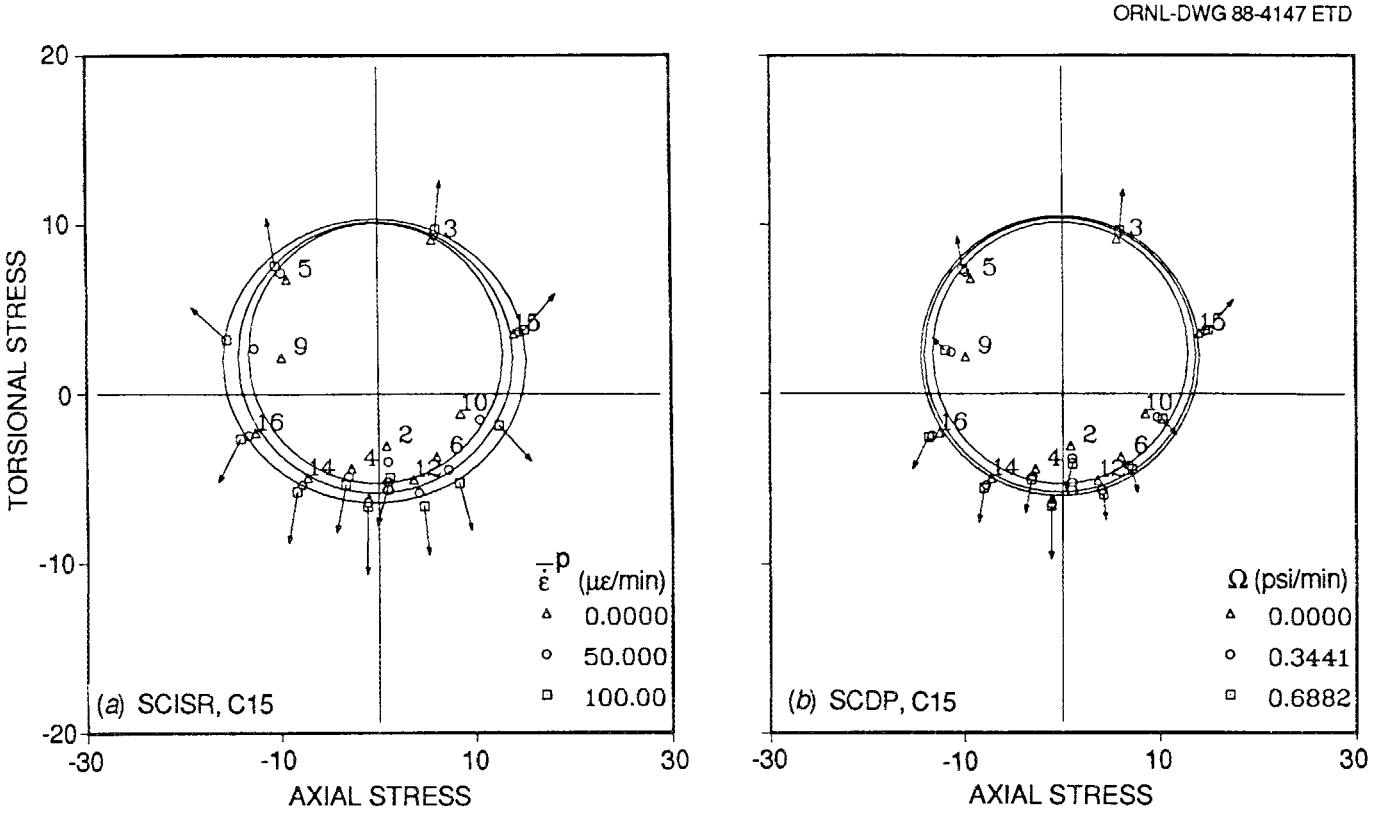

A.20. Flow surfaces for point 15 of Fig. 3 preloading.

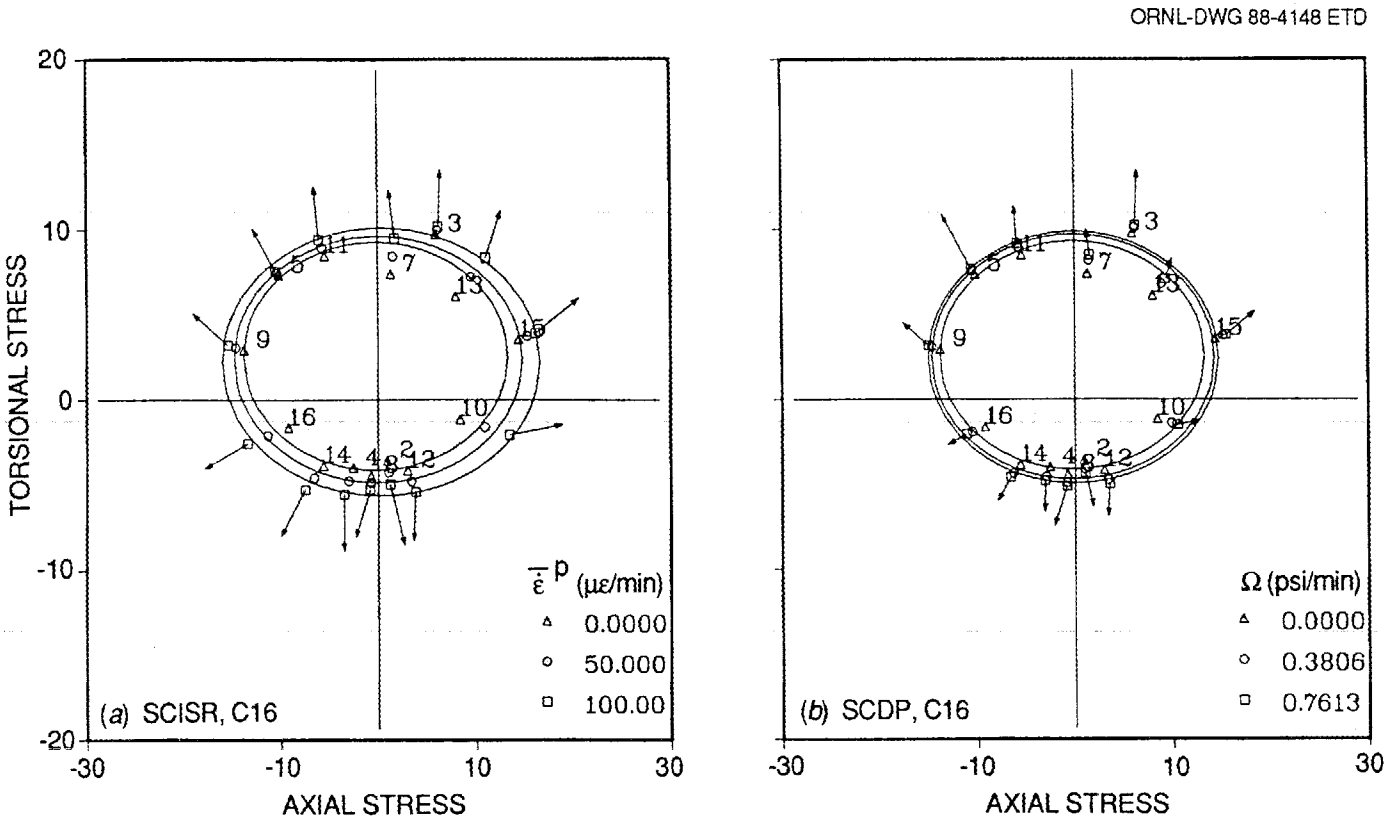

A.21. Flow surfaces for point 16 of Fig. 3 preloading.

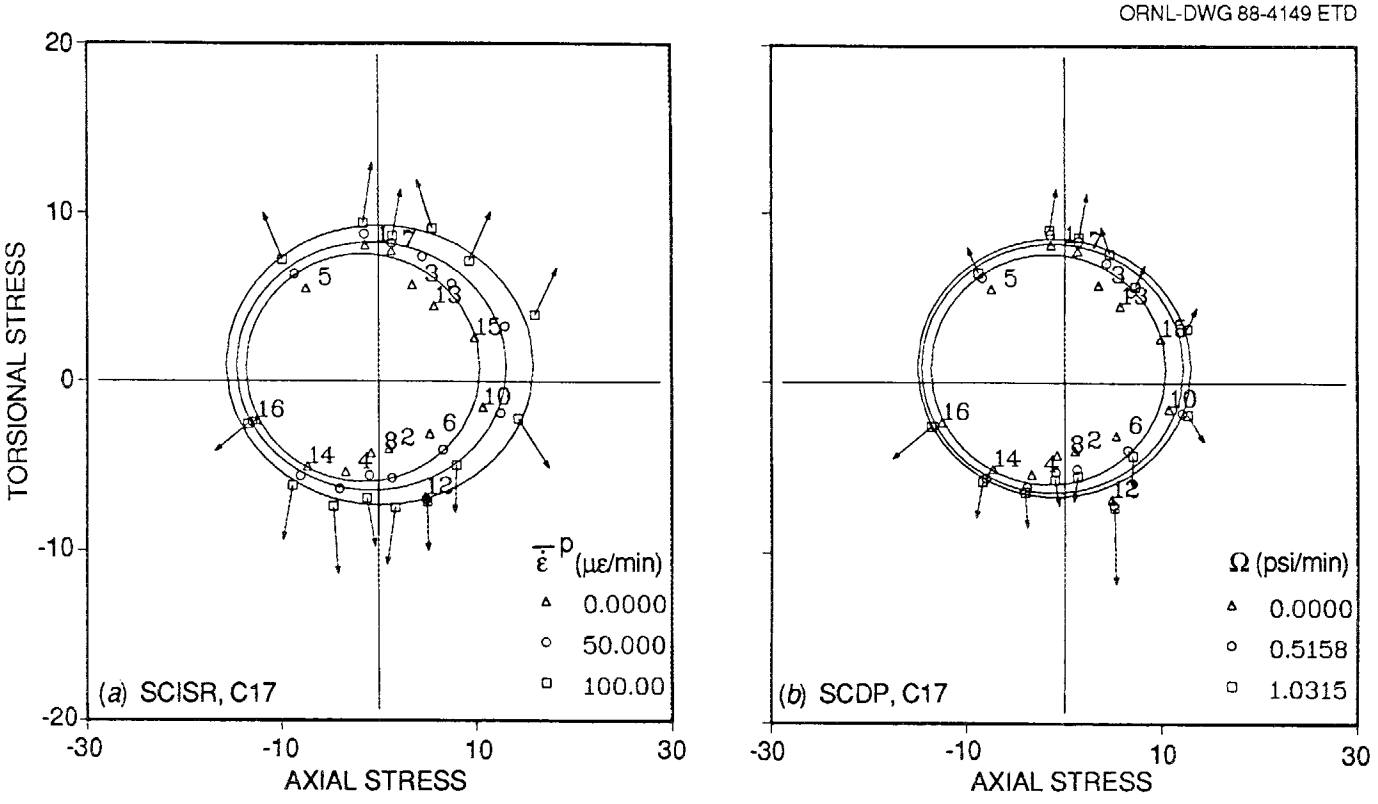

A.22. Flow surfaces for point 17 of Fig. 3 preloading.

ORNL/TM-10787

Internal Distribution

1. S. J. Ball
2. R. L. Battiste
3. J. J. Blass
4. C. R. Brinkman
5. S.-J. Chang
6–15. J. A. Clinard
16. J. M. Corum
17. R. L. Huddleston
18. K. C. Liu
19. C. E. Pugh
20. M. B. Ruggles
21. W. K. Sartory
22. R. W. Swindeman
23. G. T. Yahr
24. ORNL Patent Office
25. Central Research Library
26. Document Reference Section
27–28. Laboratory Records Deparment
29. Laboratory Records (RC)

External Distribution

30. C. Lacombe, University of Tennessee, Knoxville, TN 37916
31. J. R. Ellis, NASA–Lewis Research Center, 21000 Brookpark Road, Cleveland, OH 44135
32. D. N. Robinson, NASA–Lewis Research Center, 21000 Brookpark Road, Cleveland, OH 44135
33. R. L. Thompson, NASA–Lewis Research Center, 21000 Brookpark Road, Cleveland, OH 44135
34. C. C. Bigelow, Division of Advanced Technology Development, MC NE-462, Office of Technical Support Programs, U.S. Department of Energy, Washington, DC 20545
35. A. Van Echo, Division of Advanced Technology Development, MC NE-462, Office of Technical Support Programs, U.S. Department of Energy, Washington, DC 20545
36. L. G. Santos-Leon, Department of Energy, ORO, Oak Ridge, TN 37831
37. Office of Assistant Manager for Energy Research and Development, Department of Energy, ORO, Oak Ridge, TN 37831
38–39. Technical Information Center, DOE, Oak Ridge, TN 37831